Norwegian University of Life Sciences
Faculty of Environmental Science and Technology
Department of Environmental Sciences

Master's Thesis 2015
60 credits

Characterization of workplace aerosols in the manganese alloy production industry by X-ray diffraction, inductively coupled plasma optical emission spectrometry, and anion chromatography

Anders M. Brakestad

Samandrag

Arbeidarar i manganlegeringsindustrien vert eksponert for ulike Mn-sambindingar, noko som kan føra til ein neurologisk tilstand kalla manganisme. For å betre vurdera helseskadar frå Mn-eksponering, er det viktig å veta kva specier av Mn arbeidarane vert eksponert for. I dette arbeidet har tre ulike aerosolar frå ferromangan- (FeMn) og silikomangan- (SiMn) produksjon vorte karakterisert: a) omnsrøyk danna frå innsida av FeMn- og SiMn-omnane; b) aerosolar i arbeidluft tatt frå tappeområda av FeMn og SiMn; og c) aerosolar i arbeidsluft innsamla ved bruk av personlege respirable syklonar borne av FeMn- og SiMn-tapparar.

Før prøvekarakterisering vart XRD-bakgrunnsnivå studert for polyvinylklorid- (PVC), polykarbonat- (PC) og polytetrafluoroetyl- (PTFE) membranfilter. Vidare vart XRD-bakgrunnsnivå studert for fire ulike filterhaldarplater: aluminiums- (Al) plate, membranfilter av cellulose, enkeltkrystall av Si produsert av PANalytical, samt enkeltkrystall av Si produsert av MTI corporation. Bakgrunnsnivå for PVC var tydeleg lågare enn for PC og PTFE, og dei to enkeltkrystallane av Si var, som forventa, av overlegen kvalitet med omsyn på XRD-bakgrunnsnivå.

Omnsrøyk vart karakterisert med røntgendiffraksjon (XRD), assistert ved induktivt kopla plasma optisk emisjonsspektrometri (ICP-OES) for grunnstoffbestemmingar, ionekromatografi (IC) for bestemming av vassløyselege anion, samt pH-målingar for å vurdera surheit og basisitet. Aerosolfilter vart studert med XRD og ICP-OES, medan personlege eksponeringsfilter vart kun analysert med XRD. Det er vist at at krystallinske fasar hovudsakleg er mangan(II)dimangan(III)tetraoksid (Mn_3O_4), dikaliumsulfat (K_2SO_4), sink(II)oksid (ZnO) og β-kvarts; det er imidlertid ikkje visst kva kjelda til detektert β-kvarts er. Små mengder av andre fasar vart detektert, til dømes magnesium(II)karbonat ($MgCO_3$), magnesium(II)oksid (MgO), dijern(III)magnesium(II)tetraoxide ($MgFe_2O_4$) og sink(II)oksid (ZnO). Grunnstoffbestemmingar viste at hovudkomponentane i prøvene var kalium (K), mangan (Mn) og silisium (Si). Anionkromatografi viste at vassløyselege anion var tilstades som sulfat (SO_4^{2-}), klorid (Cl^-) og fluorid (F^-), noko som stemmer godt overeins med XRD-resultata. Vassekstrakta av både FeMn- og SiMn-omnsrøyk var lett basiske. Funna i arbeidet viser at arbeidarane vert eksponerte for ei mengd ulike sambindingar, noko som stemmer også godt overeins med tidlegare studier.

Faseidentifikasjon av prøvemateriale på aerosolfilter og personlege eksponeringsfilter var begrensa av låg signa-til-støyratio, på grunn av ei for lita mengd prøvemateriale på filtera. Stabling av filter førte til ei tydeleg auke i diffraktert signal, men også ei tydeleg auke i støy. Bruk av monokromator i XRD-instrumentet kan forbetra spektral reinheit og redusera bakgrunnsignal. Framtidige studie lyt fokusera på å auka mengda av prøvemateriale for XRD-karakterisering av aerosolprøvar. Ein framgongsmetode for å oppnå dette kan vera å modifisera NIOSH metode 7500 til manganhaldige aerosolprøver. Den moglege eksponeringa til α-kvarts bør også undersøkjast nærare.

Abstract

Workers in the manganese (Mn) alloy industry are exposed to a variety of Mn compounds, which may lead to a neurological condition called manganism. To better assess health effects due to Mn exposore, it is important to know to which Mn species workers are exposed. In this thesis, three different aerosols types from ferromanganese (FeMn) and silicomanganese (SiMn) production were characterized: a) furnace fumes generated inside the FeMn and SiMn furnaces; b) workplace aerosols collected in the FeMn and SiMn tapping areas; and c) workplace aerosols collected using personal respirable cyclones worn by FeMn and SiMn tappers.

Prior to sample characterization, XRD background levels of polyvinylethylene (PVC), polycarbonate (PC), and polytetrafluoroethylene (PTFE) membrane filters were checked. Further, XRD background signals of various sample plates were checked: aluminium (Al) plate, cellullose membrane filter, single-crystal Si plate manufactured by PANalytical, and a single-crystal Si plate manufactured by MTI corporation. PVC background levels were significantly lower than for PC and PTFE filters, and the two single-crystal Si plates were, as expected, of superior quality with respect to XRD background levels.

Furnace fumes were characterized by X-ray diffraction (XRD), aided by inductively coupled plasma optical emission spectrometry (ICP-OES) for elemental analyses, ion chromatography (IC) for determination of water-soluble anions, and pH measurements to assess acidity and alkalinity. Workplace aerosols were studied by XRD and ICP-OES, and personal exposure filters were studied by XRD only. Here it is shown that the crystalline phases are predominantly manganese(II) dimanganese (III) tetraoxide (Mn_3O_4), dipotassium sulfate (K_2SO_4), zinc(II) oxide (ZnO), and β-quartz; however, the source of detected β-quartz is not known. Minor amounts of several other phases were detected, e.g. magnesium(II) carbonate ($MgCO_3$), magnesium(II) oxide (MgO), diiron(III) magnesium(II) tetraoxide ($MgFe_2O_4$), and zinc(II) oxide (ZnO). Elemental analysis revealed the major components of the samples to be potassium (K), Mn, and silicon (Si). Anion chromatography revealed that water-soluble anions were present as sulfate (SO_4^{2-}), chloride (Cl^-), and fluoride (F^-), which agree well with XRD results. The FeMn and SiMn furnace-fume water-extracts were slightly alkaline. The findings of this thesis show that workers are exposed to a variety of different compunds, which agree well with previous studies.

Phase identification of aerosol filters and personal exposure filters was limited by low signal-to-noise ratio, due to the low amount of sample mass on the filters. Stacking of filters resulted in a large increase of diffracted signals, but also a large increase in noise. The use of a monochromator in the XRD instrument may improve spectral purity and reduce background signals. Future investigations should focus on increasing sample material for XRD characterization of aerosol samples. One way to achieve this may be by adapting NIOSH Method 7500 to manganese-holding aerosol samples. The possible exposure to α-quartz should also be investigated further.

Preface and acknowledgements

This master's thesis is part of my master's program in analytical chemistry, and has been written for the Department of Environmental Sciences, Norwegian University of Life Sciences, Campus Ås, Norway. The work has been carried out in co-operation with, and financed by, the National Institute of Occupational Health (NIOH), Oslo, Norway.

Many people deserve recognition for the help given to me during the last year. First and foremost I would like to thank my main supervisor, Yngvar Thomassen, for insightful discussions, good ideas, and constructive feedback on my work. Next I wish to thank my co-supervisor, Elin Gjengedal, for all the helpful comments and feedback on my writing. I also wish to thank Kari Dahl, Grete Friisk, Nils Petter Skaugset, and Balazs Berlinger for helping me with my analyses — and for never (seemingly) getting bored with all of my questions. Lastly I want to thank Julian Tolchard and Martijn Fransen for being willing to help me over e-mail with various aspects of XRD analysis.

Ås, May 2015
Anders M. Brakestad

Contents

List of Figures

List of Tables

List of Abbreviations

Abbreviation	Meaning
DL	"Detection limit"
EDX	"Energy dispersive X-ray spectrometry"
EGC	"Eluent generator cartridge"
EM	"Electromagnetic radiation"
FeMn	"Ferromanganese"
FFP	"Furnace fume powder", refers to furnace fumes collected in the emission purification unit
IC	"Ion chromatography"
ICP-OES	"Inductively coupled plasma optical emission spectrometry"
ICS	"Ion chromatography system"
IS	"Internal standard"
NIOH	"National Institute of Occupational Health", Oslo, Norway
NIOSH	"The National Institute for Occupational Safety and Health", USA
PC	"Polycarbonate"
PEF	"Personal exposure filter", refers to tapping fumes collected using personal respirable cyclones
PHD	"Pulse-height discrimination"
PMT	"Photomultiplier tube"
PTFE	"Polytetrafluoroethylene"
PTN	"Peak-to-noise", refers to the peak-to-noise ratio in XRD analysis
PVC	"Polyvinylchloride"
QC	"Quality control", refers to quality control samples used in IC analysis
QL	"Quantification limit"
RTMS	"Real-time multiple-strip", refers to an XRD detector type
SEM	"Scanning electron microscope"
SiMn	"Silicomanganese"
TEM	"Transmission electron microscope"
TF	"Tapping fume", refers to tapping fumes collected with multiport sampler
THF	"Tetrahydrofuran"
WDX	"Wavelength dispersive X-ray spectrometry"
XRD	"X-ray diffraction"
XRF	"X-ray fluorescence"

1

Introduction

Manganese (Mn) is a transition metal, located in the fourth period and seventh group. Mn has a rich chemistry, and can take on every oxidation state from -3 to +7. This ensures that Mn can form many different kinds of compounds, with varying chemical properties. Most common in nature are Mn oxides, silicates, and carbonates, e.g. MnO_2, Mn_3O_4, $MnSiO_3$, and $MnCO_3$. Constituting about 0.1 % of the Earth's crust, Mn is the 12th most abundant element in the crust.

Manganese is necessary for several enzymatic activities in the human body, thus making Mn an essential element to humans. We do not need much Mn, and indeed, Mn deficiency is rarily observed; at least *some* Mn is present in very common foodstuffs. Examples of food with high Mn concentration are hazelnuts, whole-wheat bread, tofu, bass, spinach, and black tea (Health Alicious Ness n.d.).

Since Mn is abundant in nature, it can be used inexpensively in the steel- and aluminium (Al) alloy production. Manganese makes steel harder, more ductile, and more resistant to wear. Austenitic Mn-steel contains about 12 % Mn (Key To Metals 2002), although other alloys exist with lower Mn concentrations; Mn content is varied to get different properties.

Manganese is also a common alloying element in Al. Mn increases Al strength, and the concentration normally ranges from 5 ppm to 50 ppm (Key to Metals n.d.). The steel and aluminium alloy industry are the largest industrial uses of manganese, but the element is used in other industries as well, examples of which are in dry-cell batteries, in welding rods, in chemicals, and as a fuel additive (Gunst et al. 2000).

Norway is one of the world's largest producing countries of FeMn and SiMn, constituting about 10 % of the world's production (Ellingsen et al. 2000). They further write that 5000 – 10000 Norwegian workers are exposed to Mn daily.

Workers in the metal industry have for long been exposed to particulate matter in air containing Mn. Indeed, occupational exposure was first described in the 1800's, then called "brass founders' ague", and later in the 1900's shipyard industry. These short-term and high-dose exposures lead to specific symptoms, later known as "metal fume fever" (Kelleher et al. 2000), and although Mn is not the most common cause for this syndrome, it is known to cause the same symptoms and disease. The National Institute for Occupational Safety and Health (NIOSH) (1978) describes these symptoms in the following way:

> Inhalation of fumes with high concentrations of Mn and its oxides may bring about "metal fume fever". Symptoms of metal fume fever are chills and fever, upset stomach, vomiting, dryness of the throat, cough, weakness, and aching of the head and body. Symptoms occur several hours after exposure to fumes and usually lasts only for a day.

The general human exposure to Mn mainly occurs through intake of food, except in cases where atmospheric concentrations may be higher, such as in industrial workplaces (Loranger et al. 1995). However, other point sources are available through inhalation, such as Mn-containing fireworks and combustion of fossil fuels (Michalke et al. 2007). Several industrial workplaces with elevated atmospheric Mn concentrations are common today, e.g. exposure during mining in Mn ores, working in the steel, Al, or Mn alloy production, or the welding of such alloys (Gjønnes et al. 2011; Michalke et al. 2007). In such workplaces long-term exposures are common, and this eventually leads to a disease similar to (but different from) Parkinson's disease, called "manganism" (Lucchini et al. 2009). These symptoms differ from those resulting from short-term exposure, and are described by NIOSH (1978) in the following way:

> Prolonged or repeated exposure to manganese may effect the nervous system with difficulty in walking or balancing, weakness or cramps in the legs, hoarseness of the voice, trouble with memory and judgement, unstable emotions or unusual irritability. If high exposure continues, a person may have poor coordination, difficulty in speaking clearly, or shaking or tremor of the arms or legs. A person may also have hallucinations or uncontrollable laughter or crying.

During the last couple of decades, more attention has been given to long-term occupational exposure to Mn. The Mn accumulated over time affect the central nervous system, and manifests as psychoneurological dysfunctions. To protect the workers in the best possible way, we must have a good understanding about what compounds the workers are exposed to, how to measure the exposure, how the compounds are transported in the human body, what the effects are, and how to measure the effects. One way to assess what the workers are exposed to is by collecting air-samples from the environment they work in. Workplace aerosols are normally deposited on a filter, mounted in special filter cassettes. Such samples reveal what compounds are present in the air the workers inhale.

The rich chemistry of Mn makes the risk assessment difficult, because the different chemical forms of Mn have different bioavailabilities. We must therefore know which chemical forms of Mn workers actually inhale during work. Special instrumentation is required to determine the chemical forms of Mn in samples. Elemental analysis cannot give this kind of information, as such analyses only estimate the concentration of the elemental constituents of the molecules in a sample.

An easy and efficient way to identify the chemical compounds present in the sample is X-ray diffraction (XRD) analysis. However, this technique relies on the sample being crystalline. The sample is irradiated by X-rays, which, upon hitting the electrons in the sample, are diffracted off in another direction. These diffracted X-rays are then detected. This technique can deduce the crystal structure and the lattice parameters of the various crystalline "phases" in the sample, and, when this data is compared to a

database containing approximately 177 000 phases, the molecular composition in the sample may be found.

XRD analysis of air-assessment filters is a relatively quick process. Sample preparation is minimal as the filter is simply placed on a sample holder and put in the instrument, although sample collection itself may be a lengthy process. Data acquisition is quick due to the high data collection rates of modern detectors. Specialized and well-designed software also reduces time spent interpreting the data.

Other techniques give valuable information that aids the XRD analyses. Elemental analysis helps excluding certain phase candidates during phase identification, since only the elements of the highest concentration are likely to be detected with XRD. Instead of searching for crystal structures that include all elements in the periodic table, the search-and-match analysis can be reduced to the most abundant elements in the samples. If the XRD analysis indicates that salts are present, ion chromatography of the water extract may further substantiate that claim if the correct anion or cation is detected. Measurements of pH may also provide useful information. If the detected phases (oxides, for example) from XRD analysis should give an acidic water extract, but the pH measurements are basic, then this finding indicates contradicting results. In this way pH measurements may be another way of comfirming, or invalidating, the results.

One challenge when collecting workplace aerosols is the low amount of aerosol mass deposited on the filter. Long sampling periods are often needed, several days, to collect enough aerosol mass to obtain useable signal-to-noise ratios for XRD phase characterization.

The main goal of this thesis has been to perform phase characterization of various fumes related to tapping of FeMn and SiMn, in order to better understand what chemical forms of Mn the workers are exposed to. In addition, XRD background levels of various filter and sample-plate materials have been tested, in order to minimize noise in XRD analyses.

The results presented in this thesis will be used in animal experiments carried out at NIOSH, Morgantown, USA (Berlinger 2015). Similar to what was done in a study by (Antonini et al. 2009), rats will be exposed to tapping fumes from FeMn and SiMn production. The main focus the study carried out by NIOSH will be to investigate how much Mn that deposits in various organs, particularly in the regions of the brain.

2

Literature review: Characterization of workroom aerosols in Mn alloy smelters

Health effects due to exposure to Mn have been widely studied (Ellingsen et al. 2000, 2008, 2013; Myers et al. 2003; Oberdörster 2001; Roels et al. 1992, 1987). However, few studies have characterized workplace aerosols with X-ray or electron diffraction. These techniques are excellent for studying the crystalline chemical species in the aerosol. The articles in this brief review are limited to those presenting chemical and phase characterization data of aerosol samples, or similar samples, related to Mn alloy production.

Gunst et al. (2000) studied individual aerosol particles collected during production of FeMn and SiMn alloys, at Eramet's production plant in Porsgrunn. They did so by carrying out wavelength-dispersive X-ray (WDX) analysis on individual particles, using an electron microprobe. A bulk chemical characterization of FeMn tapping fumes was also carried out using ICP-OES, after microwave-digesting the filters in *aqua regia* and hydrofluoric acid (HF). Bulk chemical composition showed the following content in wt% (limited to those with content above 1 wt%): 2.86 wt% calcium (Ca), 2.0 wt% iron (Fe), 51.0 wt% potassium (K), 3.7 wt% magnesium (Mg), 17.9 wt% Mn, 3.0 wt% sodium (Na), 1.6 wt% lead (Pb), 8.9 wt% silicon (Si), and 6.4 wt% zinc (Zn).

The individual particle characterization showed a diverse community of particle compositions. Gunst et al. divided all particles into six different groups, based on their chemical composition. Of 329 particles from tapping of FeMn, 91.2 % were placed in two of these six groups: 69.3 % in Group III and 21.9 % in Group V (same group number as used as in article). Group III was dominated by C, O, Si, and Mn, with the following typical particle compositions: 12.0 at% carbon (C), 57.2 at% O, 23.1 at% Si, and 3.8 at% Mn. Group V was dominated by the following typical particle compositions: 40.7 at% C, 33.1 at% O, 4.5 at%Na, 14.0 at% Mn, 1.7 at% Fe, and 2.0 at% copper (Cu). The authors state that these values are "typical" concentration, but do not state if they are mean or median concentration based on the particles in the respective group, or if they are arbitrarily chosen to represent the group.

Whereas 50 wt% of the FeMn fume is K, less than 1 wt% of SiMn casting fume is K. Potassium is a volatile element, and because casting takes place after tapping, most of the volatile K may have evaporated by the time casting takes place. However, SiMn fumes should not be expected to be similar to the FeMn fumes. Further, the casting fume is not necessarily comparable to the tapping fume, since they are generated at two different production stages.

Because Gunst et al. have characterized individual particles, and not bulk samples,

the issue of representability arises. It is hard to imagine that the 329 particles from the tapping area represent the vast number of particles in the workroom aerosol. Variations from the values reported should be expected, as the aerosol is likely not to be homogeneous. In addition, day-to-day variation in operation conditions, which will affect the aerosol, further reducing the representability of the 329 particles characterized. Nonetheless, the chemical compositions reported are true for 329 particles, and possibly many more, and should serve as an indication of the chemical composition of the workplace aerosol.

A recent study by Kero et al. (2015) performed elemental analysis of fumes collected in a SiMn alloy production plant, using energy-dispersive X-ray spectrometry (EDX) coupled to an electron microscope. They found that the major elements were Si, Mn, and O, but no numerical concentrations were reported. Minor elements were Mg, Ca, Al, and K, while trace elements were Na, Fe, Zn, Cu, and chlorine (Cl).

Kero et al. do not specify the meaning of the terms "major" and "minor" elements, although they state that their results are in fair agreement with previous studies (Gjønnes et al. 2011; Gunst et al. 2000). It is also hard to judge whether the terms were treated equally for both fumes, or if the fumes were evaluated independently. Due to limited knowledge about the data, comparability to other studies is also limited.

In a study by Gjønnes et al. (2011), individual aerosol particles collected during tapping of high carbon FeMn (HC FeMn) were analyzed with electron diffractometry coupled to a transmission electron microscope (TEM). In addition, EDX coupled to a scanning electron microscope (SEM-EDX) was used to determine elemental composition in individual particles.

SEM-EDX revealed K concentrations up to 50 at%, and variable amounts of Na, sulfur (S), Zn, Cl, and O. They also found up to 20 at% Mn in the larger particles (around 2 µm geometric diameter). Further, they observed agglomerates (larger than 5 µm geometric diameter) consisting of mixed Fe and Mn oxides, silicates and carbonates, and metallic particles (for example SiMn and FeMn).

SEM analysis of two different fibre morphologies were seen (along with other particle shapes): 1) fibres characterized by "contrast fringes either normal to the fibre axis or as two sets of fringes inclined to the fibre axis", and 2) which showed "no distinct contrast features". In the first type, EDS shows only Mn and O, with a Mn/O ratio indicating either MnO or Mn_3O_4 when compared to Mn oxide standards. In the second type they found Mg in addition to Mn and O, with a Mg/Mn ratio between 0.05 and 0.1. Sometimes they also found small amounts of Fe in the second fibre type.

TEM reavealed three main particle morphologies: chain-like agglomerates, sheets and flakes, and fibres and needles. Electron diffractometry of chain-like agglomerates (diameters below 0.2 µm) revealed mainly crystals of MnO, although they also observed individual particles and agglomerates containing Mn_3O_4 and Fe_3O_4. EM of sheets and flakes (0.1 – 0.2 µm) revealed mainly MnO, Mn_3O_4 and Fe oxides. Minor amounts of Mn_2O_3 and MnO_2 were also observed in the sheets and flakes. Analysis of fibres and

needles revealed that the first type was Mn_3O_4, and that the second type was either MnO or Mn_3O_4. The second type was also enriched in Mg and Fe.

The same issue as with the study by Gunst et al. arises here: Individual particles have been characterized, and not a bulk sample. In some ways, individual characterization provides more information about the sample. It is possible to selectively characterize particles of a certain morphology, size, or shape. However, unless a very large number of particles are characterized, even compositions of the the sub-group of particles may not be representative for their own sub-group. Therefore variations from the reported compositions should be expected. Still, as noted for the Gunst study, the characterizations are representative for the particles that were characterized.

Thomassen et al. (2001) studied the chemical speciation of Mn in workplace aerosol during production of FeMn and SiMn alloys. They developed a sequential leaching procedure, and were able to sequentially dissolve different oxidation states of Mn. The water-soluble Mn ions were dissolved in 0.01 mol L^{-1} ammonium acetate at pH 7. Mn^0 and Mn^{2+} (MnO, FeMn alloys, Mn^{2+} part of the mixed-state Mn_3O_4) were dissolved in 25 % acetic acid. The Mn^{3+} and Mn^{4+} components (Mn^{3+} part of Mn_3O_4, Mn_2O_2 and MnO_2) were dissolved in 0.5 % hydroxylamine hydrochloride in 25 % acetic acid. The remainding chemical forms of Mn were considered insoluble, and were dissolved in a mixture of *aqua regia* and HF, under pressure in teflon autoclaves. The insoluble forms were mostly Mn-silicates and SiMn, and were not considered bioavailable.

The leaching procedure was used for both bulk inhalable and respirable aerosol sub-fractions, collected at different stages of production in both a SiMn plant and a mixed FeMn/SiMn plant. During FeMn/SiMn smelting operations, 10 % of the inhalable sub-fraction were water-soluble Mn compounds, 54 % were Mn^0 and Mn^{2+} holding compounds, 21 % were Mn^{3+} and Mn^{4+}, and 16 % were insoluble compounds of Mn. The same proportions for the respirable sub-fraction were the following: 8 % water-soluble Mn compounds, 62 % Mn^0 and Mn^{2+} holding compounds, 12 % Mn^{3+} and Mn^{4+} compounds, and 18 % were insoluble compounds of Mn.

During SiMn smelting operations, the following concentrations were discovered for the inhalable sub-fraction: 4 % water-soluble Mn compounds, 39 % Mn^0 and Mn^{2+} holding compounds, 11 % Mn^{3+} and Mn^{4+} compounds, and 46 % were insoluble compounds of Mn. For the respirable sub-fraction the concentrations were: 14 % water-soluble Mn compounds, 47 % Mn^0 and Mn^{2+} holding compounds, 10 % Mn^{3+} and Mn^{4+} compounds, and 29 % were insoluble compounds of Mn.

Manganese is less soluble during production of SiMn, which is attributed to formation of SiMn alloys evaporating from the melt. Oxidation states 0 and II seem to be the most abundant form of Mn in both the inhalable and respirable sub-fraction, except for the inhalable sub-fraction during smelting operations in the SiMn plant, at which the insoluble Mn components dominated.

The composition in tapping fume from the mixed plant may be different from that of a pure FeMn plant, and, as is seen from their data, different from a pure SiMn plant.

Hence the speciation data may not be representable for pure FeMn or SiMn plants. As is seen in Thomassen et al.'s data, Mn speciation in FeMn/SiMn fume and SiMn fume is different.

Despite not performing elemental analysis, the study by Thomassen et al. interestingly presents the Mn speciation in the tapping fume, which no other study has done. This is interesting because speciation affects solubility, which affects bioavailability, and hence toxicity. Knowing the Mn speciation may therefore facilitate the setting of occupational exposure limits by showing the Mn distribution between harmful and harmless Mn species.

A study by Shen et al. (2005) analyzed furnace dust samples from Mn alloy production collected at the Tasmanian Electro Metallurgical Company Pty Ltd (TEMCO). The furnace dust is accumulated at large settling ponds, and were collected at three different sites of the settling pond. Further, at each sampling point, powder was taken from three different depths in the pond: 0 cm to 30 cm, 30 cm to 60 cm, and 60 cm to 90 cm. The powder was then analyzed by X-ray fluorescence (XRF) spectrometry for element concentrations. They reported that one of the sites (Northwest C) showed irregular data, and excluded this particular site from their subsequent analyses. Therefore, data from the two remaining sites are presented here. The reported concentrations varied within a few wt% between different sampling depths at same sampling point. Typical concentrations are the following (wt%, in dried samples): 30 % to 33 % Mn, 0.9 % to 1.5 % Zn, and 19 % to 22 % C. The dust was wet and contained about 58 wt% water, determined from LECO analysis.

Further, they studied the dried powder by XRD to assess the present crystalline phases. It should be noted that prior to the XRD analysis, the powder had been subject to extraction for organic components by using solvents such as hexane, toluene, tetrahydrofuran, pyridine, dichloromethane, chloroform, and ethyl acetate. The influence of the solvents on the inorganic phases is, however, not known. They reported that the major phases from the two sites are $MnCO_3$ (rhodochrosite), MnO (manganosite), Mn_3O_4 (hausmannite), SiO_2 (quartz), $Mn,Ca(CO_3)$ (manganocalcite). They were not able to detect any Zn-containing phases by XRD analysis due to the low concentration of Zn. However, from X-ray photoelectron spectroscopy (XPS) they concluded that Zn was present as $ZnSO_4$ and ZnO, with a molar ratio of 1:2 between the two. It is not mentioned whether they detected αor β-quartz.

Shen et al. explained that TEMCO produces both FeMn and SiMn alloys with electric ferroalloy furnaces. However, they did not state whether the furnace-dust deposition-site contains a mixture of FeMn and SiMn furnace dust; that is, the ventilation of the four furnaces join together. If the deposition area is a mix of the two fumes, then is the mixture homogeneous? Hence, it is hard to judge whether it is FeMn dust or SiMn that they have analyzed, which makes it difficult to compare their results to other studies. In Table 2.1 the detected phases and elements have been placed under the FeMn header, but this is not really justified; it is just to fit their data into the table..

Table 2.1. Summary of detected elements (≥ 1 wt%) and detected phases in FeMn and SiMn tapping fumes reported in four of the cited studies

Study	FeMn		SiMn	
	Elements	Phases	Elements	Phases
Gunst et al. (2000)	Ca, Fe, K Mg, Mn, Na, Pb, Si, Zn	—	—	—
Kero et al. (2015)	—	—	Si, Mn, O Mg, Ca, Al, K	—
Gjønnes et al. (2011)	K, Mn, Na, S, Zn, Cl, O	MnO, Mn_3O_4, Fe_3O_4, MnO_2, Mn_2O_3	—	—
Shen et al. (2005)[a]	Mn, C, Zn	Mn_3O_4, MnO, $MnCO_3$, SiO_2, $(Mn,Ca)CO_3$	—	—

[a] Their data should not be placed under the "FeMn" heading, since it is unknown whether dust at the settling pond is a homogeneous mix of FeMn and SiMn dust, or if FeMn and SiMn dominate local areas of the settling pond. Their placement in the table is therefore arbitrary.

The cited studies share some features. The elemental analyses agree on that the most abundant elements in the Mn alloy tapping fume (except O and C) are Mn, Fe, Si, K, Ca, and Mg. The fumes/aerosol/furnace dust are complex mixtures of different elements and different oxidation states of Mn. This finding was true for all sampling sites and during all steps of the production, for all studies; none of the production steps of sampling points can be characterized by only one compound. However, the studies presenting diffraction data, and those attempting to predict the Mn oxides based on Mn:O ratios, propose that Mn_3O_4 and MnO are the most likely Mn species (oxidation state II/III and II respectively).

The complex nature of this kind of occupational exposure makes risk assessment difficult. Workers are exposed to a complex mix of elements and compounds of varying bioavailabilities. It is not fully known how the solubility or oxidation state of Mn compunds affect the reactivity at deposition sites in the human body (Thomassen et al. 2001), and more research on these relationships needs to be conducted to facilitate risk assessments and the setting of meaningful occupational exposure limits. In addition, compounds such as α-quartz, which is associated with its own health effects, may be present in high concentrations.

3

Theory and principles

This chapter will *briefly* present the analytical techniques IC and ICP-OES. In addition, an in-depth account of X-ray diffractometry will be presented.

3.1 X-ray diffraction

The theory of X-ray diffraction is well-known (see for example Pecharsky et al. (2009)). The following theory is just a brief summary of what one might encounter in the literature, unless otherwise stated.

3.1.1 Analytical principle

The principle of x-ray diffractometry relies on the fundamental interaction between electromagnetic (EM) radiation and matter, and on wave-wave interaction. A wave hitting an obstacle will diffract; that is, bend around the obstacle. The bending effect varies depending on the wave's wavelength, and the size of the obstacle. Visble light will not be diffracted by atoms in a crystal, to any observable extent, because the wavelength is so much longer than the distance between the atoms.

When two waves are superimposed, they will interfere with each other. The amplitudes will add double if their maxima are perfectly aligned (constructive interference) and cancel each other if their minima are perfectly aligned (destructive interference). This is visualized in Figure 3.1. Constructive interference is central to the principle of X-ray diffraction.

EM-radiation can interact with matter in three ways: ionization, compton scattering, and thomson scattering. Ionization: If the electron hit by X-rays are ejected out of the

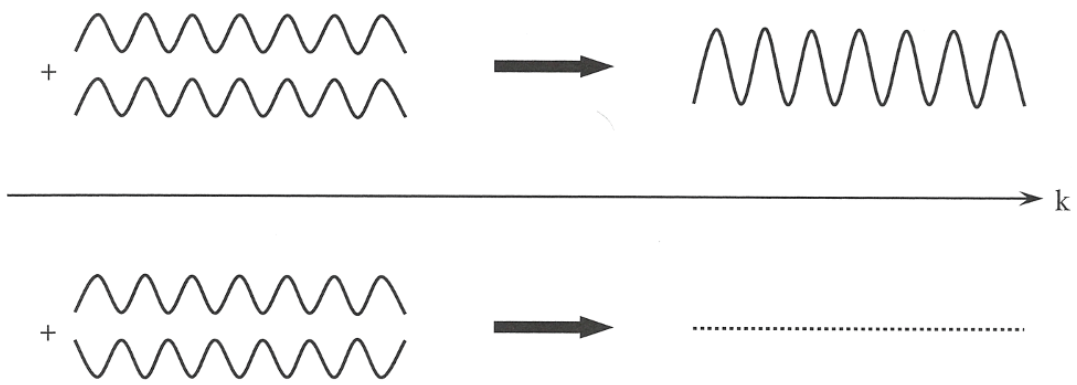

Figure 3.1. Contructive interference occurs when the peaks of the superimposed waves overlap, while destructive interference occurs when the minima overlap. Figure taken from *Fundamentals of Powder Diffraction and Structural Characterization of Materials*, 2nd ed., by V. K. Pecharsky and P. Y. Zavalij, 2009, New York, USA: Springer. Copyright 2009 by Springer Science+Business Media. Adapted with kind permission from Springer Science+Business Media.

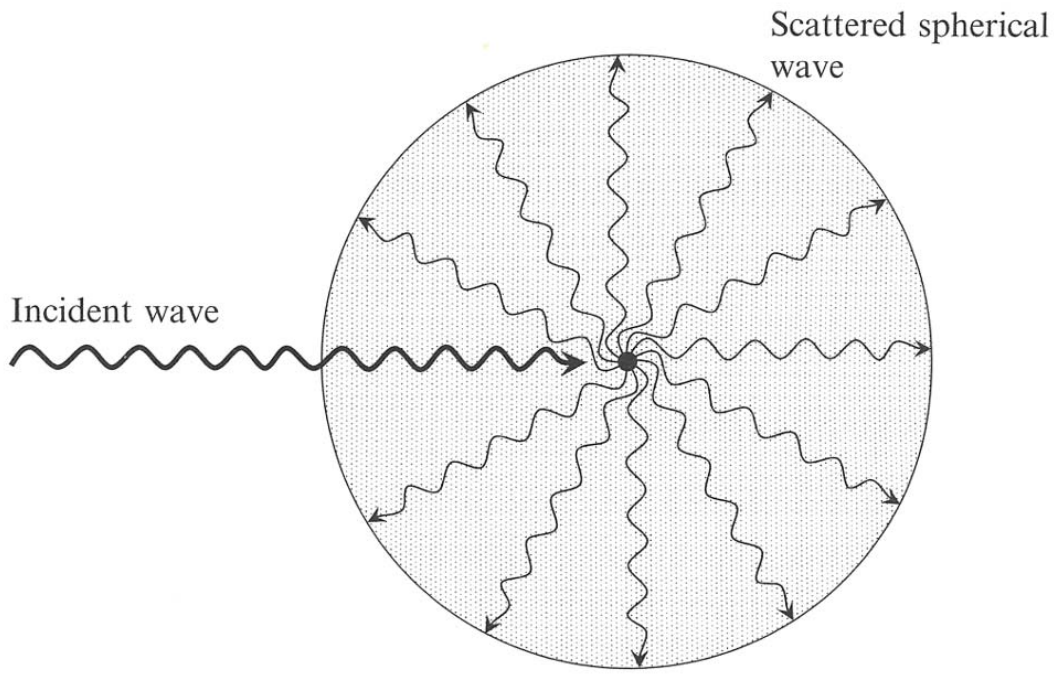

Figure 3.2. Showing X-rays hitting an electron, which then re-emits the wave without any energy loss. In three dimensions, the emitted wave will be spherical. Figure taken from *Fundamentals of Powder Diffraction and Structural Characterization of Materials* (p. xx), 2nd ed., by V. K. Pecharsky and P. Y. Zavalij, 2009, New York, USA: Springer. Copyright 2009 by Springer Science+Business Media. Adapted with kind permission from Springer Science+Business Media.

atom, the atom has become ionized. In this process, the wave's energy is fully transferred to the electron. This is a type of inelastic interaction, because energy transfer is involved. Compton scattering: The photon may transfer some of its energy to the electron, and being scattered at an angle. This is also an inelastic interaction. The events following the interaction may involve a fully ejected electron, or just an excitation. Thomson scattering: the wave may interact elastically, and induce oscillations in the electron at the frequency of the incoming radiation. The electron then emits EM radiation in all direction, conserving the energy. It is this elastic scattering that is interesting in X-ray diffraction.

In three dimensions, the elastically scattered wave is spherical, with its origin in the scatter point (see Figure 3.2). If five such scatter points (electrons) are placed next to each other, and are irradiated, the emitted and spherical waves will interfere at certain points, both constructivelly and destructivelly. See Figure 3.3

Building on the basic theoretical foundation that P.P. Ewald developed in the beginning of the 1900's, Max von Laue and coworkers discovered that a crystal lattice works as a three dimensional diffraction grating when irradiated by X-rays. In an experimental set-up they bombarded a single crystal of copper sulphate with X-rays and placed a photographic plate behind the crystal. They observed a strong central darkening, due to the primary beam, and several other dots surrounding the center (the so-called "Laue

dots"). Thus, the diffraction of X-rays by crystals was discovered, and Laue recieved the Nobel Price in 1914 for this discovery.

Within a year of Laue's discovery, William Lawrence Bragg realized that the diffracted X-rays could be modeled as X-rays reflecting off parallel planes within the atom (Ewald 1962, Chapter 5), and derived a geometrical criterion for when constructive interference would occur. The unit cell parameters in a crystal (distances between atoms in the unit cell) are (very much) characteristic for the crystal lattices, and so the diffraction of X-rays by crystals could be used to deduce the crystal structure of crystalline materials. The Braggs derived a geometrical relationship defining the angles at which scattered waves would interfere constructively and produce an intense "reflection" of the x-rays. This relationship, termed "Bragg's law", is central to the x-ray diffractometer.

To derive Bragg's law, we model the crystal lattice as a structure consisting of various "atomic planes". At these planes, the electron density is higher than in-between the planes, and the probability of scattering of the incoming X-rays is higher. The distance between two adjacent planes is denoted d, the X-ray's wavelength is denoted λ, and the incident irradiation angle is denoted θ. All this is visualized in Figure 3.4.

We see from the figure that the two rays have different path lengths; the one penetrating deeper into the crystal travels farther. This path difference means that the rays will experience a phase shift; they are in-phase as they enter the crystal, but not necessarily as they exit. The figure shows that the lower ray travel a total of $2l$ farther than the upper ray. With simple trigonometry, we find that

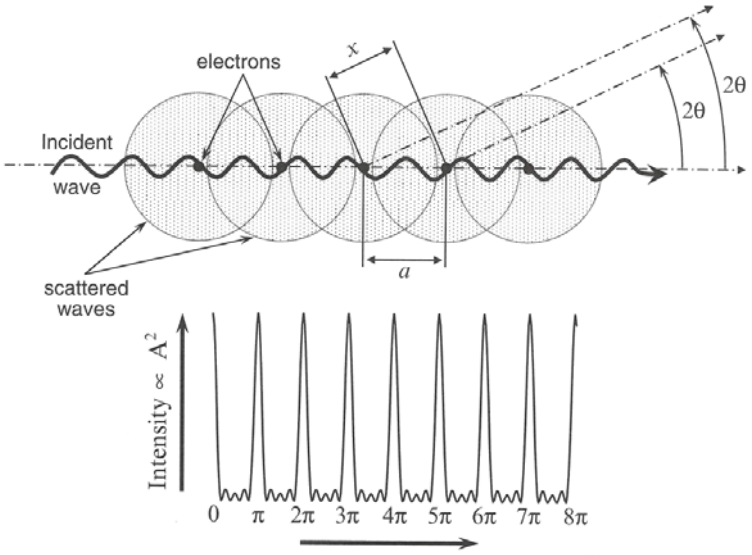

Figure 3.3. Illustration of how constructive and destructive interference occurs from different scattering points. Figure taken from *Fundamentals of Powder Diffraction and Structural Characterization of Materials*, 2nd ed., by V. K. Pecharsky and P. Y. Zavalij, 2009, New York, USA: Springer. Copyright 2009 by Springer Science+Business Media. Adapted with kind permission from Springer Science+Business Media.

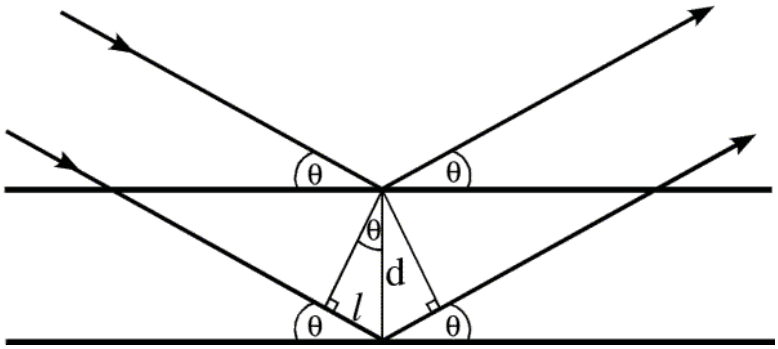

Figure 3.4. Simple sketch of two adjacent atomic planes of high electron density. Two parellel and in-phase X-rays enter the crystal and are scattered in the same angle at different depths inside the crystal. When Bragg's law is fulfilled, the rays will exit the crystal in-phase and interfere constructively.

$$2l = 2d \sin\theta \tag{3.1}$$

Bragg's law is found by seeing that full constructive interference occurs when the path difference equals integer multiples of the wavelength, or in mathematical terms,

$$n\lambda = 2d \sin\theta, \tag{3.2}$$

where $n \in \mathbb{Z}^+$ (also called the order of reflection). In essence, we control the wavelength, vary the angle, measure the reflected intensity, and deduce the unit cell parameters. The intensity is plotted against the diffraction angle 2θ, and the resulting graph is called the "diffractogram".

In the case of *powder* diffraction, the result is slightly different. A powder basically consists of a vast number of tiny single-crystals, ordered in random orientations. The diffracted wave-pattern is not a symmetrical array of dots, as from a single crystal, but rather a cone with its apex in the origin, and with a cone angle of 4θ. As the incoming waves' angle is varied, concentric diffraction cones with different cone angles are formed. This is nicely illustrated in Figure 3.5. When placing a detector or a photographic plate behind the powder, these cones will form dark, concentric circles or ellipses on the detection medium with varying intensities, depending on how much constructive interference occured at the specific angle, illustrated in Figure 3.6. These rings, called "Debye rings" (from the Dutch physicist and chemist Peter Debye), are central to the powder diffractogram, and its detection will be described later.

3.1.2 Basic anatomy

Although X-ray powder diffractometry may be carried out in both transmission geometry and reflection geometry, only the reflection geometry will be covered in this chapter. The reflection geometry is commonly referred to as the "Bragg-Brentano" geometry, named after the physicists Bragg and J. C. M. Brentano.

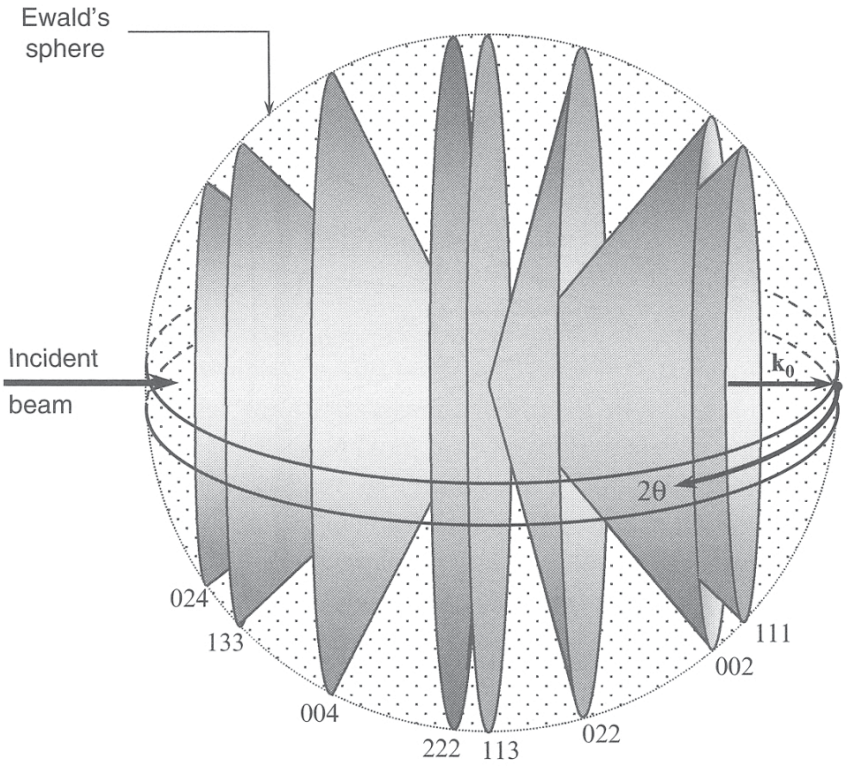

Figure 3.5. Illustration of diffraction cones from powder diffraction. Figure taken from *Fundamentals of Powder Diffraction and Structural Characterization of Materials*, 2nd ed., by V. K. Pecharsky and P. Y. Zavalij, 2009, New York, USA: Springer. Copyright 2009 by Springer Science+Business Media. Adapted with kind permission from Springer Science+Business Media.

3.1.2.1 The X-ray source

X-rays are generated with two main types of devices: X-ray tubes and synchrotrons. Synchrotrons consist of circular tubes (hundreds of meters in diameter) in which charged particles (electrons, protons, etc.) travel. Their stable trajecetory is ensured by magnetic lenses placed on the tube walls. When charged particles accelerate (bend) they emit radiation, which can be varied by varying the particle speed. Synchrotrons are large and expensive to build and maintain, but offer superior quality X-rays compared to X-ray tubes. X-ray tubes, however, are inexpensive and small, fitting in benchtop instruments. Therefore, this section focuses on the typical X-ray tube only.

Wilhelm Röntgen discovered X-rays in 1895 when operating a Crookes tube (electrical discharge tube), though he did not know that it was X-rays he had discovered. Electrical discharge tubes may emit X-rays when the applied voltage is high enough, resulting in high-energy electrons that lead to fluorescence when colliding with components inside the tube. New kinds of tubes were designed specifically to generate these mysterious X-rays, and X-rays were incorporated in conventional medicine even before the nature of X-rays were understood.

These X-ray tubes have not changed much over the 100 or so years since they were

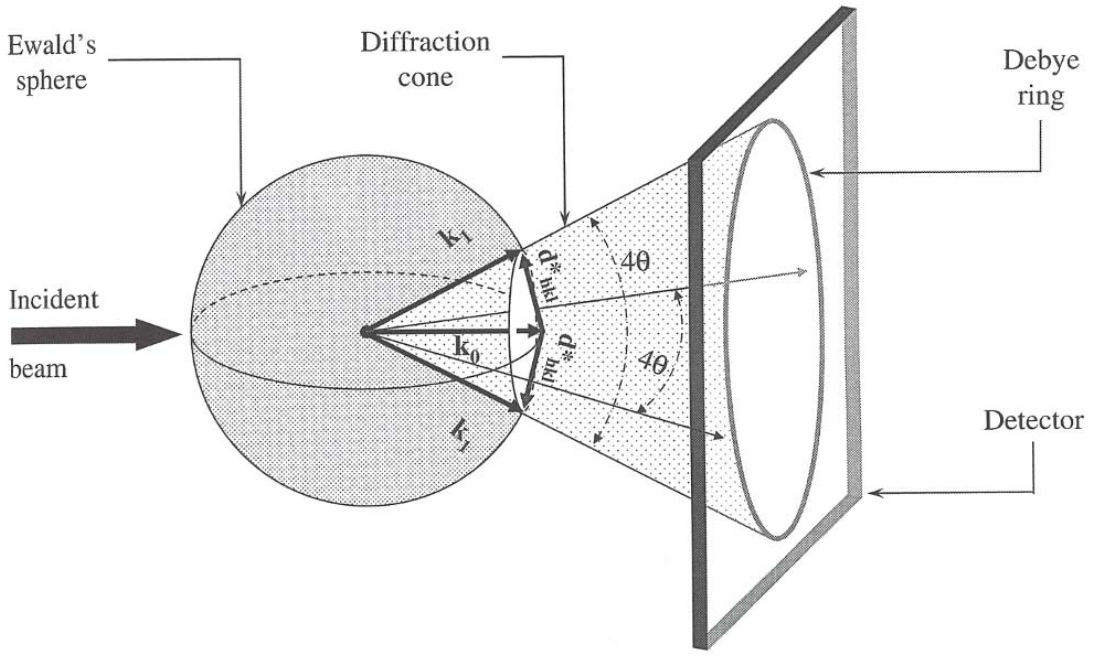

Figure 3.6. Illustration of how diffraction cones are projected onto a flat detector surface. The projected image of *several* diffraction cones is a set of concentric rings, or segments of concentric rings if the plate is not large enough. Figure taken from *Fundamentals of Powder Diffraction and Structural Characterization of Materials*, 2nd ed., by V. K. Pecharsky and P. Y. Zavalij, 2009, New York, USA: Springer. Copyright 2009 by Springer Science+Business Media. Adapted with kind permission from Springer Science+Business Media.

first made, though, of course, they have been modernized. The modern X-ray tube includes a heated cathode, usually wolfram (W), and a water-cooled anode metal. An electric potential is applied, and loose electrons in the W kathode are accelerated down towards the anode. Most of the energy invovled is lost as heat (hence the water cooling), but some energy is used to generate continuous and characteristic X-rays.

Continuous X-rays are generated by the mechanism called "bremsstrahlung" (German; breaking radiation), which takes place when the high-energy electrons are decelerated as their trajectory is bent when they interact with the atomic nucleus in the anode metal. They may excite electrons one or more times before leaving the anode material, losing energy as they do so. In the context of X-ray diffraction, bremsstrahlung is not of interest, and is considered noise to be minimized. In Figure 3.7, the continuous part is everything but the sharp peaks.

Characteristic X-rays are generated by another mechanism. The accelerated kathode electrons may collide with bound electrons in the anode material. Because the accelerated electrons' energy much exceeds that of the bound electrons, anode atoms may become ionized. When the inner electron (K shell) is ejected, the newly formed vacancy is filled by an electron from a outer shell (L or M). When the L or M electron "falls down", EM radiation is emitted in the X-ray region. The sharp peaks in Figure 3.7 are characteristic radiation resulting from three different electronic transitions. These X-rays are characteristic because every element's discrete energy levels are characteristic,

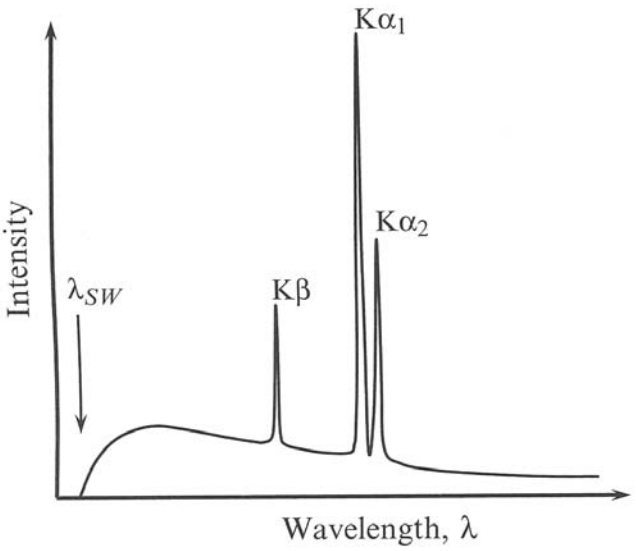

Figure 3.7. Continuous and characteristic radiation resulting from ejection of K-shell electrons, and filling of the vacancy by either L- or M- shell electrons. The continuous background is of no interest in XRD analysis, and is considered noise. K$\alpha_{1,2}$ is most often used in XRD, while Kβ is filtered out by either using filters of monochromators. Figure taken from *Fundamentals of Powder Diffraction and Structural Characterization of Materials*, 2nd ed., by V. K. Pecharsky and P. Y. Zavalij, 2009, New York, USA: Springer. Copyright 2009 by Springer Science+Business Media. Adapted with kind permission from Springer Science+Business Media.

and it is these X-rays that are interesting in X-ray diffraction analysis.

Although the characteristic X-rays are characteristic to each element, it is not monochromatic (although *much* more so than bremsstrahlung) This is because there is a fine-structure of energy levels within the main electron shells (K, L, and M), meaning that the emitted characteristic X-rays comprise a *mix of different* characteristic X-rays; electronic transitions within this fine-structure result in non-pure radiation.

Each electron in an atom can be assigned a unique "label" by using the four quantum numbers. Depending on the exact quantum state of the electron involved in filling the vacancy, the emitted characteristic X-rays will vary slightly. For instance, the Kα_1 line is the result of a transition from $2p_{3/2}$ to 1s. The Kα_2 and Kβ lines result from other transitions. These transitions, leading to a set of emitted characteristic wavelengths, have consequences for the X-ray diffraction analysis, as the Bragg angle is different for different wavelengths. Several ways of "purifying" the X-rays exist, and they will be outlined later.

The X-ray tube is tightly sealed to not let X-rays escape uncontrollably. However, several beryllium (Be) windows are placed next to the anode to let X-rays exit the tube at certain directions. Beryllium is used because of its low atomic number, and hence X-rays have a low probability of interating with the relatively tiny electron cloud. When X-rays exit the tube, they enter the focusing mechanism of the diffractometer.

3.1.2.2 The slits

Slits have an important part in the X-ray diffractometer. The X-rays emerging from the X-ray source diverge in their propagation, which is bad for resolution. The slits collimate the divergent rays; that is, making them approximately parallel. Various types of slits are comonly used in the diffractometer: soller slits, divergence slits, anti-scatter slits, and the receiving slit.

The soller slit are a set of thin, parallel plates of a certain length in the beam path, stacked next to each other with a certain space between each plate (Figure 3.8). The soller slits collimate the beam, resulting in parallel rays instead of divergent rays. Soller slits are used in both the incident beam and the diffracted beam, usually of the same size at both places. The collimation effect can be increased by decreasing the space between the plates, or by increasing the length of the plates. However, this comes at a cost of the diffracted intenstiy.

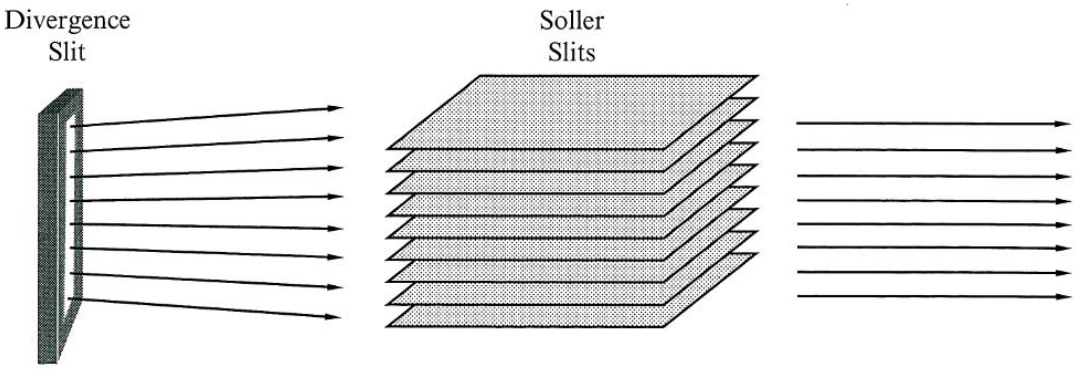

Figure 3.8. Illustration of how soller slits collimate the X-ray beam. Non-parallel waves are absorbed by the slits, and hence only waves parallel "enough" are let through. Figure taken from *Fundamentals of Powder Diffraction and Structural Characterization of Materials* (p. xx), 2nd ed., by V. K. Pecharsky and P. Y. Zavalij, 2009, New York, USA: Springer. Copyright 2009 by Springer Science+Business Media. Adapted with kind permission from Springer Science+Business Media.

The divergence slits are placed in the incident beam, and their job is to reduce the divergence of the X-ray beam. They affect both the intensity and resolution, depending on their placement and opening. The divergence slits may be a fixed opening, resulting in a constant volume of irradiation on the sample; however, the irradiated area is not constant, and decreases as the angle 2θ increases. This may lead to poor quality peaks at high bragg angles. To counter this, automatic-opening slits exist. These slits open up as the irradiation angle increases, resulting in a constant irradiated area on the sample. This improves the peak quality at high bragg angles, but the background has an upward slope as 2θ increases. Software makes it possible to mathematically convert the diffractogram from "automatic divergence slit" to "fixed divergence slit", which levels out the diffracogram. To achieve a better collimation effect, two divergence slits can be placed in sequence, where the second slit further collimates the beam coming from the first slit.

Anti-scatter slits are placed in the diffracted beam, and their job is to limit the diffracted rays to those solely scattered by the crystal, and exclude those scattered from air, the sample holder, or from something else. A large anti-scatter slit increases the intensity at the cost of resolution, while a small opening does the opposite. The anti-scatter slits may also be of the fixed or automatic type. The automatic anti-scatted slit are usually set to accept the same length as the sample was irradiated with. Hence, the irradiated length and the "observed length" are usually the same.

The receiving slit is placed at the X-ray focal point in the diffracted beam (Ermrich et al. 2011), and defines the intensity and resolution of the detected signal. A large receiving slit increases intensity and reduces resolution, and vica versa. The settings are adjusted according to the specific need of the analysis.

3.1.2.3 The monochromator and filter

The monochromator is used to purify the X-ray beam. This involves reducing the intensity of the Kα_2 and Kβ contributions without sacrificing the Kα_1 intensity too much. Usually a beta filter or a crystal monochromator is used.

The common monochromator is a single crystal, and works by the principle of Bragg's law. The crystal is irradiated at a certain angle chosen such that, according to Equation (3.2), only a certain wavelength will be diffracted. The angle is chosen to allow Kα_1 to be diffracted. The monochromatic X-rays then passes through collimators and slits and reach the sample. This method eliminates the Kα_2 and Kβ contriutions, while keeping the Kα_1 intensity intact.

A monochromator can also be placed in the diffracted beam. This has other benefits, as it will drastically decrease the background signals. For example, sample fluorescence will be almost completely removed, which is significant for cobolt (Co), Fe, and Mn containing samples. Diffracted wavelengths from the sample holder will also be eliminated.

The beta filter is a thin nickel sheet placed in the incident beam. The filter material depends on the the wavelength of the X-rays used, and hence the anode material in the X-ray tube. The filter material is chosen in such a way that the absorption edge of the filter material lies just before the K$\alpha_{1,2}$ peaks of the X-ray source spectrum. In this way, the filter absorbs the Kβ wavelength while letting K$\alpha_{1,2}$ pass through. For the common Cu-anode, nickel is used as a beta filter. As is seen in Figure 3.9, most of the beta line is absorbed, while most of the alpha lines are let through. The beta filter method is less expensive than using a crystal monochromator, but has the downside of including the Kα_2 component. In addition, although most of the beta line is removed, some intensity is still left in the X-ray beam after the filter. The specific applications for the diffractometer dictates which method should be used.

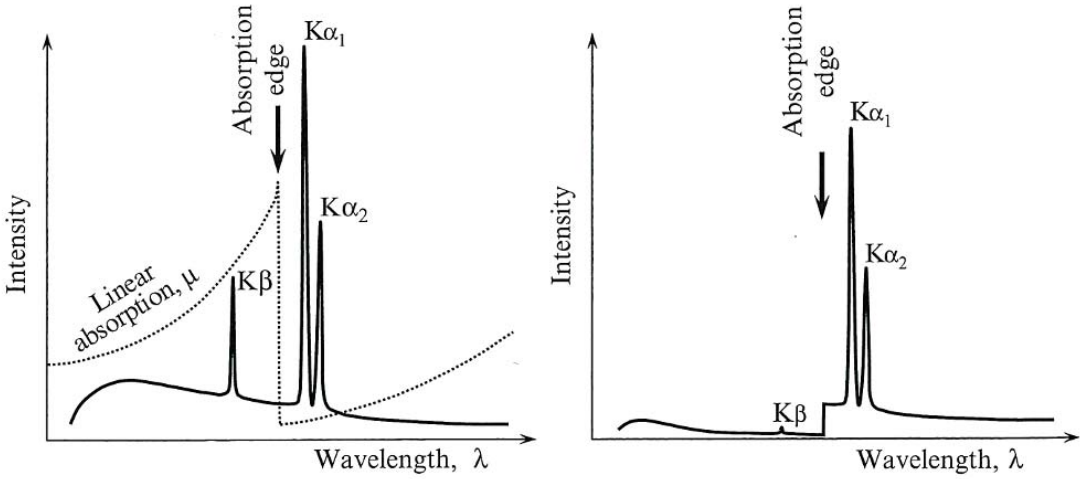

Figure 3.9. Illustration of the principle behind a beta-filter. The absorption edge lies just before the $K\alpha_{1,2}$ components. Figure taken from *Fundamentals of Powder Diffraction and Structural Characterization of Materials*, 2nd ed., by V. K. Pecharsky and P. Y. Zavalij, 2009, New York, USA: Springer. Copyright 2009 by Springer Science+Business Media. Adapted with kind permission from Springer Science+Business Media.

3.1.2.4 The detector

The detector's job is to record the diffracted X-rays and convert them to electrical signals. Depending on the applications, various different types of detectors are available. The three main types are point detectors, linear detectors, and area detectors.

The point detectors can measure the diffracted intensity at only one point along the 2θ scan range. Hence, they are quite slow and inexpensive. Common types are the gas-proprtional counter, the scintillator, and the solid-state detector. In the gas-proportional counter (which is used in Geiger counters to detect radioactivity) consists of a sealed chamber filled with a gas. A high electrical potential is applied over the chamber. The X-rays enter the chamber and ionize the gas, and the electrons are attracted to the positive anode. The resulting electrical signal is proprtional to the number of absorbed photons.

The scintillator, on the other hand, consists of a crystal coupled to a photomultiplier tube (PMT). Here, also, a high voltage is applied over the crystal. When the X-rays are absorbed by the crystal, visible light is emitted which enters the PMT. The PMT consists of a sequence of positively charged electrodes, called dynodes, with an increasing positive charge down the sequence of dynodes. Visible-light photon strikes the first dynode, and ejects a number of electrons from the dynode material, as according to the photoelectric effect. The ejected electrons are then attracted to the second dynode, and each electron ejects a certain amount of new electrons. These then continue to the next dynode, and hence a chain reaction start. The final electrical signal is proprtional to the amount of visible-light photons emitted by the crystal, and is hence proprtional to the amounts of X-ray photons absorbed by the crystal.

The solid-state detector uses a semi-conductor crystal, usually a lithium (Li) doped Si or germanium (Ge) crystal, over which a high voltage is applied. The crystal absorbs the X-rays, and electron-hole pairs are formed. Electrons travel toward the positive anode, and the electrical signal measured electrical signal is proprtional to the amount of absorbed photons. Solid-state detector needs to be cooled to around 80 K to reduce background and migration of Li. Energy resolution of solid-state detectors are very good, and monochromators are not necessary to filter out the Kβ component. Since even the best crystal monochromators reduce the K$\alpha_{1,2}$ intensities with a factor of 2, this energy resolution is a great advantage.

Linear detectors (also called line, 1D of point-sensitive detectors) cover a limited angular range of 2θ. Short-range detectors may cover up to 10° 2θ, while long-range detectors may cover as much as 140° 2θ. Modern gas-proprtional counters are able to measure the diffraction angle of the diffracted X-rays because of high-speed electronics. The signal follows two wires to the counting electronics, and depending on where on the anode the electrons hit, the time difference between the two wires is enough to deduce the angle. These need regular maintenence due to aging of ionization gas, and have a low linear dynamic range (Ermrich et al. 2011). A newer and better design is called real-time multiple-strip (RTMS) detectors. These operate in similar ways as the solid-state detector. A number of p-doped strips are placed on an n-doped wafer, and an electric potential is applied over each strip. Electron-hole pairs are formed in the strips where the X-rays are absorbed, and the applient potential makes the electrons travel to the positive anode, where the signal is measured. The electron-holes travel along a path of least resistance, and the current over the potentials at each respective strip provides positional information about the diffracted x-rays. Because an angular range is covered, data collection time is greatly reduced. Collection times of hours with point detectors may be reduced to minutes with linear detectors.

Area detectors are able to measure the diffracted intensity in two dimensions. They detect larger parts of the debye rings, and even complete rings at small bragg angles. Photographic film is an example of an area detector that is no longer commonly in use in routine laboratories, but modern replacements have been developed.

3.1.2.5 The autosampler

The autosampler, or sample changer, is a mechanism to choose, place, and replace various different samples. This automates the whole process, making sure the diffractometer can analyze five, 10, 20, or more samples without operator intervention. Different mechanisms exist, depending on manufacturer and patented designs.

3.1.2.6 The goniometer

The goniometer is the heart of the diffractometer. It usually consists of two arms, holding the X-ray source and incident-beam optics, and the detector and diffracted-

beam optics. One of the arms, or both, may move in a circular way around the center of the goniometer where the sample holder is placed. The diameter of the circle formed by the moving arms is called the goniometer diameter. The smallest angular step the goniometer arms may move accurately is the limit of angular resolution. The larger the goniometer diameter, the greater the angular resolution is; however, the X-rays will diverge more, air-scatter more, and lose intensity. Most goniometer have a radius of 150 mm to 300 mm

The goniometer may be designed in two different modes, depending on which of the arms move around, and whether or not the sample holder move. The two common goniometer settings are known as $\theta - 2\theta$ and $\theta - \theta$, and are presented in Figure 3.10 In $\theta - 2\theta$, the sample holder angle is synchronized with the movement of the detector; the incident beam is stationary. In the other mode, $\theta - \theta$, the sample holder is held horizontal, and both goniometer arm movements are synchronized. The modes get their names from the angles formed, as seen in Figure 3.10.

Figure 3.11 shows an example of a goniometer equipped with the components we have discussed in this section. This diffractometer is in $\theta - \theta$ mode, and uses two divergence slits in the incident beam, with soller slits in-between. In the diffracted beam we see an anti-scatter slit and a receiving slit, with soller slits in-between. No monochromator or beta filter is seen, but if the detector is of the solid-state type, this may not be necessary due to the excellent energy resolution. *R* in the figure refers to the goniometer radius, measured from the center of the sample to the start of the detector.

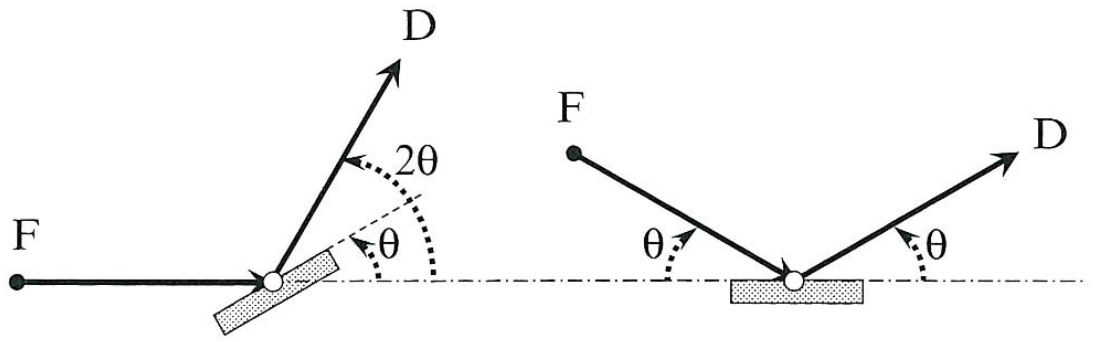

Figure 3.10. The two goniometer modes geometrically shown. Figure taken from *Fundamentals of Powder Diffraction and Structural Characterization of Materials*, 2nd ed., by V. K. Pecharsky and P. Y. Zavalij, 2009, New York, USA: Springer. Copyright 2009 by Springer Science+Business Media. Adapted with kind permission from Springer Science+Business Media.

3.1.3 Sample preparation

Proper sample preparation is extremely important to obtain a high-quality diffractogram. The smaller the particle sizes, the more random the crystallite orientations become, hence reducing the effect of preferred orientation and increasing counting statistics. However, if the particle size is too small, the crystallinity becomes weaker

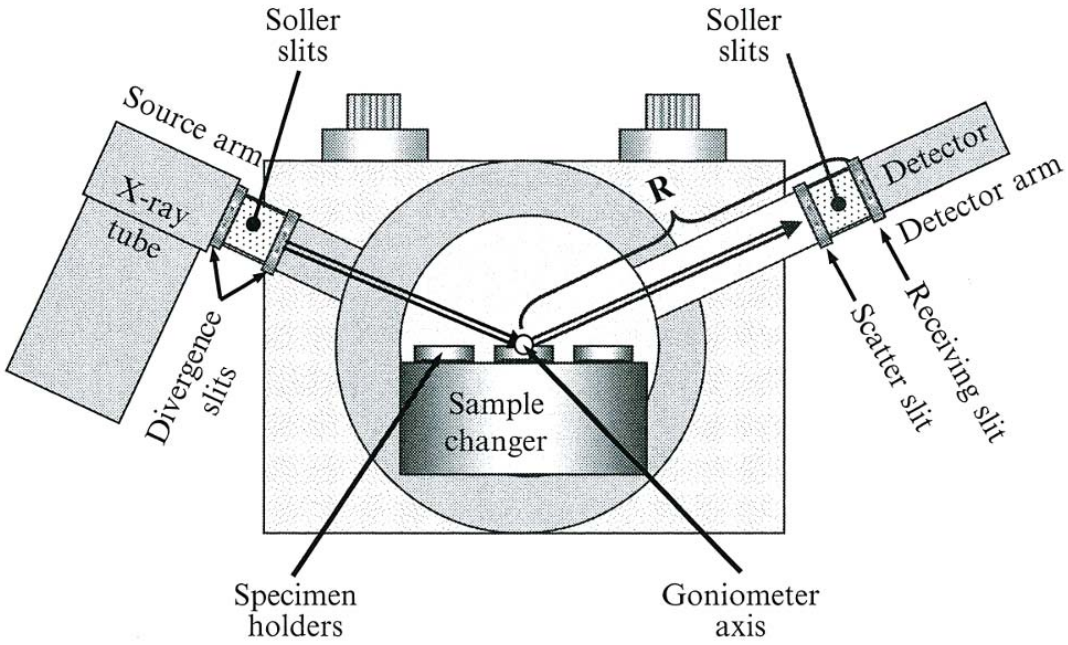

Figure 3.11. Example of goniometer with attached components. *R* refers to the goniometer radius. Figure taken from *Fundamentals of Powder Diffraction and Structural Characterization of Materials*, 2nd ed., by V. K. Pecharsky and P. Y. Zavalij, 2009, New York, USA: Springer. Copyright 2009 by Springer Science+Business Media. Adapted with kind permission from Springer Science+Business Media.

and resolution is reduced. A solid sample may be grinded by using a mortar and a pestle, but mechanic mills are available too. Mortars and mills should of course be kept as clean as possible to avoid contaminating the sample. Particle sizes should not be too small, as the particles may start to agglomerate, and too much grinding may degrade the crystallinity of the powder. Heat treatment may be able to restore the crystal structure in some cases.

Not just powder samples can be analyzed. During workplace air assessments, aerosols are deposited on filters, which can be put on a filter holder and placed in the instrument. Very little preparation of filter samples is necessary.

3.1.4 Data acquisition

Data collection means setting up the method and starting the diffractometer. Various different scan modes exist, examples of which are the step scan and the continuous scan. In a step scan, the goniometer arms move a defined step size and measure the diffracted intensity for a defined amount of time. Measurement time is increased by reducing the step size and increasing the integration time per step. The step size determines the resolution of the resulting diffractogram. In a continuous scan, however, the goniometer arms do not stop at each step, but moves continuously at a speed defined by the operator. The resulting diffractogram is visually identical, but the data collection is slightly different. Instead of measuring the intensity at each step, the

software calculates the average intensity within the specified step size. For example, if the intensity at 10° 2θ is given, then this may be the average intensity at 9.99° and 10.01°, with a step size of 0.02°. In theory, the step scan mode is slightly more accurate, especially if the goniometer is misaligned.

The sample holder can also be set to spin throughout the scan. This reduces the effect of preferred orientation, and increases the counting statistics, because more bragg angles will be measured. Spinning speeds of 0.5 rpm to 1 rpm are common.

Longer scans give higher quality data, because statistical noise is reduced. This may lead to small peaks becoming visible, that would otherwise not be so. Increasing the scan time is an easy way to increase the quality of the diffractogram.

3.1.5 Phase identification

Environmental samples are rarily pure substances, but will rather contain several different crystalline compounds with different crystal structures, called phases. All of these compounds will contribute to the diffractogram. If the sample contains four different phases, the Bragg peaks of all four phases will be present in the diffractogram (granted all Bragg angles are found, and the intensity of each peak is large enough to be spotted). These peaks may overlap and further complicate the diffractogram. So how can we distinguish between the phases?

When using PANalytical's own software for phase identification, HighScore Plus, the phase identification process can be described in the following steps: data inspection, background determination/subtraction, Kα_2 stripping, smoothing, peak searching, profile fitting, and search & match analysis.

Data inspection

Data inspection usually invovles just visually inspecting the diffractogram and assessing its quality or suitedness for further analysis. Factors such as resolution, background, signal-to-noise ratio, comparing various samples, etc., could be considered.

Background determination/subtraction

The first step of the phase identification process should be either subtracting the background signals from the diffractogram, or simply determining and adding it to the observed intensity. If this is not done, false peaks present in the background variation may be wrongfully identified as a peak, or a peak may be wrongfully identified as background, during the peak seraching stage. Therefore, the background levels should be accurately determined. The background may be determined automatically by software algorithms, or manually by defining a set of background points along the diffractogram. The latter is more accurate, but takes more time. In clean and simple diffractograms, automatic background determination may be sufficient, but in complex mixtures with a lot of overlapping peaks, the background may need to be determined manually.

$K\alpha_2$ stripping

Because the peak splitting due to the presence of $K\alpha_2$, it may be necessary to mathematically subtract its contribution. Different algorithms exist that do the job slightly different. The software tries to subtract the $K\alpha_2$ component from the peaks, and not from the background. However, modern software is able to take peak splitting into consideration when searching for peaks, and $K\alpha_2$ stripping may therefore not be necessary.

Data smoothing

For poor quality samples, or when very little sample material is available, the diffractogram may contain a lot of statistical variation. Smoothing the date involves eliminating this statistical variation, thus "smoothing out" the data. This process will decrease the resolution somewhat, depending on the amount of smoothing, and may affect phase identification. However, the diffractogram may look much cleaner afterward, and may be more "presentable".

Peak searching/manual peak identification

Searching for peaks are done either automatically or manually. Automatic peak serach usually involves calculating the double differential of the diffractogram, and evaluating how it varies with 2θ, and in that way detecting when peaks start and stop. The background is also taken into account when identifying peaks. Various criteria can be set to adjust the automatic peak search, such as minimum significance, minimum base width, minimum intensity, etc. The software may not identify all peaks, or may identiy peaks that are just background noise. In manual peak search, the operator locates the positions of the peaks visually, and inserts them by using the mouse. Doing this manually takes more time, but ensures that all necessary peaks are identified.

Profile fitting

After the peaks have been identified, a calculated profile is fitted to the observed data, based on the determined background and placement of the peaks. Several different algorithms exist that result in slightly different profiles, using different peak-shape functions to approximate the observed diffractogram. The profile is, at least in the case of PANalytical's HighScore Plus software, refined iterativelly, getting closer to the observed data for each run. The fitting process is usually runs for about 20 cycles. After the fitting process is done, some single-peak refinements may be necessary to optimize the peak shapes and peak positions of the calculated profile.

Search & match analysis

This stage involves searching for matching phases in a crystallographic database. Characteristics of the calculated profile are matched against the database phases, and the best matches are sorted in a list based on a matching score. It is important to remember

that any phase matching the profile may turn up as a prime candidate; the software does not take realism into account. An "exotic" phase, only ever detected from remote places under extreme conditions, may pop up as a prime candidate, but may not actually be present in the sample.

It is up to the operator to consider the candidates and decide on which ones are likely to be present. Diffraction data of candidates are available for all candidates, and factors such as collection temperature and pressure should be kept in mind; some phases are collected using non-ambient X-ray diffractometry, and *may* thus be unlikely to be present in the sample. In addition, the operator should be aware of any asymmetry in the peaks, which may indicate impurities in the crystal structure, such as solid solutions or substituted atoms, which results in tensions in the crystal structure, which affects the peaks.

Another thing that complicates matters, is that two phases may have overlapping peaks. Thus, after a peak has been labeled as "explained", another phase may still be explained by parts the peak. Indications of this may be that the peak originating from two phases exhibit an intensity that does not match the intensity ratios of the pure candidate diffractogram, or the peak may be of a different shape than the rest originating from the phase. Another way to spot this is by evaluating the "residual" calculated by the software: When the entire peak is explained by a phase, the residual is zero. If it the residual is non-zero, this may indicate that a minor phase is buried by the major phase.

It is important to have as much knowledge of the sample as possible when deciding which candidates are present. Knowing how the sample was taken and prepared, can yield information that helps eliminating certain candidates. Having performed elemental analysis, using e.g. ICP-techniques or X-ray fluorescence spectrometry, is also very helpful. Knowing the major and minor elements of the sample helps eliminating a lot of candidates.

The search can also be limited to just certain elements of the periodic table, or to groups of elements such as "transition metals", "inorganic", or "minerals". Forcing restrictions on the search can help bring the true candidate up the lists, but also hide a candidate if poor restrictions are set.

3.1.6 Challenges

3.1.6.1 Overlapping peaks

The large number of crystalline compounds present in some samples complicates phase identification. Peak overlap takes place when the crystal strucure of two crystalline compounds satisfy the Bragg equation at the same, or similar, Bragg angles. This is especially challenging when weak peaks from minor phases overlap with strong peaks from major phases; the weak peak is completely buried and invisible. Software may be able to detect such minor phases by calculating a "peak residual" by subtracting

the theoretical peak area for the phase with the observed peak area. If the residual is non-zero, a residual peak is displayed which may be detected by the software. However, peak properties such as intensity, resolution, Bragg angle, and shape may be heavily distorted, which may lead to incorrect phase suggestions by the software. Minor phases detected in this manner are therefore associated with larger uncertainties.

3.1.6.2 Limited knowledge about the sample

The diffractometer does not give the molecular composition of our samples, but rather just deduces the crystal structure. A lot of chemically different crystalline compounds have very similar unit cell parameters, and hence the candidate list will feature a lot of irrelevant suggestions of phases — "noise". Identifying unknown phases in the sample means going through these candidates and consider whether they fit the context. It is very helpful to know something about which elements are present in the sample, before starting XRD analysis. Therefore, results from element determinations with ICP-OES (or other atomic spectrometry techniques) should be considered when performing search & match analysis. This way we can limit the search to include the elements we know are present.

Accepting a phase as "present" is not a straightforward process; careful consideration is necessary. Factors such as "analysis temperature" and "analysis pressure" need to be looked up, and the resolution of the peaks in the diffractogram should match those of the reference pattern. If the widths differ slightly, this may indicate impurities in the crystal lattice. In the production halls of FeMn, the aloy is molten and warm. Solid solutions may take place, meaning that some Fe may be dissolved within a Mn oxide crystal lattice, or the other way around. Such considerations complicate the phase identification process, but are necessary to ensure an accurate analysis. Thus, as much knowledge about the sample material greatly benefits XRD analysis.

3.1.6.3 Sample fluorescence

Sample fluorescence occurs when the X-ray beam, which we hope will interact elastically, interacts inelastically with the electrons and ionizes the sample. When an electron from a higher shell fills the vacancy, the sample fluoresces; that is, emitting radiation with total energy equal to the energy difference in the energy levels. The fluorescence is both low-energy and high-energy radiation: long waves are emitted because the electron falls via the closely spaced energy levels *within* a main shell, while short waves (X-rays) are emitted when the electron falls from one main shell to another (e.g., L $\rightarrow$ K)

The probabilty of sample fluorescence increases as the X-ray's energy gets close to the binding energy ejected electron (Fransen 2004). Fluorescence occurs in all directions, and will hence be detected at all steps in the angular range, adding to the continuous background. Hence, this effect needs to be minimized. Although the fluorescence will always be present, its detection can be reduced in different ways:

adding a monochromator between the sample and the detector; switching to an X-ray tube with a different anode material; adding filters between the sample and the detector; or changing the spectral detection range of the detector. The last option is what was used in this thesis, and so it will be explained a bit further.

The detector does not detect the incoming signals continuously, but in pulses. This is because the detector needs to spend some time resetting itself after each detection. The time this resetting takes is called the "dead time", during which the signals pile up. These pulses may have different intensities, some of which are irrelevant in our analysis. Pulse-height discrimination (PHD) is the process used to limit the detected signals, and in that way suppress the unwanted fluorescent radiation.

3.1.6.4 X-rays hitting the sample holder

Because of the penetrating ability of X-rays, care should be taken to ensure that the material supporting the powder does not contribute with any peaks. We want the peaks in the diffractogram to come from our sample exclusively, and not from some other crystalline material. "Zero diffraction" plates are specially designed Si crystals, cut at an orientation parallel to the 510 lattice planes[1] (Delgado et al. 2015), where the diffraction order is zero. This means that no diffraction occurs, and hence no peaks are present. However, X-rays are reflected and refracted by the crystal, and contributes to the background, although at very low levels. These properties make zero diffraction plates ideal to use when low backgrounds are needed.

3.1.6.5 Preferred orientation

Preferred orientation is a phenomenon that always occurs, depending on the sample. Certain particle shapes tend to *not* pack randomly, but prefers a certain orientation. Needle- or platelet-like particles, for example, have anisotropic shapes, and tend to pack in a distinct non-random way. This effect might greatly affect the diffracted intensity ratios, as not all bragg angles are available to the same extent, and may affect the search & match analysis.

3.2 Inductively coupled plasma optical emission spectrometry

ICP-OES is a technique capable of quantifying most elements of the periodic table in a sample. The sample needs to be in liquid form to be introduced to the ICP-OES system. This can be achieved by digesting the sample in acid in a microwave oven, which brings the analyte to a form that is dissolvable in acid or water. Acids commonly used include hydrochloric acid (HCl), nitric acid (HNO_3), and HF. Digestion takes place

[1] 510 is a notation of lattice planes in Miller Indeces. See chapter 1 in Pecharsky et al. (2009).

due to oxidation, reduction, and/or complex binding of chemical species. Maintaining the integrity of the molecular composition in the sample is not necessary, since it is the elements, not molecule, that are of interest. By heating the sample in a microwave, the sample is digested much faster than compared to digestion at room temperature. To obtain even faster digestions, the reactions can take place in closed systems under pressure. The digests are usually diluted, and are then ready to be introduced to the ICP-OES system.

After being introduced to the tubes, the sample reaches the nebulizer. Different kinds of nebulizers exist, but their function is the same: transform liquid sample into fine mist. A small particle size in the mist is desireable, and so the larger particles are removed from the aerosol in the spray chamber. Here, too, several different designs exist, but their function is the same: larger droplets are carried off to the drain, while the smallest droplets are carried to the plasma torch. The plasma torch usually consists of three concentric quartz tubes surrounded by a Cu coil. A radiofrequent field is applied to the coil, forcing charged and polar particles in the quartz tube to align to the field. A high-voltage spark causes a local ionization in the argon (Ar) gas, and Ar ions start colliding with adjacent Ar atoms as they continuously align to the shifting high-frequency field. The plasma grows by chain reactions of collisions between Ar ions and atoms until equilibrium is reached. The plasma is about 8000 K at its hottest. As the sample is introduced to the warm plasma the water evaporates, and the molecules are broken down to their elemental constituents. Heat excites electrons in the atom, and the radiation emitted when electrons de-excite propagate via the optical components to the detector. Energy levels in the atomic electronic structure are characteristic to the element. The plethora of emitted wavelengths are separated in polychromators, and are ultimately detected simultanesouly. The intensity of the detected wavelength is compared to calibration standards of known elemental concentrations, and quantification of elements is thus achieved.

For more informaion about the ICP-OES technique, the reader is referred to the works by Skoog et al. (2007, Chapters 8 and 10), Hou et al. (2000), and Thomas (2013).

3.3 Ion chromatography

IC falls under the more general term "liquid chromatography", but only IC is considered here. IC is a separation technique capable of separating and quantifying ions in a mixture. The separation is accomplished by the use of a "separator", usually a column. The inside walls of this column is packed with special compounds (stationary phase). As the sample matrix passes over the stationary phase, the ions are partitioned between the staionary phase and the solvent, and a state of equilibrium is reached after a given time. Ions with large partitioning coefficient, K_D, tend to distribute more in the stationary phase, while ions with smaller K_D tend to spend time in the solvent. When anions are to be separated, the staionary phase i positively charged, so as to attract the anions, and

vica versa for when cations are to be separated. Ion exchange takes place as the eluent interacts with the staionary phase, exchanging the ions bonded to the stationary phase with H^+ or OH^-, for anion and cation chromatography respectively. Small K_D ions are eluted first, and large K_D ions are eluted last.

The separated ions are detected by conductivity measurements. However, since the eluent concentration is much higher than the analyte concentrations, the eluent conductivity is suppressed before quantification takes place. This is achieved by converting the eluent from an electrolyte to a neutral species. The conductivity, measured in µS, is normally plotted against time or eluent volume used. Based on their K_D the anions appear at different times in the chromatogram. The integrated intensity is compared to calibration standards of known concentrations, and quantification is achieved.

For more detailed account of IC, the reader is referred to e.g. Skoog et al. (2007, Chapter 28) and Elkin (2014, Section 2).

4

Methodology

This chapter will present a site description, describe the sample collection procedures, analytical procedures in the laboratory, and the instrument methods used during analyses. Manufacturer and model of the instruments used can be found in Table A.1, and the purity and manufacturer of the chemicals used can be found in Table A.2, both tables in the appendix.

4.1 Site description

FeMn and SiMn production in Norway takes place at three different plants: Eramet Porsgrunn, Eramet Sauda, and Eramet Kvinesdal. The plant in Porsgrunn produces both FeMn and SiMn, while Sauda produces only FeMn and Kvinesdal produces only SiMn. All three plants use electric arc furnaces. In FeMn production, the main raw materials are typically Mn and Fe ores, coke, quartz, and dolomite. These are mixed at designated sites, and transported to and added to the furnaces.

The finished product is then tapped, crushed, screened, and packaged for sale. The

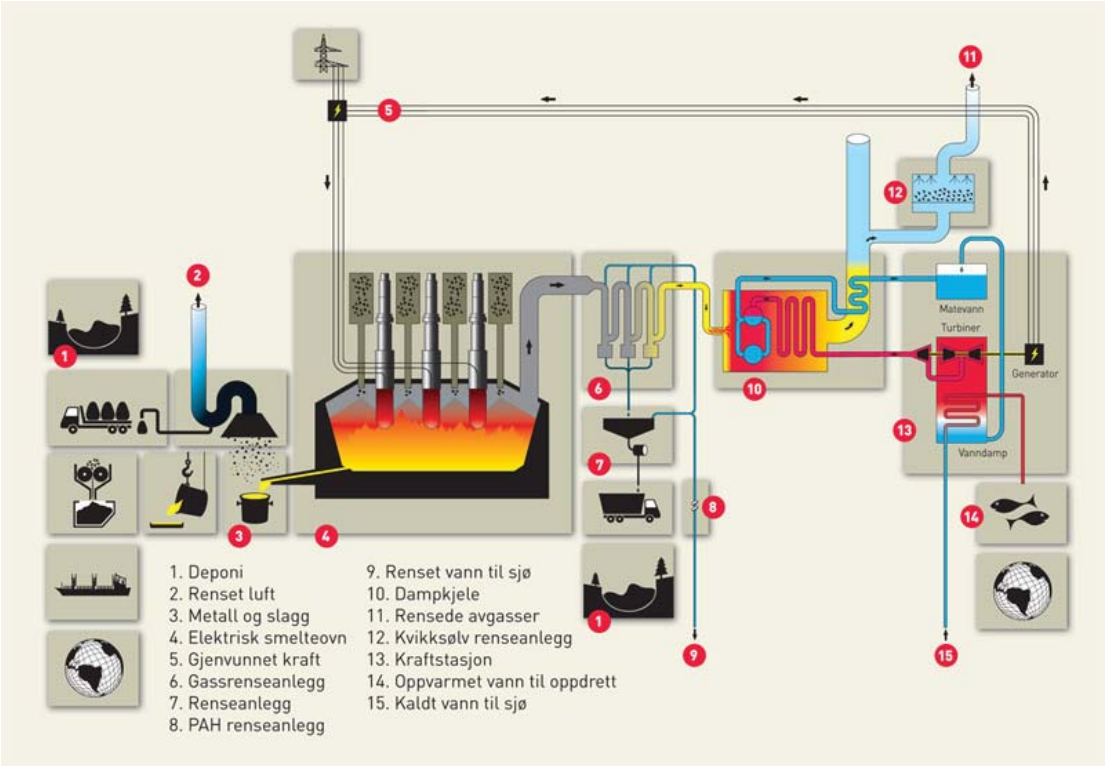

Figure 4.1. The FeMn and SiMn production process "at a glance" (Eramet Norway n.d.). Translation of Norwegain text: 1. Deposition site, 2. Refined air, 3. Metal and slag, 4. Electric furnace, 5. Recycled power, 6. Emission purification unit, 7. Refinement station, 8. PAH refinement station, 9. Refined water to sea, 10. Steam container, 11. Refined off-gasses, 12. Mercury refinement station, 13. Power station, 14. Heated water to fish breeding, 15. Cold water to sea.

FeMn slag contains muchMnO and is therefore reused as part of the charge for SiMn production. The charge used in SiMn production contains quartzite, coke, coal, and dolomite. After the slag is separated from the SiMn alloy, it is crushed, washed, and screened, and is ultimately used in cement manufacturing and concrete production. The whole production process of FeMn and SiMn alloys is summarized in Figure 4.1.

4.2 Sample collection

4.2.1 FFP samples

Furnace fumes are produced by evaporation of molten raw materials inside the furnace. These fumes are deposited as a powder inside the emission purification unit, from where the deposited powder was collected (see point 6 in Figure 4.1.) This powder was sieved using a 45 µm sieve.

4.2.2 TF samples

Tapping fumes were assessed by employing 25 mm air sampling cassettes in the FeMn and SiMn tapping area. The aerosols were collected on 25 mm in diameter and 5.0 µm pore-size polyvinyl chloride (PVC) membrane filters in a multiport air-sampler developed at NIOH, Oslo. The air samples were collected in batches of 27, with a collection time of approximately 24 h. Two batches were collected next to the FeMn and SiMn furnace tapping areas. The multiport sampler was connected to a high-capacity pump, and a 2 L min^{-1} air-flow rate through each sampling port was obtained using a critical orifice. The filters were kept over-night in a dedicated room with constant temperature and humidity, prior to weighing the filters before and after sample collection.

The multiport sampler was placed approximately five meters away from the furnace. A close-up image of the multiport sampler is shown in Figure 4.3, and Figure 4.2 shows the placement of the sampler next in the SiMn furnace tapping area. No image was taken of the sampler placement in the FeMn tapping area.

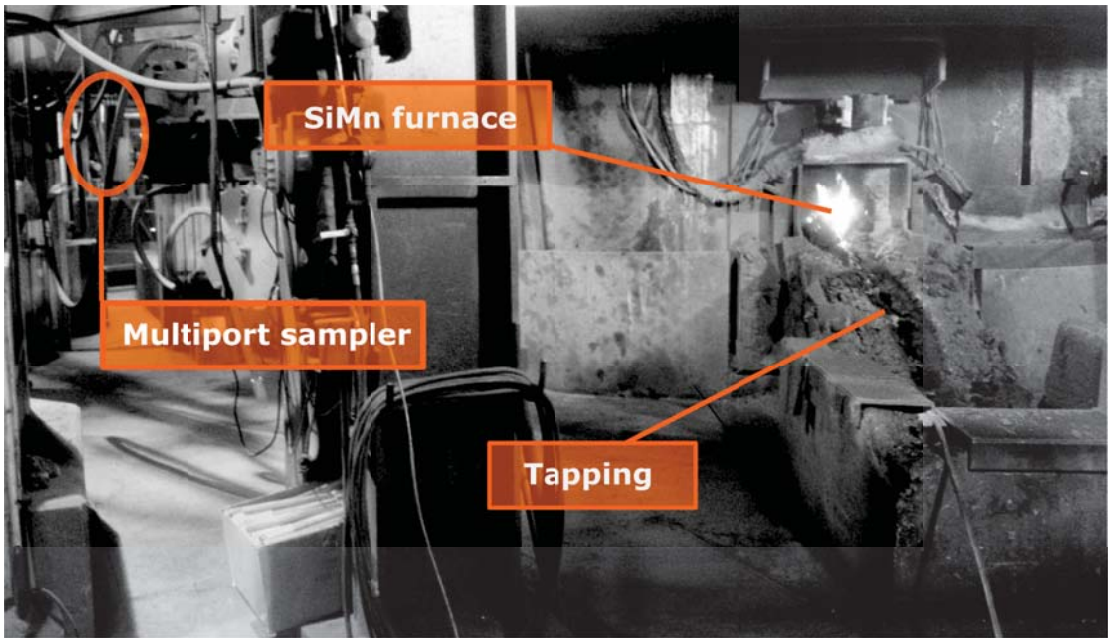

Figure 4.2. Placement of multiport sampler system in the SiMn tapping area in Porsgrunn. Approximate distance from the furnace tapping is 5 m. The sampler was placed approximately 1.5 m above ground, measured at the bottom-most tip. The sampler, the metallic cone-like shape, is shown in the orange circle. In addition the furnace opening and tapping runner is shown on the right.

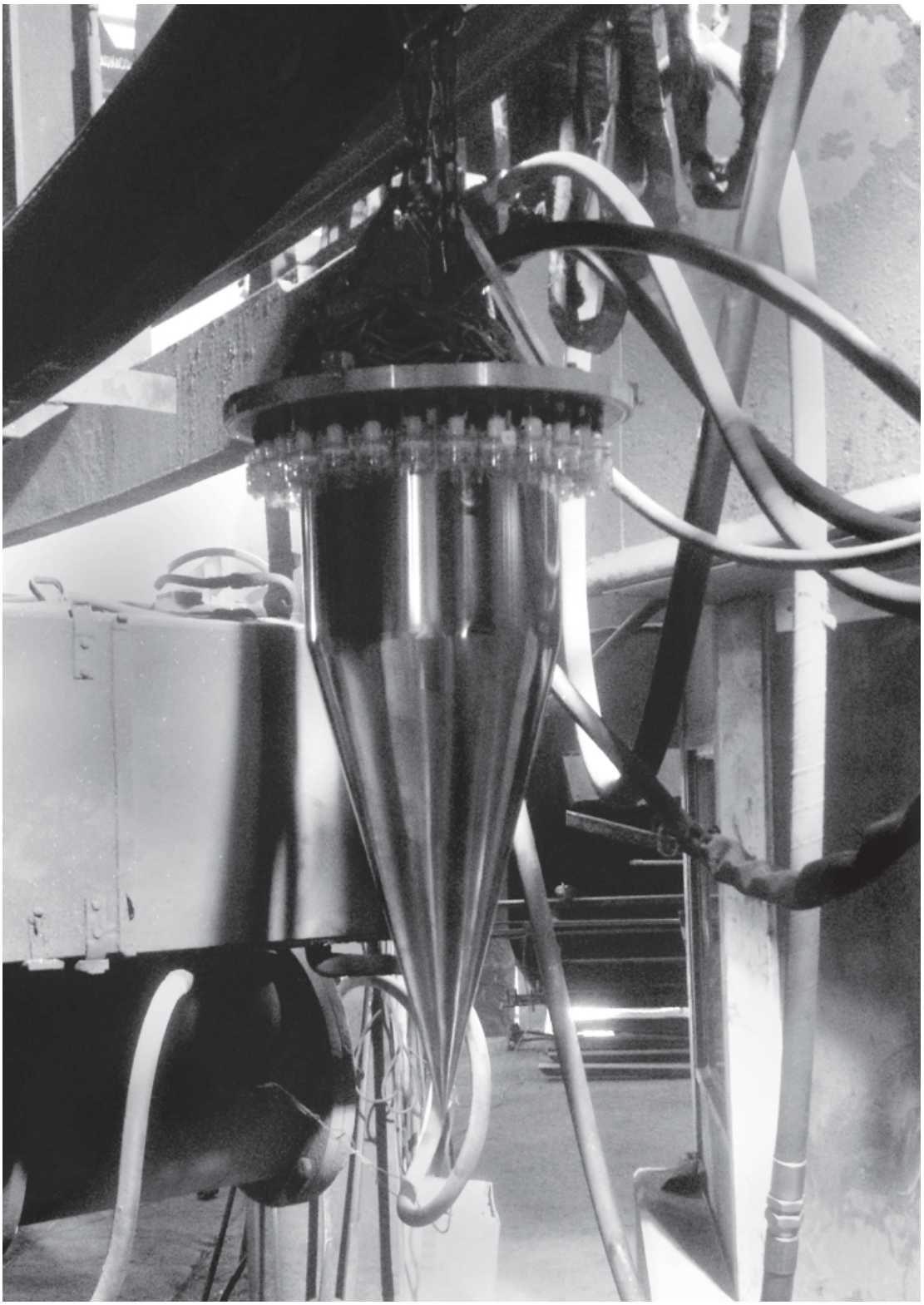

Figure 4.3. Close-up of the multiport sampler cone (37 parallel samples). The millipore filter cassettes are mounted around the upper part of the cone, as shown in the image. A metal cover was secured over the cassettes to protect the filter cassettes before sampling started. The pump was connected to the top of the cone.

4.2.3 PEF samples

The personal expsure filters were mounted in cyclones collecting the respirable aerosol sub-fraction. The cyclones were placed the breathing zone of the workers and connected to a pump. 25 mm PVC membrane filters with a 5.0 µm pore-size were used during sample collection. The filters were kept over-night in a dedicated room with constant temperature and humidity, prior to weighing the filters before and after sample collection.

4.3 XRD analyses

4.3.1 Optimizing the method

To optimize the signal-to-noise ratio, three pre-experiments were carried out: a) testing of different sample plates that holds the filter in place during analysis, b) testing of different filters used to collect aerosol samples, c) and optimizing the pulse-height discrimination levels.

4.3.1.1 Testing of sample plates

The following plates were tested: Al plate, cellulose membrane filter, single crystal Si manufactured by PANalytical, and single crystal Si manufactured by MTI Corporation. The single crystal Si plates are specially designed to give near-zero background, as mentioned in the theory chapter. The results from this comparison can be seen in Figure 4.4. The PANalytical single crystal Si plate was chosen for all subsequent XRD analysis presented (henceforth referred to as the Si plate).

4.3.1.2 Testing of filters

Different filter materials were analylzed to see which gave the lowest background signals. Three different filters were tested (all manufactured by Millipore): a) 5.0 µm pore-size and 25 mm ø PVC filter, b) 0.5 µm pore-size and 25 mm ø PTFE filter, and c) 0.4 µm pore-size and 25 mm ø PC filter. The results are presented in Figure 4.5, along with the diffractogram of the Si plate. Where relevant, the PVC filters were chosen for all subsequent XRD analyses.

4.3.1.3 Optimizing pulse-height discrimination settings

To limit the detection of sample fluorescence, the PHD settings of the detecter were optimized, inspired by Fransen (2004). A continuous scan-mode was used, the step size was 0.039 39°, and the time-per-step was 10 s. 0.04 rad soller slits were used in both

incident and diffracted path, and programmable anti-scatter slits were used in both incident and diffracted path, where both irradiated and observed length were set at 15 mm.

The PIXcel ^{1D} detector's lower level (LL) and upper level (UL) are placed on a scale from 0 % to 100 %. During optimization, the UL was held constant at 80 %, and the LL was tested at 30, 35, 40, 45, 50, and 55 %, respectively. The peak-to-noise (PTN) ratio was estimated by reading the number of counts at the top of the highest peak, and dividing by the number of counts at background level at 90° 2θ. This angle was chosen because air-scattering of X-rays is likely to be negligible at this high angle Fransen (2004). The PTN ratios are presented in Table 4.1, and based on these results, a LL of 45 % was chosen for all XRD patterns presented in the this thesis. The diffractograms are presented in Figure B.1 in the appendices.

4.3.2 Sample preparation

4.3.2.1 FFP

The FFP was suspended in ethanol (*pro analysi*) using a ultrasonic wave-generator, and filtrated onto a 25 mm in diameter and 5.0 µm pore-size PVC membrane filter. This was done using a water aspirator connected to a faucet and a water-suction filtration system, similarly to what is described in ISO 15202-2 (ISO/IEC 2012, Annex B). Approximately 9 mg powder was deposited on the filter.

For comparisons with the diffractograms, Mn_3O_4 powder was prepared in the same way as described above. About 10 mg of powder was deposited on the filter.

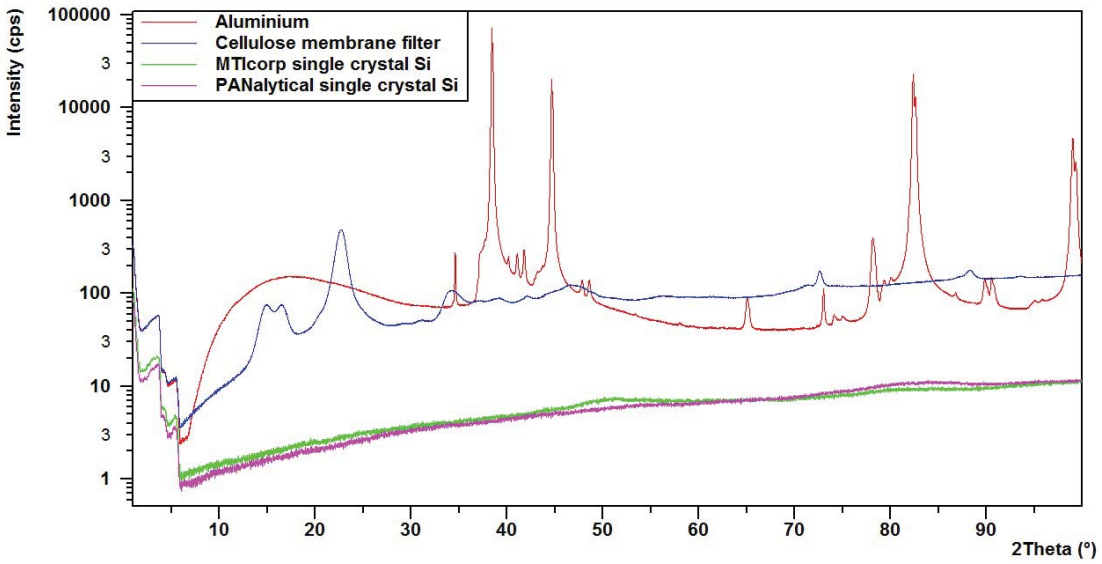

Figure 4.4. Four different materials for a sample plate were tested: Aluminium, cellulose membrane, and two single crystal Si plates of different manufacturers. It is clear that the single crystal plates are superior in their low background levels. The intensity in counts per second i plotted logarithmically.

Table 4.1. Optimization of pulse-height discrimination settings. A continuous scan-mode was used, and the lower level PHD setting was varied, while the upper level was kept constant at 80 %.

Lower level [%]	Peak-to-noise ratio
30 %	1.71
35 %	2.62
40 %	7.13
45 %	20.8
50 %	13.8
55 %	3.65

4.3.2.2 TF samples

The PVC filters were taken out of the cassettes and placed in the XRD sample holder on a Si zero-diffraction plate. To increase the signal from the aerosol particles on the filters, three filters were stacked together on the Si plate.

4.3.2.3 PEF samples

The PVC filters were treated as the aerosol filters, but were not stacked. This was to prevent contamination between filters, as they were to be used for chemical analyses outside the scope of this thesis.

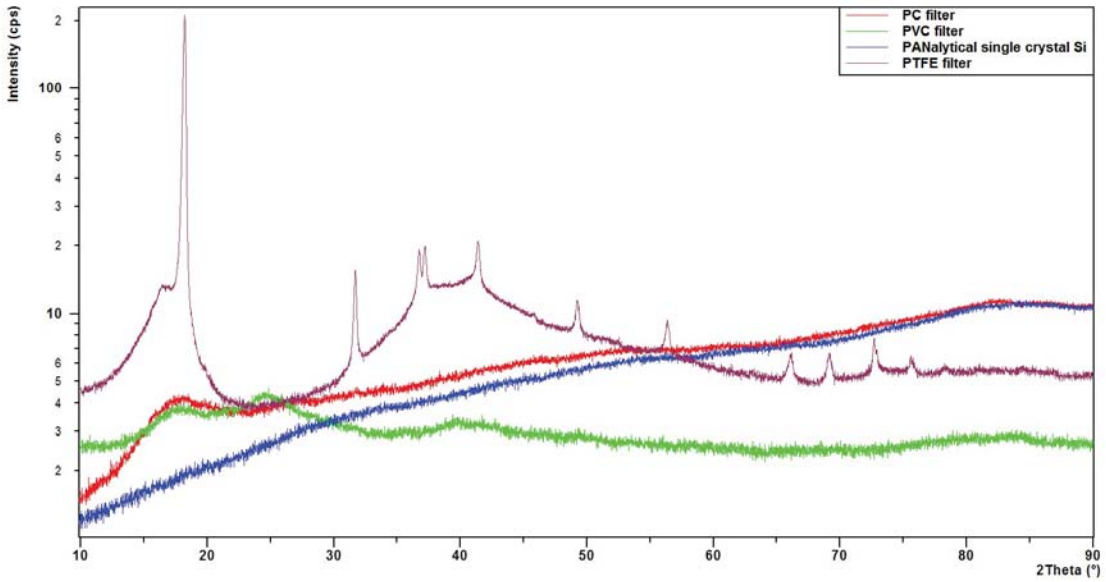

Figure 4.5. Background levels were checked for three different filter materials: PVC, PTFE, and PC. The PVC filter gave the lowest background of the three filters.

Table 4.2. Scan settings for the three different sample types analyzed in this thesis. A continuous scan-mode was used for all scans.

Sample	Scan range [°]	Step size [°]	Time per step [s/°]
FFP	1–100	0.0131	250
TF	10–90	0.0263	2500
PEF	1–100	0.0263	600

4.3.3 Instrument method

A PANalytical X'Pert^3 Powder diffractometer, equipped with a PANalytical Empyrean X-ray tube in line-focus mode, was used for all XRD analyses. Characteristic Cu radiation was used. A two-arm goniometer with a 240 mm radius was used to hold the following components:

- Incident beam path: 0.020 mm Ni beta filter, 0.04 rad soller slits, 11.60 mm beam mask, and a programmable divergence slit
- Diffracted beam path: Programmable anti-scatter slit, 0.04 rad soller slits, and a PIXcel^{1D} RTMS detector

During all scans the instrument was operated at 45 kV and 40 mA. Based on the PHD optimalization, the PHD lower and higher levels were set to respectively 45 % and 80 %. A continuous scan mode was used for all XRD analyses. The individual scan settings for furnace fume powders, aerosol filters, and personal exposure filters are given in Table 4.2.

4.3.4 Phase identification

The diffractograms were loaded into HighScore Plus software. Because the samples were analyzed using an automatic divergence slit, and not a fixed one, a slit correction-algorithm was applied to the diffractograms. Background levels were determined manually, and peaks were identified manually by visual inspection. A profile was fitted to the observed data, which was compared to a search-and-match version of the Inorganic Crystal Structure Database (FIZ Karlsruhe 2014) for phase identification.

Based on elemental analyses of the FFP and TF samples, the Search & Match analysis was restricted to C, K, Na, Ca, Mg, Mn, Fe, Zn, Si, S, and O to prevent irrelevant elements from dominating the candidates list. This restriction was also used for the PEF samples, although no elemental analyses were performed for these samples.

4.4 Elemental analyses

4.4.1 Sample preparation

The method for elemental analysis presented here is routinely used at NIOH, Oslo, and has been previously validated. No quality control samples or certified reference materials were therefore used to assess the accuracy of the analysis.

Six parallels of FeMn and SiMn FFP were prepared and digested as described below. Approximately 10 mg portions of powder were weighed onto PVC filters, which were placed in teflon digestion vessels (see Table B.5 for actual amounts weighed in). In addition, three FeMn and SiMn TF samples were digested in the same way. 2.00 mL *aqua regia* and 0.200 mL HF was added to each vessel, and a known amount of Be was added as an internal standard. The autoclaves were run at Program 1, and taken out and shaken before run at Program 2. See Table 4.3 for a summary of the programs. The digests were diluted to 14 mL with de-ionized water. Unused PVC filters from the same batch were digested in the same way as described above, and served as blank filters, which were subtracted from the FeMn and SiMn sample concentrations. Multielement calibration standards were prepared from stock solution manufactured by Spectrapure Standards.

Table 4.3. Summary of program settings for the microwave digestion system.

Program	Duration [min]	Power [W]
Program 1	5	250
	10	500
Program 2	5	250
	10	500
	5	250
	10	500

Three parallels of both FeMn and SiMn FFP water-extract were analyzed. The extraction process is described in Section 4.5. The same multielement calibration standard used for analysis of FFP was used for analysis of the water-extract.

4.4.2 Instrument method

Table 4.4. Analytical emission lines used for elemental analyses

Element	Emission wavelength [nm]
Al	308.213
Al	394.401
Al	396.157
Ca	315.889
Ca	317.931
Ca	422.671
Fe	234.349
Fe	238.200
Fe	259.942
Fe	239.570
K	766.509
Mg	280.267
Mg	279.079
Mg	285.210
Mn	257.606
Mn	260.564
Mn	294.924
Na	589.597
Pb	216.996
S	181.975
S	180.669
S	182.563
Si	212.412
Si	251.608
Si	288.158
Zn	206.196
Zn	202.546
Zn	213.855

For all elemental analyses a PerkinElmer Optima 7300 Dual View ICP-OES spectrometer was used, equipped with a cross-flow nebulizer and a Scott dual-pass spray chamber. The detector was an echelle-based polychromator segmented-array charge-coupled device. The analytical emission lines used for calibration and quantification are presented din Table 4.4. Plasma gas flow was operated at 15 L min^{-1}, auxilliary gas flow at 0.2 L min^{-1}, and nabulizer gas flow at 0.90 L min^{-1}. Sample and wash flowrate was 1.50 mL/min, wash time was 60 s, and washing was performed between every sample. The torch power was 1500 W for all analyses, and the viewing distance to the plasma was 15 mm. All analytes were viewed radially except for Pb which was viewed axially. Radial viewing of the Be 313.042 line was used as internal standard for all elements. Two replicate readings were performed by the instrument for each emission line analyzed. Calibration equations for each element were linear and forced through zero. Peak area, based on three points per peak, was used for quantification, and a two-point background correction was used for all emission lines.

4.5 IC analyses

4.5.1 Sample preparation

Three parallel samples of FeMn and SiMn water-extract were prepared. Water-soluble ions were extracted in 50 mL Vectaspin centrifuge tubez with a 0.45 µm filter attached. The weighed-in amounts of powder and milli-q water are given in the appendix (Tables B.1–B.4).

The water-soluble anions were identified from a pre-experiment as chloride (Cl^-), fluoride (F^-), and sulfate (SO_4^{2-}). Since F^- and Cl^- are strong complex-binders, three parallels of FeMn and SiMn water-extract were spiked with all three anions to asses the recoveries of these anions after extraction. The spiked concentration was approximately the same as the inherent anion concentration in the water-extract. Therefore, the spiked samples were also diluted 2x so that no extension of the calibration curve would be needed. Note that spike was added *after* extraction. Recovery of spike was calculated in the following way:

$$R = \frac{\text{Moles of analyte in spiked sample} - \text{Moles of analyte in unspiked sample}}{\text{Theoretical number of moles of added spike}} \cdot 100\,\% \tag{4.1}$$

All FeMn water-extracts were diluted 40x, and all SiMn water-extracts were diluted 10x (by weighing, see Tables B.2 and B.3 in the appendix).

Duration of extraction by gravity was approximately 24 h, after which all samples were centrifuged at a relative centrifugal force of 203 g for two minutes. Repeating of extraction to check if all water-soluble anions were extracted, was not performed.

A calibration curve was constructed based on calibration standards of 0, 1, 3, 5, 10, 20, 32, and 50 $\mu g\,mL^{-1}$, respectively. To assess the accuracy of the analysis, a set of quality control samples of approximately 13 $\mu g\,mL^{-1}$ and 25 $\mu g\,mL^{-1}$ were prepared from the same stock solutions used for preparing calibration standards. A known amount of phosphate (PO_4^{3-}) was added to all samples as internal standard (added to water-extracts *after* extraction).

4.5.2 Instrument method

A Dionex 2100 Ion Chromatography System (ICS), coupled to a heated conductivity cell, was used to identify and quantify the anions in the water-extracts. The ICS used a hydroxide-selective anion-exchange column (2x250 mm) to separate the anions, coupled to a 2x50 mm guard column of the same type. More information about the columns can be obtained in the product manual (Dionex Corporation 2012). The suppressor used was an anion self-regenerating suppressor (Dionex ASRS®300, 2 mm). A Dionex EGC III Eluent Generator Cartridge providing KOH was used for the analysis, and freshsly prepared de-ionized water was used as solvent. Isocratic eluation was used.

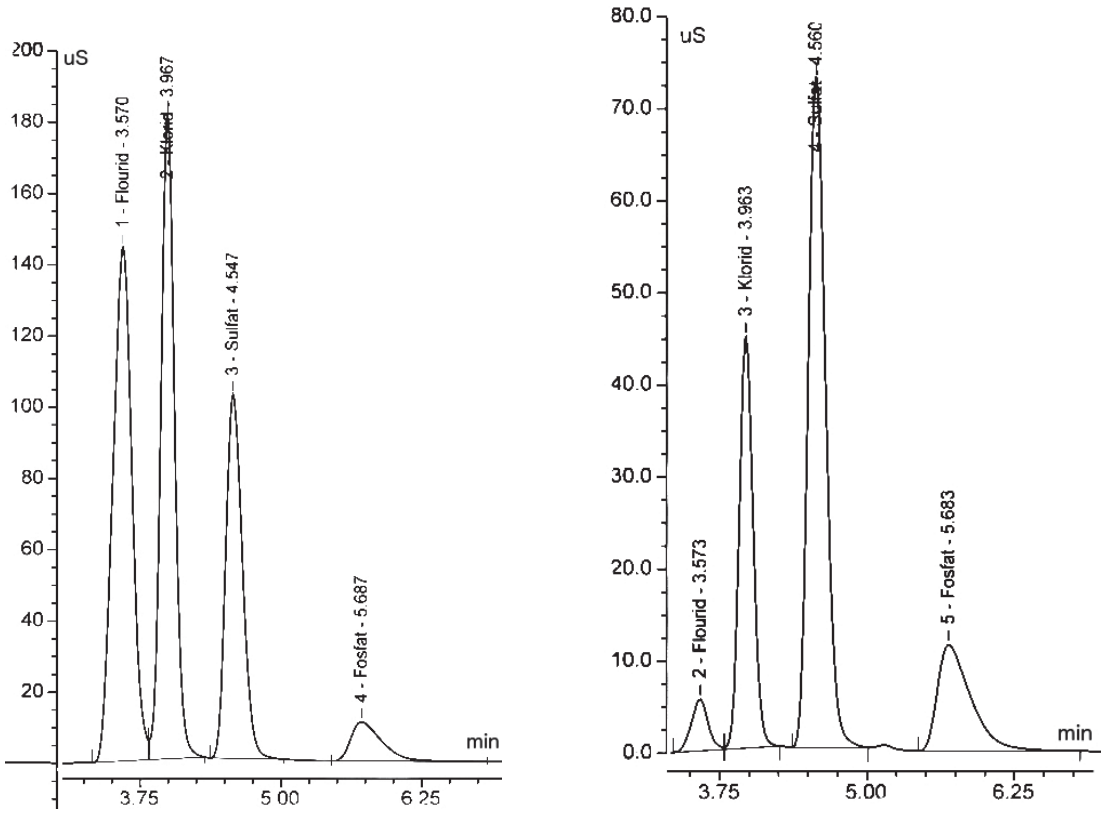

(a) 50 µg mL^{-1} calbration standard

(b) Parallel of SiMn FFP water extract

Figure 4.6. Chromatograms of a calibration standard and a typical water extract. Peaks 1, 2, 3 and 4 belong to F^-, Cl^-, SO_4^{2-}, and PO_4^{3-}, respectively.

The instrument settings are summarized in Table 4.5. The separation achieved can be seen in the chromatograms in Figure 4.6.

Table 4.5. Instrument settings used for the ion chromatographic analysis

Factor	Setting
Column flow	0.25 mL/min
Run time	10 min
Injection volume	10 µL
Number of injections per sample	2
Eluent concentration	18 mmol L^{-1}
Data collection rate	5.0 Hz
Cell temperature	35 °C
Column temperature	30 °C
Suppressor current	12 mA

4.6 pH measurements

1.002 70 g FeMn FFP and 45.003 03 g de-ionized water was weighed into a 50 mL tube, shaken well, and allowed to rest overnight. 1.003 88 mg SiMn FFP and 45.988 16 mg de-ionized water was treated in the same way as described for the FeMn FFP. The water-powder suspension was filtrated through a 0.45 µm filter by water-suction filtration, similarly to what is described in (ISO/IEC 2012, Annex B). The pH was measured in the extracted solution.

A three-point calibration was performed just before the measurements, using the following pH buffer solutions from HACH: pH 4.1 ± 0.02, pH 7.00 ± 0.02, and pH 10.01 ± 0.02. The electrode was thoroughly rinsed with de-ionized water between each measurement. Measurements of pH in reference solutions were not performed.

5

Results

5.1 XRD analyses

The detected phases have been termed "major" or "minor", but no objective measure was used to distinguish between the two; each diffractogram was considered individually. Hence, a major phase in the samples from Sauda might have been called a minor phase if present in the FFP samples.

The XRD spectra collected from the FFP, TF, and PEF samples are presented in Figures 5.1–5.5. The FeMn and SiMn FFP diffractograms have been plotted together, and the same was done to the FeMn and SiMn TF diffractograms. The PEF analyzed from Eramet Porsgrunn, Sauda, and Kvinesdal were grouped together with their respective parallels. All diffractograms referred to in the text are sequentially presented starting from Page 51. This was done to prevent breaking up the text. Due to little sample material on the filters from Kvinesdal (see Table B.7), no phases were detected.

Hexagonal quartz (hence β-quartz) dominate both FeMn and SiMn FFP samples, as is seen from its highly intense peak at 26.6° 2θ in Figure 5.1. β-quartz was also detected in both TF samples. More β-quartz was detected in the FeMn FFP than in the SiMn FFP, as is illustrated in the zoomed-in view of the 26.6° 2θ peak in Figure 5.7 In addition, α-cristobalite, a high-temperature polymorph of silica, was detected on one of the PEF samples from Porsgrunn (sample #026). A zoomed-in view of the most intense cristobalite peak can be seen in Figure 5.6, plotted with the other PEF samples from Porsgrunn for comparison.

In addition, hausmannite (Mn_3O_4, tetragonal) was detected in most samples. By plotting a reference spectrum of hausmannite with the FeMn FFP, many overlapping peaks are observed (Figure 5.8). This is also seen by plotting the hausmannite reference spectrum with SiMn FFP and FeMn TF samples(Figures 5.9 and 5.10), although to a smaller extent. The detected hausmannite in SiMn FFP contained some Fe, which may explain why the Mn_3O_4 reference pattern shows peaks that do not match. Hausmannite was not detected in any of the SiMn TF samples. Hausmannite was detected on all PEF samples from Porsgrunn, but not in the ones from Sauda. However, another Mn oxide, bixbyite (Mn_2O_3, cubic), was detected in one of the PEF samples from Sauda.

Magnetite (Fe_3O_4, cubic) was only detected in SiMn FFP, although two different crystal structures of magnetite were detected: cubic and monoclinic. However, magnesioferrite ($MgFe_2O_4$) was detected in several samples, including both FeMn and SiMn TF, and in PEF sample #008 from Sauda. The most intense peak of magnesioferrite is shown in a combined diffractogram of the Sauda samples (Figure 5.11), showing that the peak is absent from the other samples.

Arcanite (K_2SO_4, orthorhombic) was detected as a major phase in several samples, including the FeMn FFP, all four PEF samples from Porsgrunn, and on PEF samples

Table 5.1. Detected phases in FeMn and SiMn FFP samples, TF samples, and PEF samples from Eramet's production in Porsgrunn, Sauda, and Kvinesdal. Eramet Sauda only produces FeMn, and Eramet Kvinesdal only produces SiMn.

Sample	FeMn	SiMn
FFP		
Major	Mn_3O_4, SiO_2, K_2SO_4	Fe:Mn_3O_4, SiO_2, Fe_3O_{4cubic}
Minor	$MgCO_3$	$Fe_3O_{4monoclinic}$
TF		
Major	—	—
Minor	Mn_3O_4, SiO_2, ZnS, $MgFe_2O_4$	MgO, SiO_2, $MgFe_2O_4$
PEF Porsgrunn		
Major	K_2SO_4, ZnO, Mn_3O_4	K_2SO_4, ZnO, Mn_3O_4
Minor	$SiO_{2cristobalite}$	—
PEF Sauda		
Major	K_2SO_4, ZnO, MgO, Mn_3Si	—
Minor	CaS, $MgFe_2O_4$, Mn_2O_3	—

#002 and #008 from Sauda. The three most intense peaks of arcanite can be seen for FeMn FFP and sample #026 from Porsgrunn in Figure 5.12.

Zincite (ZnO, hexagonal) was detected as a major phase on all PEF samples from Porsgrunn and Sauda. Visual inspection of the diffractograms reveals that the most intense peak of hexagonal ZnO is indeed present in all samples (Figure 5.13). Although sample #008 looks to be slighly shifted to the left, the ZnO was detected.

PEF sample #007 from Sauda differed from the other Sauda samples, as is clear from Figure 5.4. In addition to zincite, oldhamite (CaS, cubic, major phase) and periclase (MgO, cubic, minor phase) were detected on PEF sample #007.. Periclase was also detected in the SiMn TF. Elemental Mn was detected as Mn_3Si (cubic) in one of the PEF samples from Sauda, but in no other sample.

In general, Mn is mostly present as Mn_3O_4. Other phases dominating the sampels are β-quartz, K_2SO_4, and ZnO.

5.2 Elemental analyses

5.2.1 FFP

Elemental analysis shows that Mn is the most abundant element in the FeMn and SiMn FFP, at 27 ± 1.3 wt% and 25.2 ± 0.43 wt% respectively. Potassium was the next most abundant element in FeMn and SiMn FFP, at 17 ± 1.0 wt% and 4.47 ± 0.036 wt% respectively. The less abundant elements include Al, Ca, Fe, Mg, Na, Pb, Si, and Zn. Their contents are presented in Table 5.2. Detection and quantification limits for the analysis are presented in Table B.6 in Appendix B.

Table 5.2. Content in wt% of the 10 most abundant elements in the FFP samples. Standard deviations based on n=6 samples.

Element	FeMn		SiMn	
	Content [wt%]	SD [wt%]	Content [wt%]	SD [wt%]
Al	1,09	0,040	2,66	0,057
Ca	0,31	0,020	1,95	0,058
Fe	1,23	0,046	5,2	0,15
K	17	1,0	4,47	0,036
Mg	0,93	0,047	0,90	0,016
Mn	27	1,3	25,2	0,43
Na	0,80	0,028	0,50	0,011
Pb	0,837	0,0048	0,233	0,0078
Si	2,6	0,29	10,9	0,54
Zn	4,5	0,18	1,65	0,031

Table 5.3. Content in wt% of water-soluble elements in the FeMn and SiMn FFP samples. Standard deviations were based on n=3 samples.

Element	FeMn		SiMn	
	Content [wt%]	SD [wt%]	Content [wt%]	SD [wt%]
Ca	0,063	0.0015	0,088	0.0050
K	15,1	0.40	3,26	0,025
Mg	0,20	0.011	0,032	0.0010
Na	0,65	0.020	0,291	0.020
Mn	0,38	0.026	0,293	0.0090
S	6,43	0.050	1,31	0.026
Zn	0,214	0.0086	0,04	0.017

5.2.2 Water-extracts of FFP

In the water soluble part of the FeMnFFP, the two most abundant elements were K and S, comprising 15.1 ± 0.40 wt% and 6.43 ± 0.050 wt% of the powder respectively. Other minor elements were Na, Mn, Zn, Mg, and Ca, decreasing in that order from 0.65 ± 0.020 wt% to 0.063 ± 0.0015 wt% for Na and Ca respectively.

In the water soluble part of the SiMn FFP, K and S were also the most abundant elements, but in lower concentrations. Potassium comprised 3.26 ± 0.0025 wt% of the SiMn FFP, while S comprised 1.31 ± 0.026 wt% of the powder. Minor elements were Mn, Na, Ca, Zn, and Mg, decreasing in that order from 0.293 ± 0.0090 wt% to 0.032 ± 0.0010 wt%. The contents for the elements given above are given in Table 5.3. Detection and quantification limits for the analysis are presented in Table B.6 in the appendix.

Table 5.4. Content in wt% of the 10 most abundant elements in the FeMn and SiMn TF samples. Standard deviations were based on n=3 samples.

Element	FeMn		SiMn	
	Content [wt%]	SD [wt%]	Content [wt%]	SD [wt%]
Al	1.9	0.25	3.4	0.98
Ca	5.1	0.13	9	1.1
Fe	3.5	0.16	1.46	0.018
K	2.6	0.22	1.7	0.12
Mg	5.9	0.12	4.3	0.75
Mn	25	2.2	11.9	0.19
Na	0.50	0.035	0.42	0.066
S	0.7	0.21	1.02	0.219
Si	11.9	0.95	12.5	0.57
Zn	0.55	0.068	0.24	0.045

5.2.3 TF samples

Elemental analysis show that Mn is the most abundant element in the FeMn and SiMn TF samples, comprising 25 ± 2.2 wt% and 11.9 ± 0.19 wt% of the sample mass, respectively. Silicon was the next most abundant element in FeMn and SiMn TF samples, comprising 11.9 ± 0.95 wt% and 12.5 ± 0.57 wt% of the sample mass, respectively. The less abundant elements include Al, Ca, Fe, K, Mg, Na, S, and Zn. Their contents are given in Table 5.4. Detection and quantification limits for the elements are presented in Table B.6 in the appendix.

5.3 IC analyses

The contents of water-soluble SO_4^{2-}, Cl^- and F^- in the FFP were found to be 18.0 ± 0.48 wt%, 2.50 ± 0.069 wt%, and 0.125 ± 0.0034 wt%, respectively. In the SiMn FFP, the contents of the same anions were 3.1 ± 0.11 wt%, 1.14 ± 0.039 wt%, and 0.104 ± 0.0058 wt%, respectively. These findings are summarized in Table 5.5.

The calculated recoveries of the added spike were in the range of 82 % to 92 %, and are presented in Table 5.6. The contents presented in Table 5.5 were corrected for the spike recoveries. All QC concentrations were estimated to within ± 5 % of their theoretical value.

Table 5.5. Contents in wt% of SO_4^{2-}, Cl^-, and F^- in the FFP. Standard deviations were based on n=3 samples.

Anion	FeMn		SiMn	
	Content [wt%]	SD [wt%]	Content [wt%]	SD [wt%]
Cl^-	2.50	0.069	1.14	0.039
F^-	0.125	0.0034	0.104	0.0058
SO_4^{2-}	18.0	0.48	3.1	0.11

Table 5.6. The recovered spikes added to the samples for anion chromatographic analysis. Standard deviations in absolute units.

Anion	FeMn		SiMn	
	Recovery [mole%]	SD [mole%]	Recovery [mole%]	SD [mole%]
Cl^-	92	1.2	84	2.2
F^-	91	1.6	85.6	0.71
SO_4^{2-}	91	4.9	82	4.1

Table 5.7. Proportions in % of elements present in water-soluble compunds, rounded to one decimal, for FeMn and SiMn FFP The ratios are based on the contents given in Table 5.2 and Table 5.3. DL: Detection limit

Element	Solubility of elements [%]	
	FeMn	SiMn
Al	0.01	0.01
Ca	19.9	4.5
Fe	<DL*	<DL
K	90.1	73.1
Mg	21.6	3.5
Mn	1.4	1.2
Na	81.4	58.4
Si	<DL	<DL
Zn	4.8	2.2

*Detection limits for Si and Fe respectively were 4.7×10^{-5} wt% and 2.3×10^{-3} wt%.

5.4 Solubilty of elements

The proportions of soluble elements have been calculated based on the contents in Tables 5.2 and 5.3. These ratios are presented for Al, Ca, Fe, K, Mg, Mn, Na, Si, and Zn in Table 5.7. Note that such ratios can only be calculated where both the bulk content and water-soluble content have been measured for the respective elements. Lead was not included in the water-extract analysis, and S was not included in the total dust analysis, and solubility data are therefore not available for Pb and S.

5.5 pH measurements

The water-extracts from both FeMn and SiMn FFP samples were slightly alkaline, having a pH of 7.6 and 7.2, respectively.

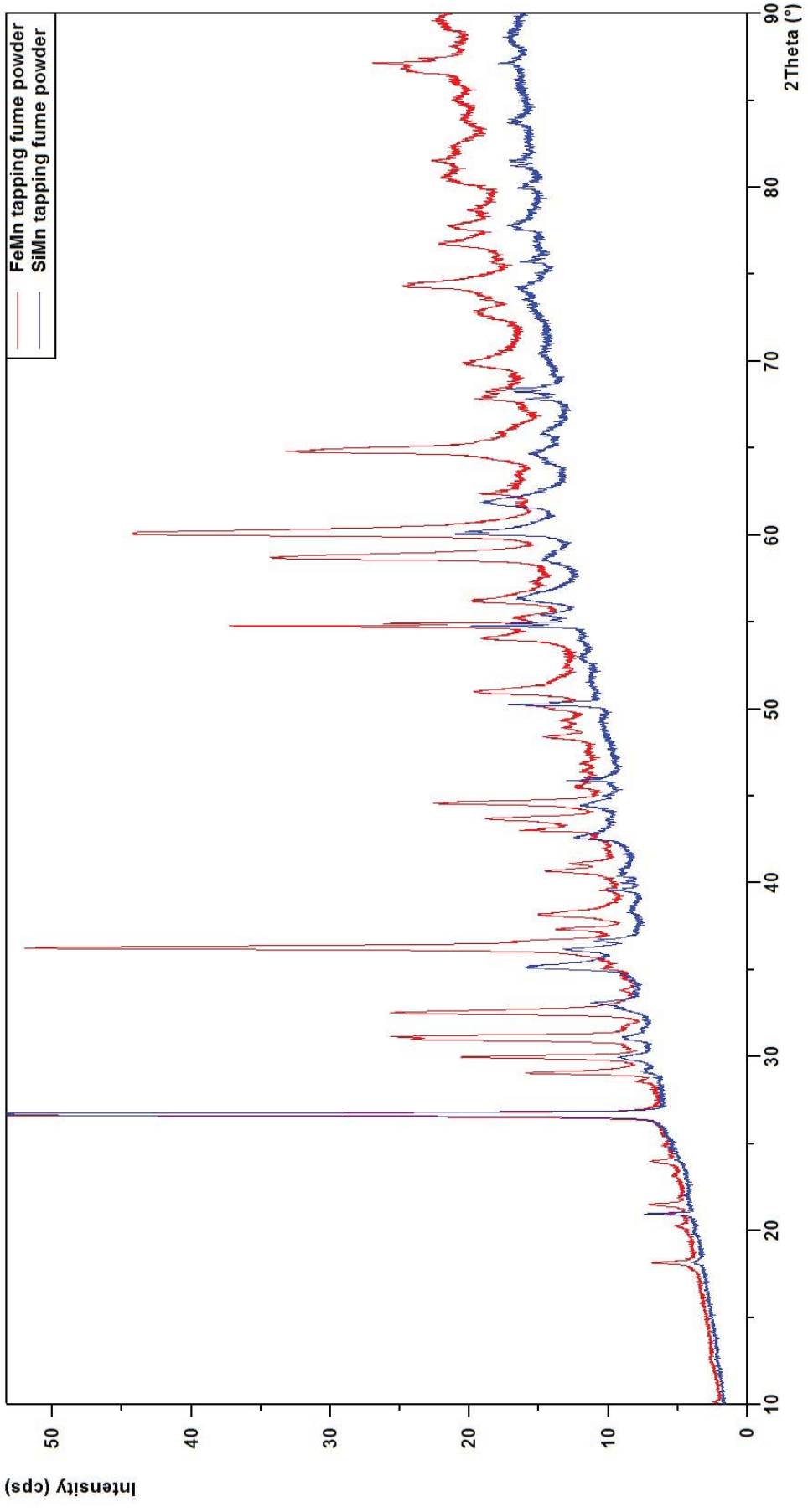

Figure 5.1. Diffractograms resulting from XRD analysis of FeMn and SiMn FFP. The large peaks at approximately $26°2\theta$ have been cut to better present the smaller peaks. The intensity of the cut peaks were about 150 cps and 70 cps for the FeMn and SiMn spectra, respectively.

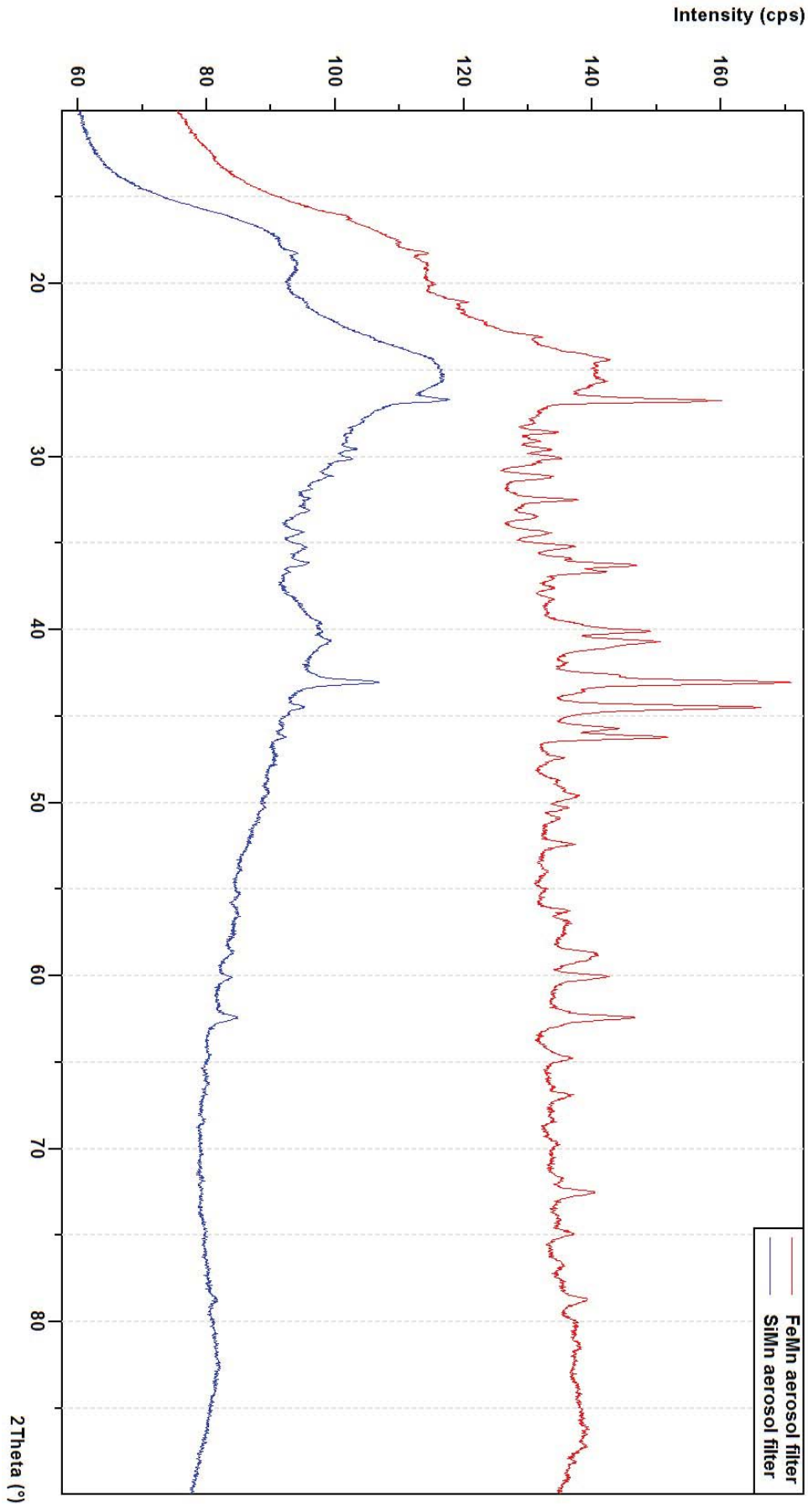

Figure 5.2. Diffractograms resulting from XRD analysis of FeMn and SiMn TF samples. A higher background is observed due to the stacking of filters.

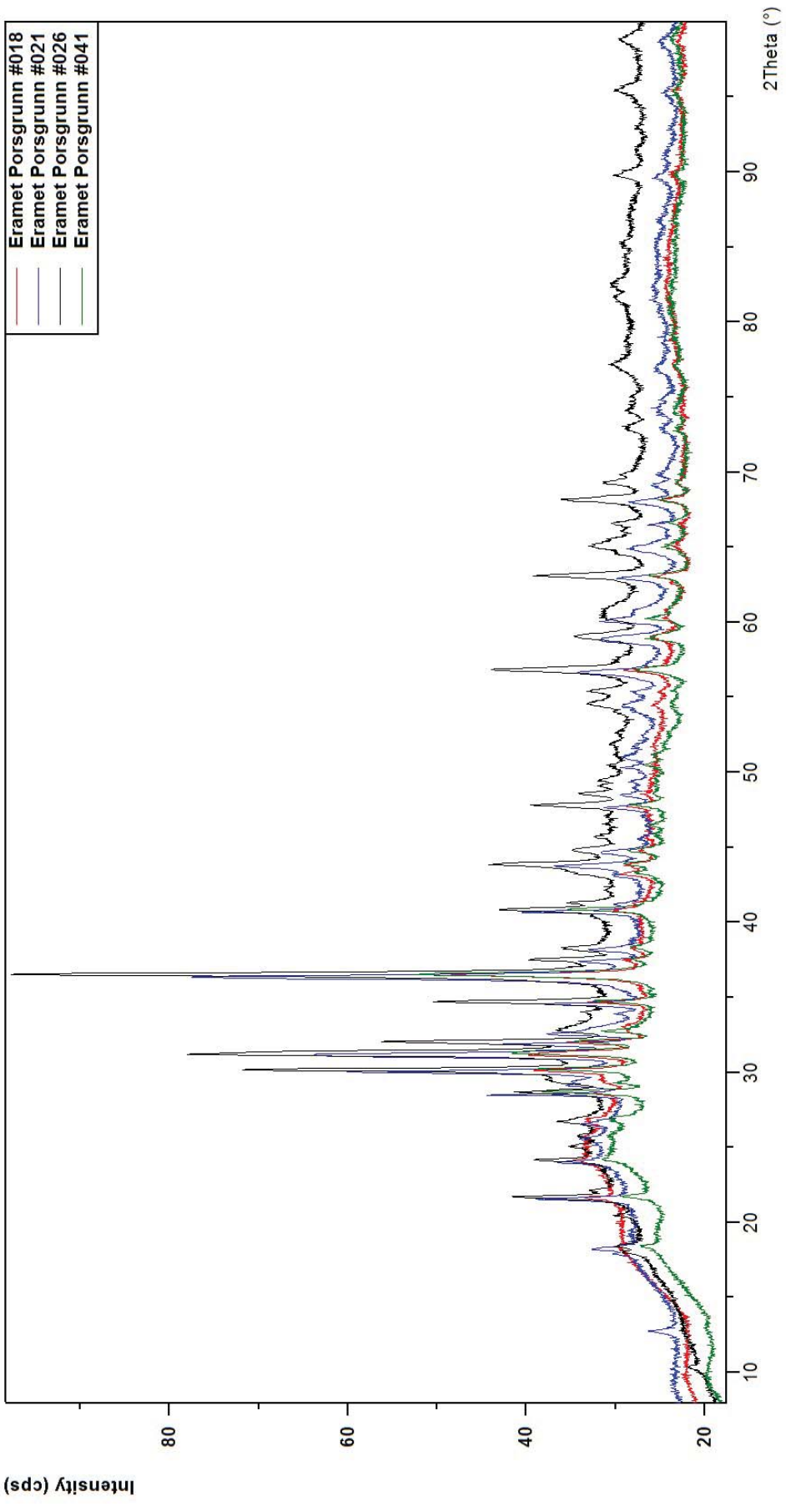

Figure 5.3. Diffractograms from analysis of four different PEF samples worn by FeMn and SiMn tappers at Eramet's plant in Porsgrunn. Sample #018 (red) was worn by a SiMn tapper, while the rest were worn by FeMn tappers.

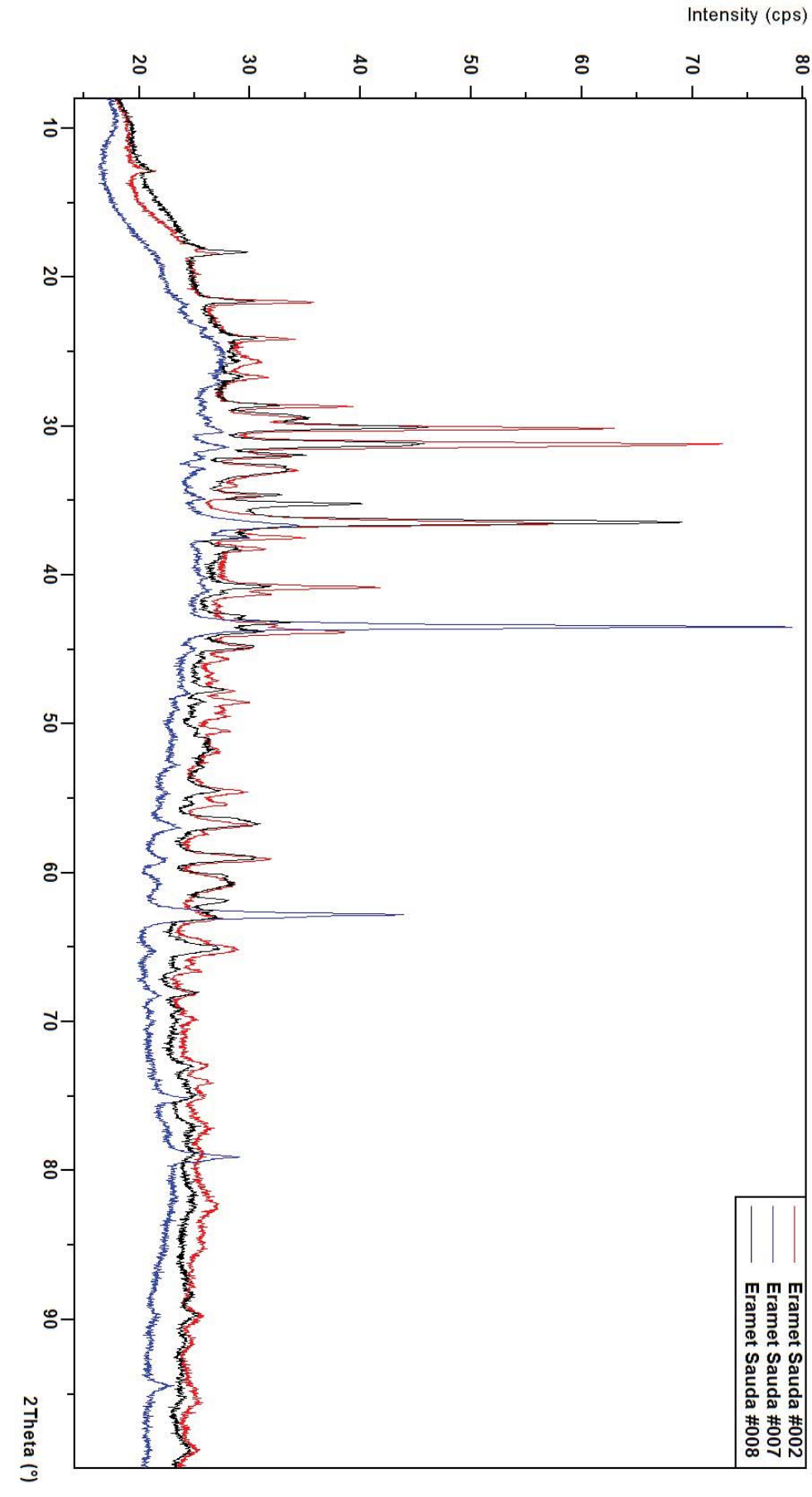

Figure 5.4. Diffractograms from analysis of three PEF samples worn by FeMn tappers at Eramet's plant in Sauda. Sample #007 (blue) exhibits different peaks than the other two samples.

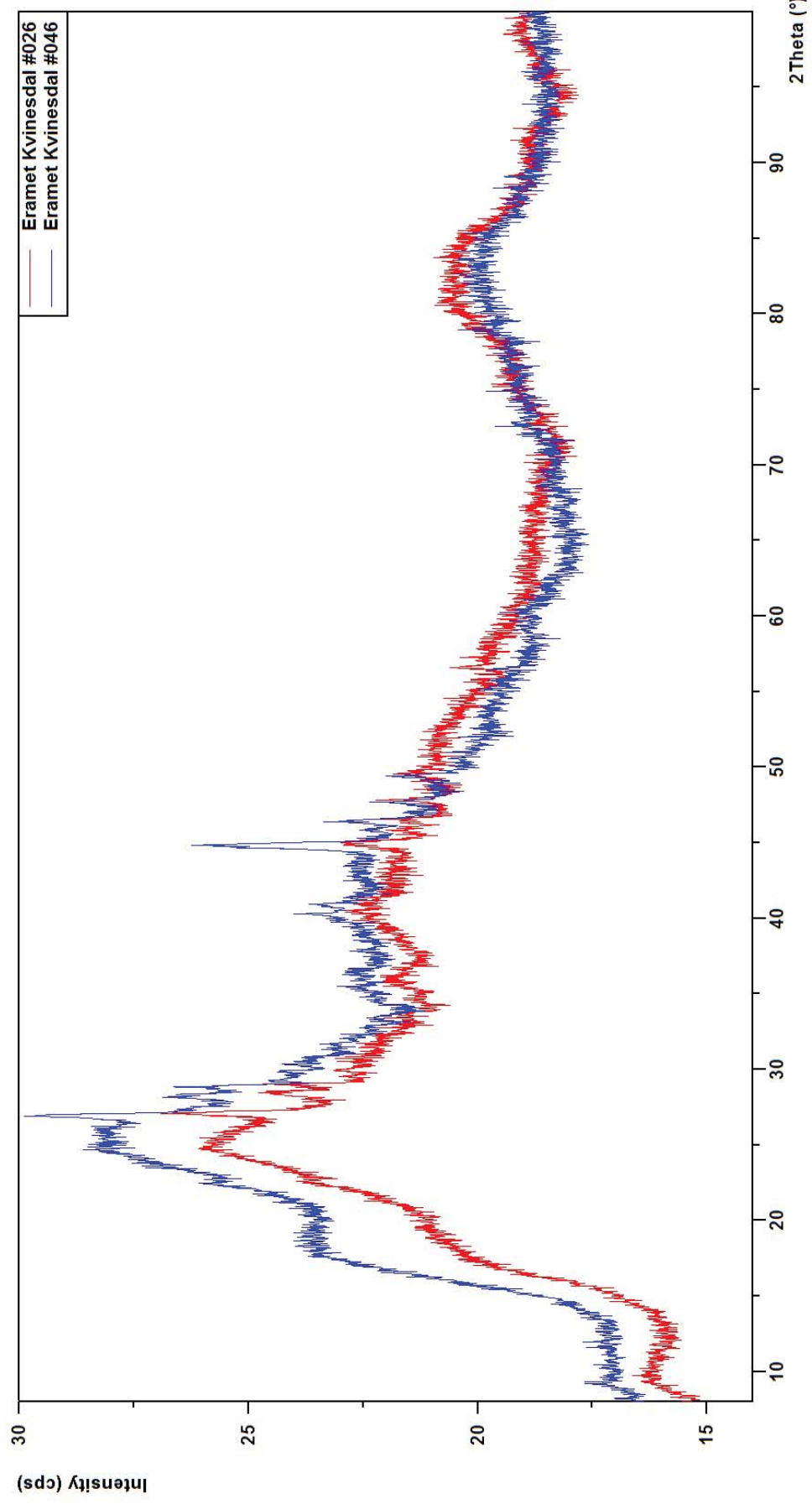

Figure 5.5. Diffractograms from analysis of two PEF samples worn by SiMn tappers at Eramet's plant in Kvinesdal. The data is noisy due to little sample material on the filters (approximately 0.5 mg), and no phases were deteected.

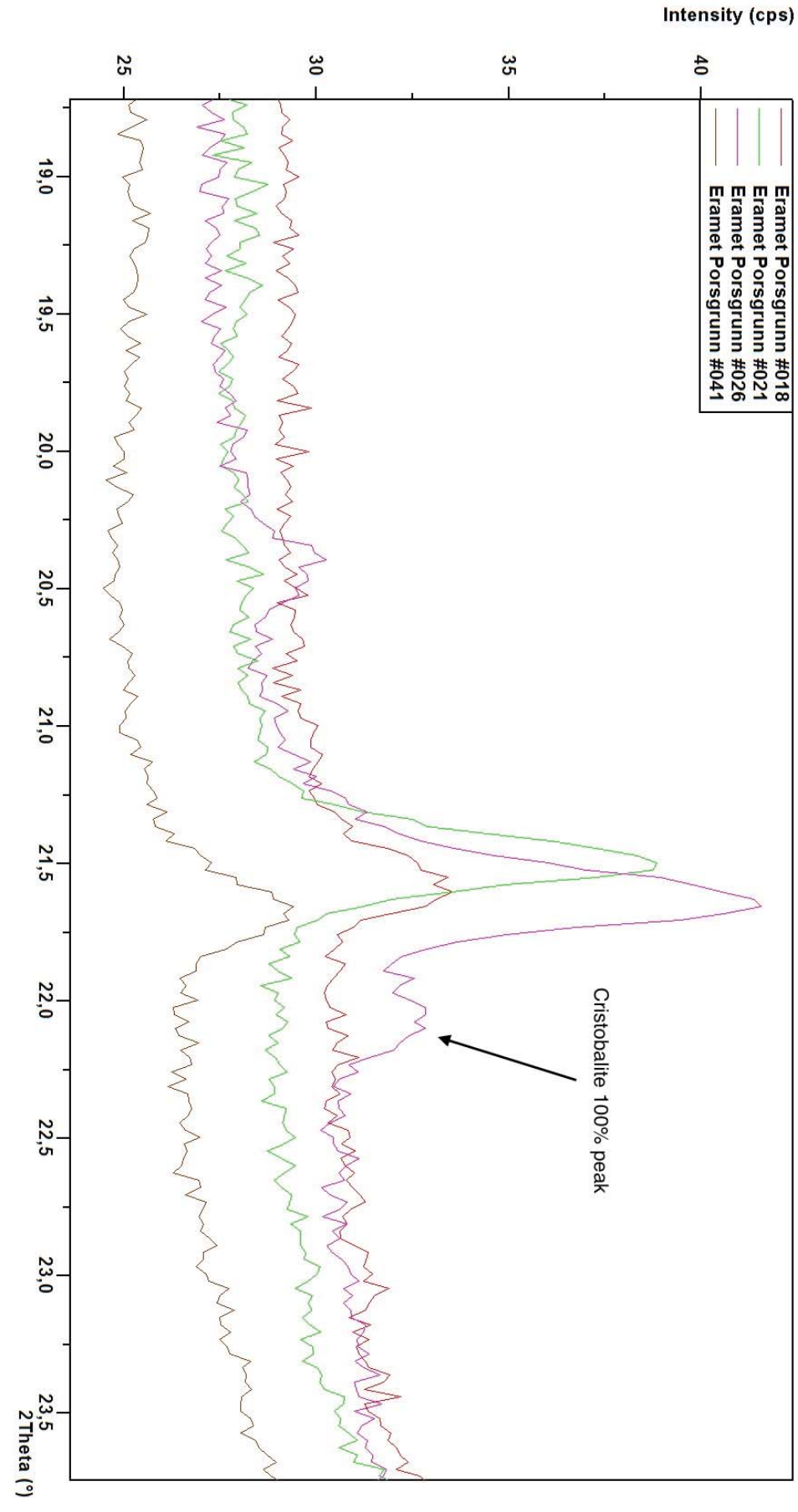

Figure 5.6. Comparison diffractograms obtained from XRD analysis of PEF samples from Porsgrunn. Cristobalite was only detected in sample #026.

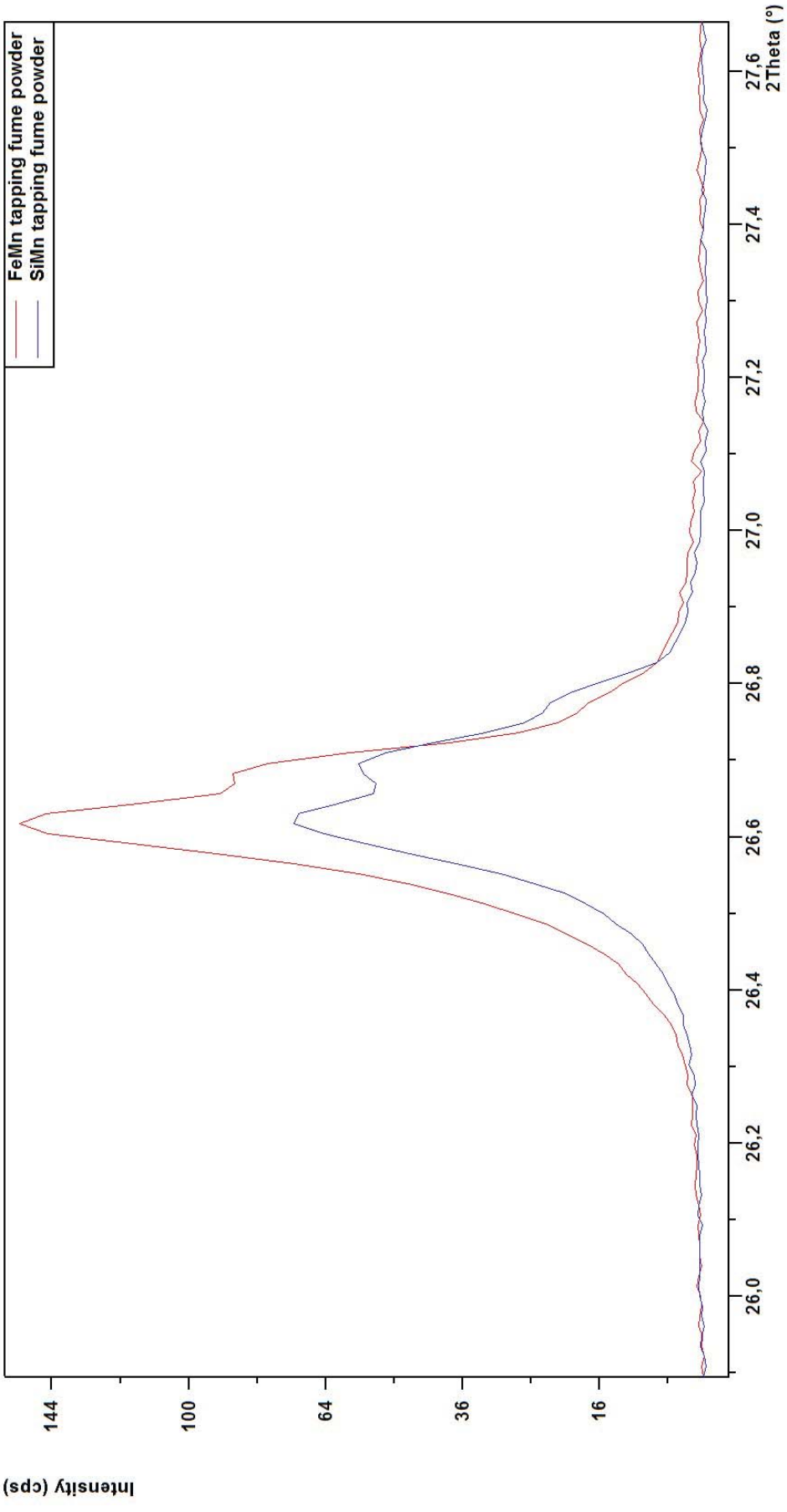

Figure 5.7. Zoomed-in view of the most intense β-quartz peak at around 26.6°2θ. The FeMn FFP more β-quartz than the SiMn FFP.

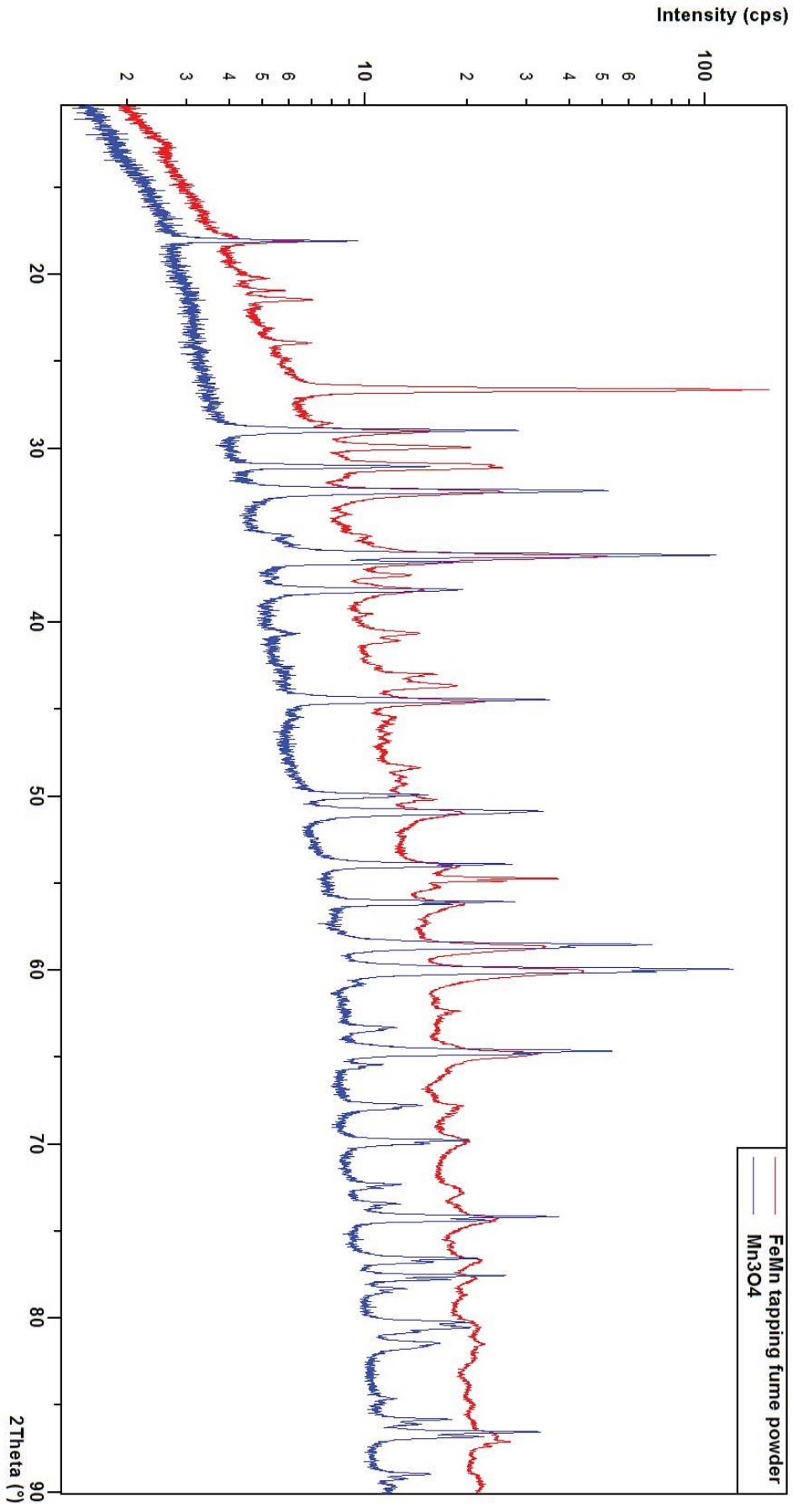

Figure 5.8. Comparison of hausmannite reference diffractogram and FeMn FFP. The two diffractograms match well. All of the largest peaks are found in XRD pattern of the FeMn FFP.

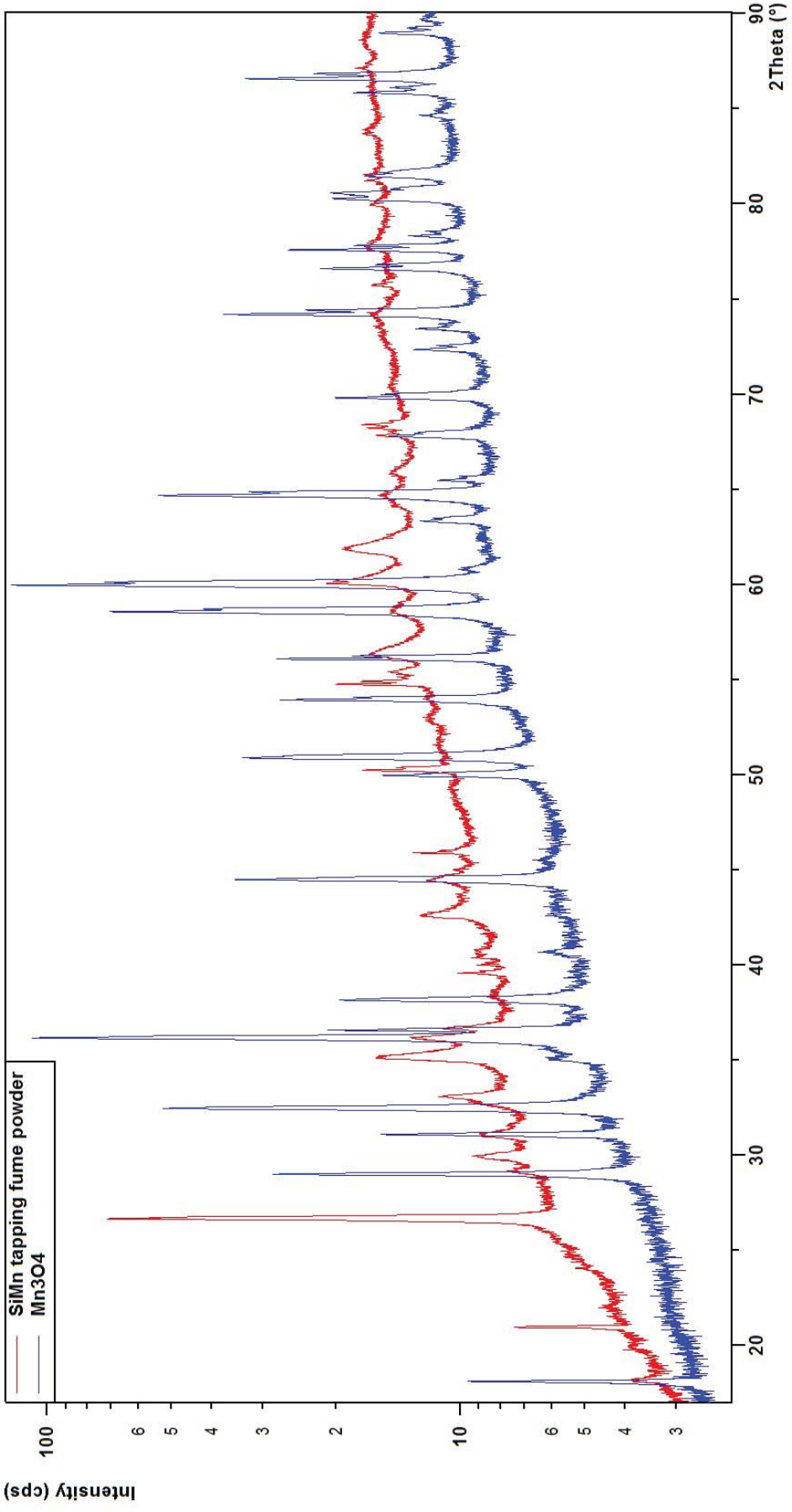

Figure 5.9. Comparison of hausmannite reference diffractogram and SiMn FFP diffractogram. The two diffractograms match well, although not as well for FeMn FFP. Ferric hausmannite was detected in the SiMn FFP, and the Fe in the crystal structure will change the peak profile slightly.

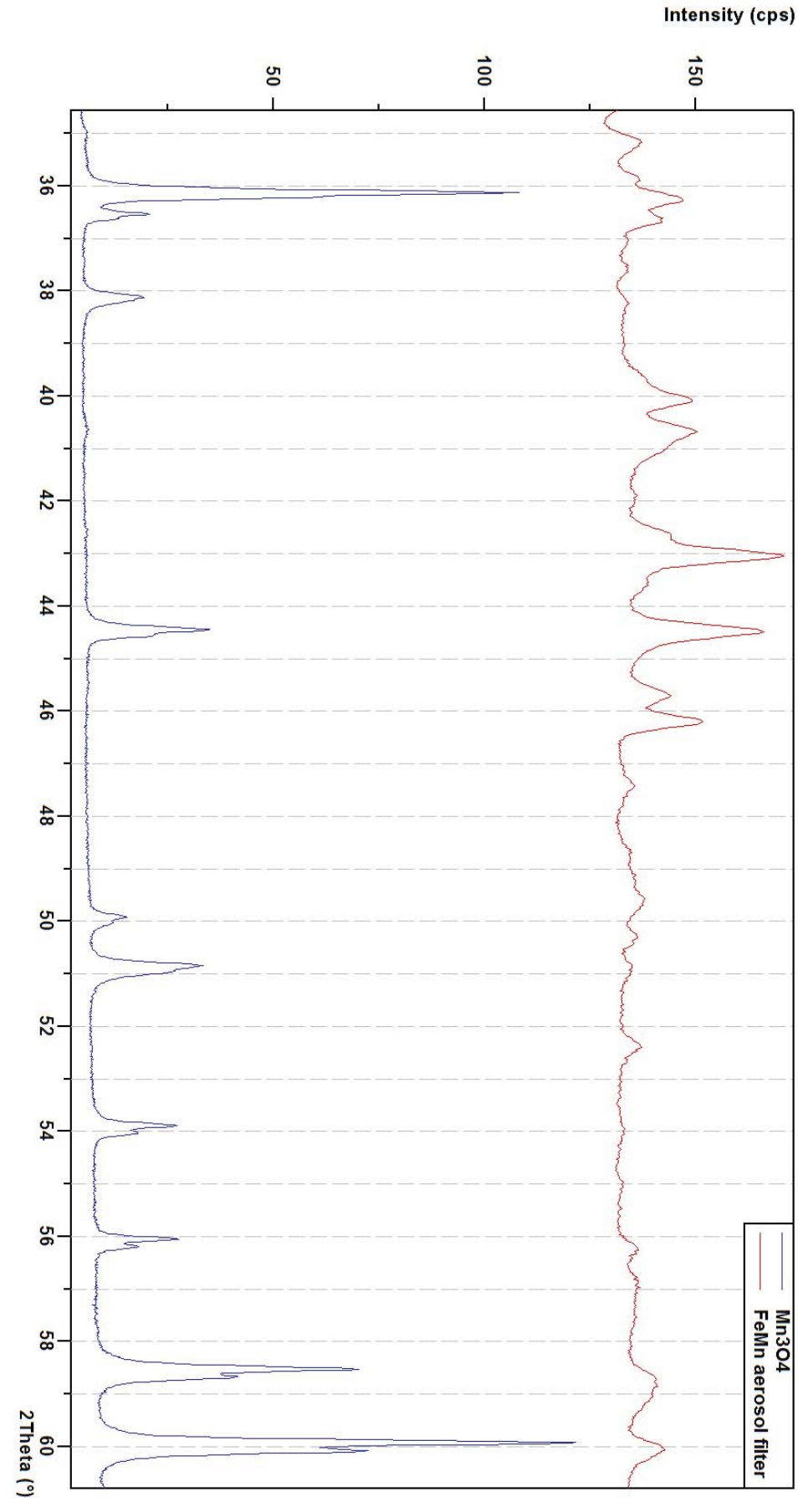

Figure 5.10. Comparison of hausmannite reference diffractogram and FeMn TF diffractogram. Because the irradiated sample mass is quite low and because of stacking effects, visual inspection is harder here than for the FFP samples. Hausmannite was detected by the software.

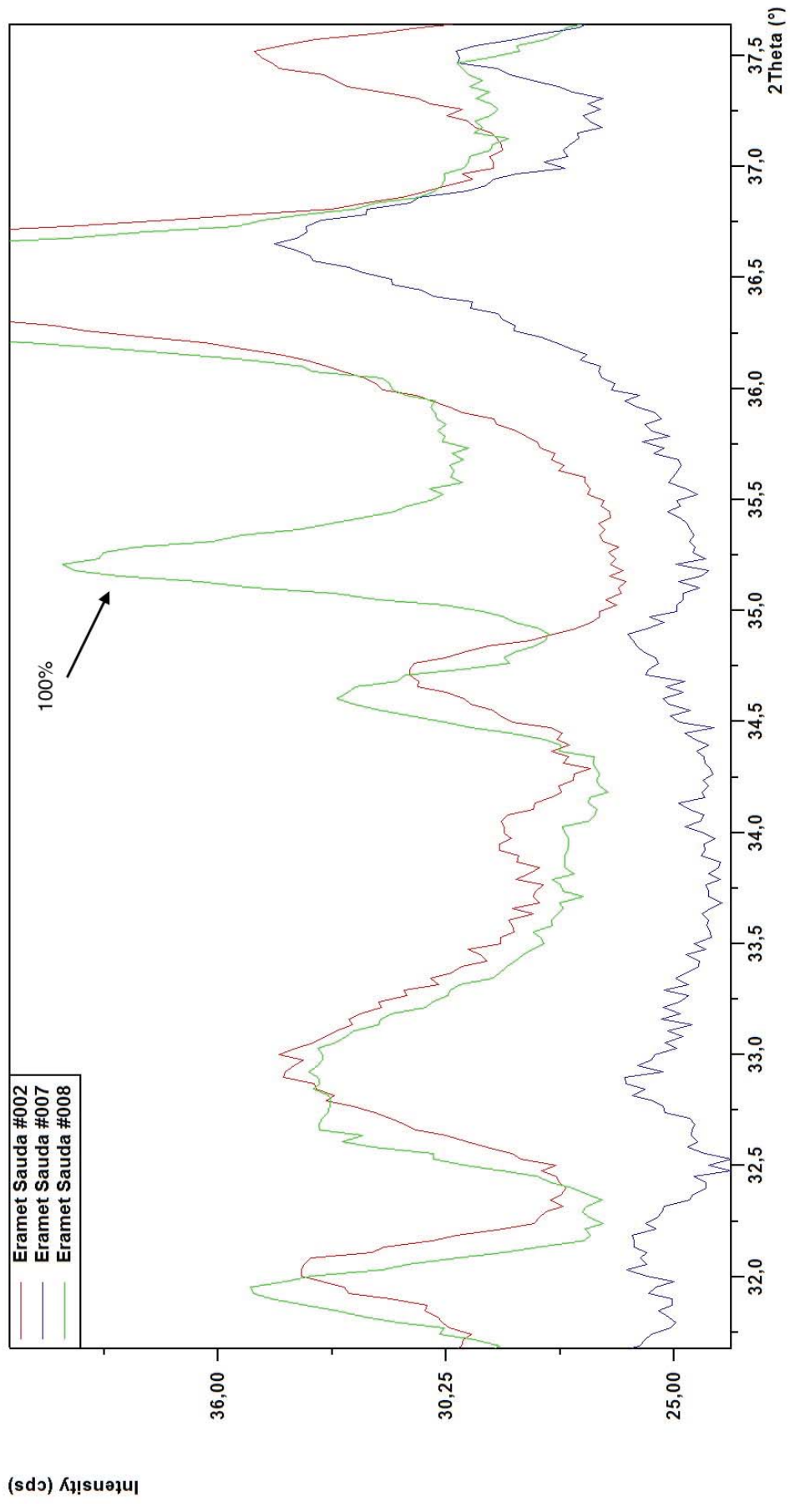

Figure 5.11. Comparison of PEF samples from Sauda. Magnesioferrite was only detected in one of the samples, which becomes clear when visually inspecting the diffractograms. The 100 % peak is clearly just present in sample #008.

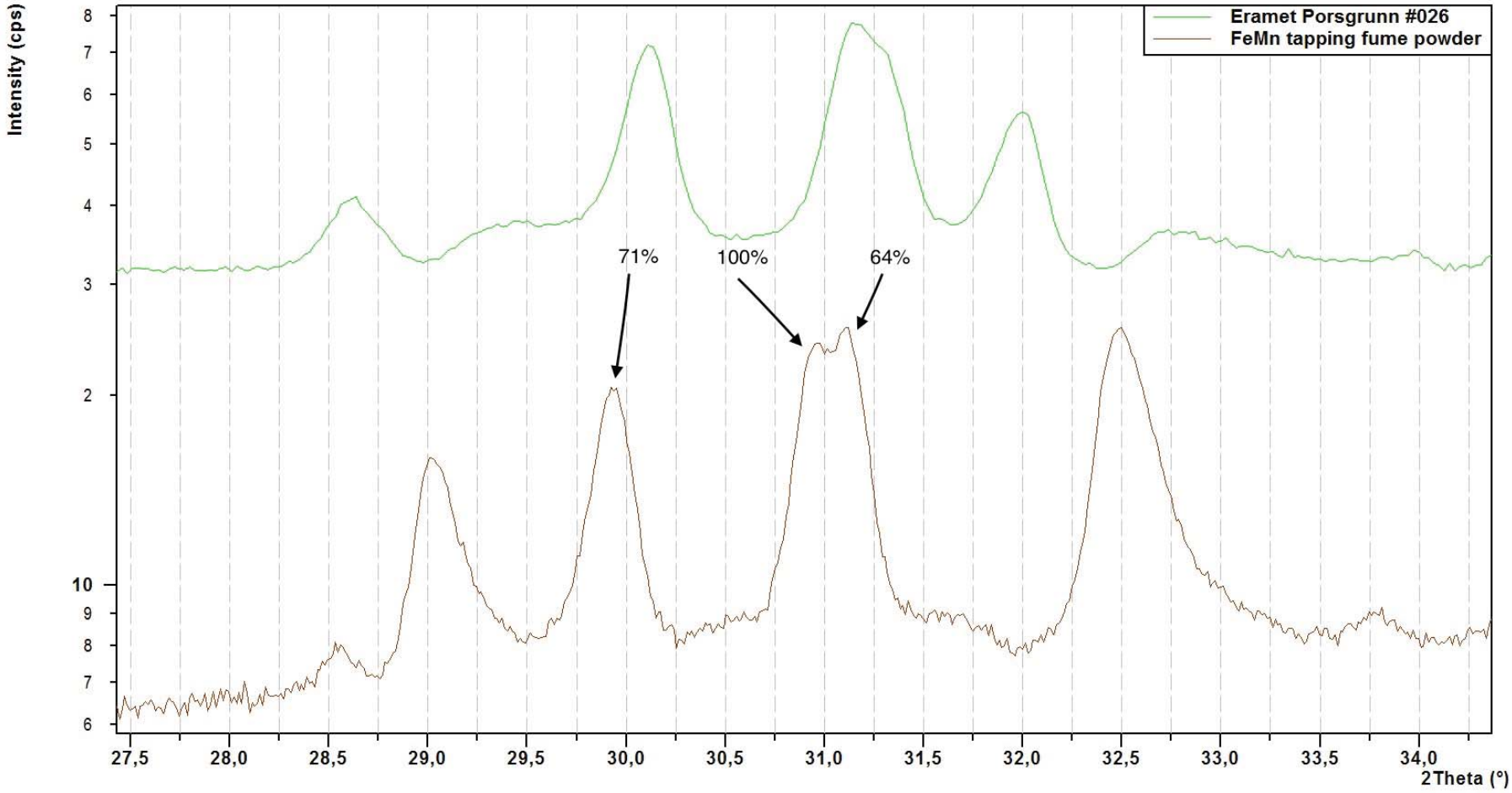

Figure 5.12. Comparison of FeMn FFP and PEF sample #026 from Porsgrunn. K_2SO_4 was detected in both samples, and the peaks are clearly visible in both diffractograms, although peak positions are slightly shifted. K_2SO_4 was detected in several other samples too, but to keep the figure clean only two samples were compared.

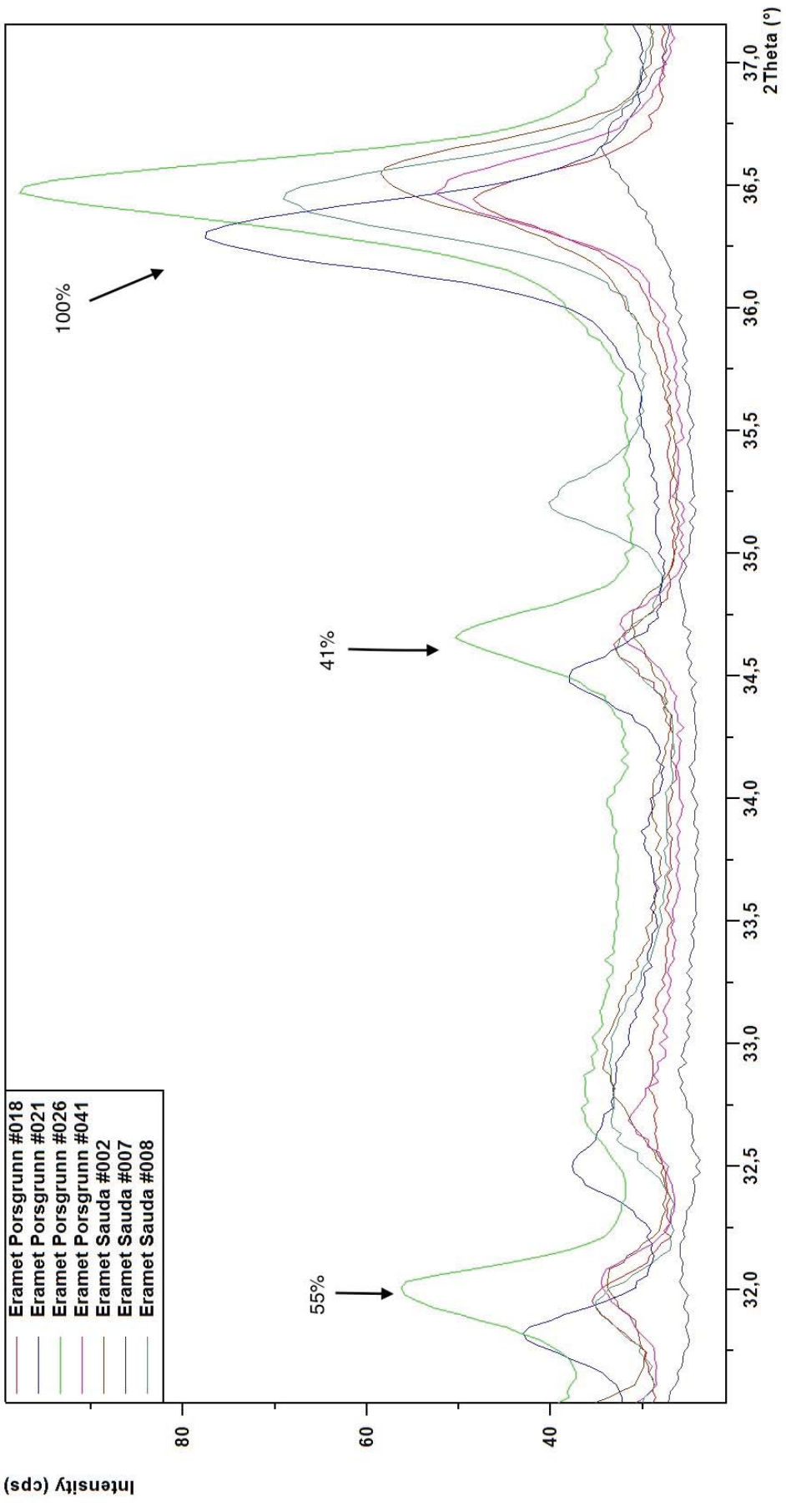

Figure 5.13. Comparison of a PEF sample from Porsgrunn and one from Sauda, zoomed in to show the three most intense periclase peaks. ZnO was detected in all samples, which share the three ZnO peaks. The peaks in sample #021 look to be slightly shifted to the left.

6 Discussion and conclusion

6.1 Discussion of results

The detected elements and phases agree well with the studies presented in Chapter 2. The cited studies report MnO as a major phase in the tapping fume, which was not detected in the present study. However, as mentioned in the literature review, individual particle diffraction analyses are not representative for the bulk sample. Further, some of Gjønnes et al. (2011)'s data indicate that Mn is present as *either* MnO or Mn_3O_4 in their samples; there is some ambiguity to their data. Gjønnes et al. analyzed sub-micron particles in the respirable sub-fraction, and it may be that sub-fraction is indeed dominated by MnO, while the bulk sample analyzed here is dominated by Mn_3O_4.

It may not be arbitrary where the air-sampler is placed during sample colleciton. The findings of Ravary et al. (2010) from an air-flow study in the FeMn tapping area at Eramet Porsgunn, show that most of the fumes released in the tapping runner are caught by the main ventilation system, but the fumes released when the melt has reached the crucible escape the ventilation system. Fumes originating in the crucible pollute the working area, and their movement and distribution are affected by air-flows. As stated in the literature review, few studies reported where the air samplings were carried out, relative to the furnace. Air-flow within the production hall may affect the composition as heavy compounds may deposit more quickly and not travel as far. Studies of how placement of air-sampler affects composition of collected aerosol may provide useful information concerning sampling strategy.

The furnace fume powder collected in the emission purification unit is different from the aerosol collected in the tapping area. Furnace fumes are generated inside the furnace, while the workplace aerosols are likely generated from the melt in the crucible and carried to the multiport sampler. Due to inherent difference in sample matrices analyzed, the observed variation in composition (e.g. K content from 2.6 wt% to 50 wt%), should therefore be expected (Thomassen 2015).

Although elemental analysis revealed that the SiMn FFP contained more Si than the FeMn FFP, XRD analysis showed that the FeMn FFP contained more crystalline quartz than the SiMn FFP (see Figure 5.7). Further, about 5x more Si was found in the FeMn TF sample than in the FFP, but a weak quartz signal was detected with XRD in the FeMn TF sample. This indicate that the quartz component of the furnace fume originates from some other place than the raw materials. Schacht (2004, Chapter 2, Section II, 1st paragraph) states that silicates are common natural impurities in commercial refractories used in furnaces. It may be possible that silica evaporates from the refractory linings, and undergo chemical reactions and crystallization in the fume.

It is alarming that crystalline quartz is detected in such large quantities. Quartz is a crystalline polymorph of silica (SiO_2). Amorphous silica may be formed by oxidation

of SiO with O_2, and the high temperatures in the furnaces may increase crystallization rates of amorphous silica, ultimately ending up as β-quartz (which was most commonly detected in XRD analysis). β-quartz is only metastable at room temperature and should slowly transform to α-quartz, the exposure to which is strictly regulated due to α-quartz's health effects. Although no α-quartz was detected in this study, the high occurance of β-quartz may be an indication that workers are also exposed to α-quartz. Future studies should focus on locating the source of crystallized Si, and whether workers are in danger of inhaling α-quartz.

It can be seen from Table 5.7 that the FeMn FFP is in general more water-soluble than the SiMn FFP. The slightly higher pH in FeMn water-extract also indicates this. Gjønnes et al. (2011) suggest that workers in FeMn production may be subject to a higher risk of adverse health effects than workers in SiMn production, due to more soluble species of Mn. Solubility and pH measurements conducted in this thesis suggest the same thing: FeMn production workers may be exposed to more bioaccessible species of Mn (and other elements too). However, the present XRD analysis showed that the same Mn oxide was detected in FeMn and SiMn samples, indicating that less soluble forms of Mn (e.g. SiMn alloy) are present in amounts too low to be detected with XRD in the current samples. That said, the difference in solubility of Mn presented here is very small, and may not be significant. The furnace fumes may also be of limited relevance to workers as it is generated inside the furnaces. Therefore, studying water-solubility of the workplace aerosol instead of the furnace fume powder may be more relevant to the workers.

6.2 Quality of analyses

6.2.1 XRD

Phase identification was limited by the low mass in TF and PEF samples. Although the major phases were detected with confidence, a larger uncertainty should be associated with the minor phases. Phase identification is a semi-subjective and experience-based process, and another XRD operator might have decided on a slightly different composition. However, diffractogram quality was good for FFP samples samples due to the large amount of mass on the filter.

Due to the high number of peaks in the diffractograms, which is especially evident in the FFP samples, a lot of peak overlapping is likely to take place. It should therefore be expected that some minor phases were wrongfully not detected. To some extent such phases may be detected based on calculations of peak residuals, but it is difficult to check whether accepting such minor phases is valid. Certain detected phases, such as α-cristobalite and magnesioferrite, were in some samples detected based on just one peak. Such identifications are associated with larger uncertainties than if several peaks are present.

The sample mass on the TF filters and the PEF should have been higher. This problem is most visible in the diffractograms of TF samples and PEF from Kvinesdal (Figures 5.2 and 5.5). The multiport sampler system used to collect workplace aerosol samples in Porsgrunn yielded only around 0.4 mg to 1 mg of sample material. The duration of sample collection could be increased from 24 h to 72 h, or even longer, which would increase the amount sample material. Of course, the low amount of sample material this is partly because of the low air concentration at the place where of sampling. In addition, if the orifices through which the air was pumped were made larger, a higher air-flow rate could have obtained, and more sample material could be collected.

Low amounts of sample material was deposited on the PEF as well, especially on those from Kvinesdal. This is partly due to that the cyclones collected the respirable aerosol sub-fraction, and not bulk samples. However, more sample material could be obtained by using sampling cyclones able to collect a larger amount of sample material.

To counter the problem of low sample mass on the filters they had to be stacked, which drastically increased the background levels from the filters. Avoiding the stacking would therefore greatly improve the quality of the diffractograms.

The National Institute for Occupational Safety and Health (2003, Method 7500) describes a method for separating the workplace aerosol sample material from the PVC filter by dissolving the filter in tetrahydrofuran (THF), and redepositing the sample material on silver membrane filters. The method is developed for quantifying small amounts of SiO_2 polymorphs using XRD, but it could perhaps be modified to increase sensitivity of other crystalline compopunds in workplace aerosols as well, such as Mn oxides. Further, several filters could be dissolved together and redeposited on another PVC filter to increase the sample material. Such a method could perhaps eliminate the need for stacking filters to obtain useable signals. The suitedness of such a method should be investigated further, as it may dramatically increase the quality of XRD analyses of low-mass samples. Although THF may affect the crystalline phases, the solvent has been previously used in contact with furnace powder prior to XRD analysis, and no undesirable interactions were reported (Shen et al. 2005).

Investing in a graphite monochromator, and placing it in the diffracted path, would also reduce background signals such as fluorescence. In addition, the Kα_2 and Kβ components would be completely eliminated, while maintaining Kα_1 intensity. Peak-splitting would therefore not be an issue, which would increase peak resolution.

Further, the crystallite size of the sample material limits the resolution obtainable in XRD analyses. Crystallite size affects peak width, and hence resolution, as described by the Scherrer equation published in 1918:

$$B = \frac{K\lambda}{L\cos\theta} \tag{6.1}$$

where B is the peak width and L is the crystallite size. This equation shows that the peak width is inversely proportional to the crystallite size. The particle sizes in furnace and

tapping fumes are inherently small, which may limit the resolution of certain phases. In most diffractograms presented here, the K$\alpha_{1,2}$ doublet is not visible due to peak broadening.

6.2.2 IC

The IC analysis of anions is considered accurate. Although the peaks were not baseline-separated, the separation was good enough for easy and straightforward peak integration (see Figure 4.6), and estimated contents were corrected for spike recovery. QC samples should ideally be independent of the calibration standards.

Concerning the extraction of water-soluble anions, the PO_4^{3-} IS was added after the actual extraction. Ideally the IS should be added before the extraction, compensating for any loss of analyte due to adsorption to the container, complex-binding, precipitation, etc. However, the IS may behave different from the analytes when going thorugh the powder. Therefore the IS was added after extraction.

The spike was also added after the extraction, but should ideally be added (along with the IS) before extraction started. Adding spike before extraction would give a more realistic recovery of the spike, as some spike may bond to the powder, and thereby not be available for dissolvation with water. A second extraction using the same powder could show whether more water-soluble anions were left in the powder. If this was the case, the anion concentrations presented here are underestimated.

6.2.3 ICP-OES

The method used for elemental analyses (both instrument method and acid digestion) is routinely used at NIOH for the same sample matrix, and has been previously validated. However, analysis of independent QC samples would improve the analysis. All elements were above their respective quantification limits, except for S which was in-between the QL and DL. This is not surprising, as S is not part of the routinely analyzed elements with the described method. All measured emission lines of S are below 190 nm, a region in which oxygen molecules in air absorb much of the emission (Boss et al. 2004). Therefore, when measuring UV emission lines, the system should to be purged with a gas that absorbs the emitted radiation to a much smaller extent, for example N_2 or Ar gas. In the present study, the system was filled with air at atmospheric pressure.

6.3 Concluding remarks

Phase characterization has been carried out for three different fume samples from production of FeMn and SiMn. The crystalline phases were shown to be predominantly Mn_3O_4, K_2SO_4, ZnO, and β-quartz. The high occurance of crystalline SiO_2 is surprising, and may be connected to the refractory linings on the inside of the electric furnaces.

The results from this thesis agree with previous studies in that workers in FeMn and SiMn production are exposed to a host of different compounds.

The quality of the XRD analyses were limited by the amount of sample material on aerosol filters and personal exposure filters. Future experiments should employ sampling systems capable of collecting more than just 0.5 to 1 mg of sample material. To obtain reasonable signal-to-noise ratios, closer to 9 mg sample may be needed. Modification of NIOSH Method 7500 should be investigated, as such a modified procedure may dramatically increase XRD sensitivity. Further, the possible exposure to α-quartz should be investigated further. Alternatively, the use of monochromators may improve spectral purity of the X-rays and reduce background signals such as sample fluorescence.

7

References

Antonini, J.M., K. Sriram, S. A. Benkovic, J.R. Roberts, S. Stone, B.T. Chen, D. Schwegler-Berry, A.M. Jefferson, B. K. Billig, C.M. Felton, M.A. Hammer, F. Ma, D.G. Frazer, J.P. O'Callaghan, and D.B. Miller (2009). "Mild steel welding fume causes manganese accumulation and subtle neuroinflammatory changes but not overt neuronal damage in discrete brain regions of rats after short-term inhalation exposure." In: *NeuroToxicology* 30 (6), pp. 915–925.

Berlinger, B. (2015). *Personal communication*.

Boss, C. B. and K. J. Fredeen (2004). *Concepts, Instrumentation and Techniques in Inductively Coupled Plasma Optical Emission Spectrometry*. Copyright PerkinElmer. USA.

Delgado, G. El, A. J. Mora, C. Pineda, R. Ávila-Godoy, and S. Parades-Duagarte (2015). "X-ray powder diffraction data and rietveld refinement of the ternary semiconductor chalcogenides $AgInSe_2$ and $AgInTe_2$." In: *Latin-American Journal of Metallurgy and Materials* 35 (1), pp. 110–117.

Dionex Corporation (2012). *Product Manual for Dionex IonPac™AS18 and AG18 Columns*. Document no.: 031878-08. ©2012 Dionex Corporation.

Elkin, K. R. (2014). "Development of novel ion chromatography techniques and their applicability in portable automated instrumentation for in-situ quantitative analysis." PhD thesis. Norwegian University of Life Sciences.

Ellingsen, D. G., R. Bast-Petterson, S. Hetland, and Y. Thomassen (2000). *Helseundersøkelse av manganeksponerte i smelteverk — en tverrsnittundersøkelse*. STAMI-rapport Årg. 1, nr. 6. ISSN: 1502-0932.

Ellingsen, D. G., R. Konstantinov, R. Bast-Pettersen, L. Merkurjeva, M. Chashchin, Y. Thomassen, and V. Chashchin (2008). "A neurobehavioral study of current and former welders exposed to manganese." In: *Neurotoxicology* 29 (1), pp. 48–59.

Ellingsen, D. G., Z. Kusraeva, R. Bast-Pettersen, E. Zibarev, M. Chashchin, Y. Thomassen, and V. Chashchin (2013). "The interaction between manganese exposure and alcohol on neurobehavioral outcomes in welders." In: *Neurotoxicology and Teratology* 41, pp. 8–15.

Eramet Norway. *The Production Process*. URL: http://eramet.no/en/the-production-process/ (visited on 09/05/2015).

Ermrich, M. and D. Opper (2011). *XRD for the analyst: Getting acquainted with the principles*. Booklet published by PANalytical.

Ewald, P. P. (1962). *Fifty years of X-ray diffraction*. Dedicated to the International Union of Crystallography on the occasion of the commemoration meeting in Munich July 1962. Utrecht, The Netherlands: N.V. A. Oosthoek's uitgeversmaatschappij.

FIZ Karlsruhe (2014). *ICSD — Inorganic Crystal Structure Database*. URL: http://www.fiz-karlsruhe.de/icsd.html (visited on 11/04/2015).

Fransen, M. J. (2004). "1- and 2-dimensional detection systems and the problem of sample fluorescence in X-ray diffractometry." In: *Advances in X-ray Analysis* 47, pp. 224–231.

Gjønnes, K., A. Skogstad, S. Hetland, D- G. Ellingsen, Y. Thomassen, and S. Weinbruch (2011). "Characterisation of workplace aerosols in the manganese alloy production indtustry by electron microscope." In: *Analytical and Bioanalytical Chemistry* 399 (3), pp. 1011–1020.

Gunst, S., S. Weinbruch, M. Wentzel, H. M. Ortner, A. Skogstad, S. Hetland, and Y. Thomassen (2000). "Chemical composition of individual aerosol particles in workplace air during production of manganese alloys." In: *Journal of Environmental Monitoring* 2 (1), pp. 65–71.

Health Alicious Ness. *Top 10 Foods Highest in Manganese*. URL: http://www.healthaliciousness.com/articles/foods-high-in-manganese.php (visited on 08/06/2014).

Hou, X. and B. T. Jones (2000). *Inductively coupled plasma/Optical emission spectrometry*. Ed. by R. A. Meyers. In: Encyclopedia of Analytical Chemistry. Copyright John Wiley & Sons Ltd, Chichester.

ISO/IEC (2012). *ISO 15202:2012(E) Workplace air — Determination of metals and metalloids in airborne particulate matter by inductively coupled plasma atomic emission spectrometry — Part 2: Sample preparation*. 2nd ed. Geneva, Switzerland: ISO/IEC.

Kelleher, P., K. Pacheco, and L. S. Newman (2000). "Inorganic dust pneumonias: the metal-related parenchymal disorders." In: *Environmental Health Perspectives* 108 (4), pp. 685–696.

Kero, I., M. K. Næss, and G. Tranell (2015). "Particle size distributions of particulate emissions from the ferroalloy industry evaluated by electrical low pressure impactor (ELPI)." In: *Journal of Occupational Environmental Hygiene* 12 (1), pp. 37–44.

Key To Metals (2002). *Austenitic Manganese Steels*. URL: http://www.keytometals.com/page.aspx?ID=CheckArticle%5C&site=kts%5C&NM=69 (visited on 08/06/2014).

Key to Metals. *Aluminum Alloys — Effects of Alloying Elements*. URL: http://www.keytometals.com/Article55.htm (visited on 08/06/2014).

Loranger, S. and J. Zayed (1995). "Environmental and occupational exposure to manganese: a multimedia assessment." In: *International Archives of Occupational and Environmental Health* 67 (2), pp. 101–110.

Lucchini, R. G., C. J. Martin, and B. C. Doney (2009). "From manganism to manganese-induced parkinsonism: A conceptual model based on the evolution of exposure." In: *Neuromolecular Medicine* 11 (4), pp. 311–321.

Michalke, B., S. Halbech, and V. Nischwitz (2007). "Speciation and toxicological relevance of manganese in humans." In: *Journal of Environmental Monitoring* 9 (7), pp. 650–656.

Myers, J. E., M. L. Thompson, S. Ramushu, T. Young, M. F. Jeebhay, L. London, E. Esswein, K. Renton, A. Spies, A. Boulle, I. Naik, A. Iregren, and D. J. Rees (2003). "The Nervous System Effects of Occupational Exposure on Woerkers in a South African Manganese Smelter." In: *Neurotoxicology* 24 (6), pp. 885–894.

Oberdörster, G. (2001). "Pulmonary effects of inhaled ultrafine particles." In: *International Archives of Occupational and Environmental Health* 74 (1), pp. 1–8.

Pecharsky, V. K. and P. Y. Zavalij (2009). *Fundamentals of Powder Diffraction and Structural Characterization of Materials*. 2nd ed. New York, USA: Springer.

Ravary, B. and S. Grådahl (2010). "Improving environment in the tapping area of a ferromanganese furnace." In: *Proceedings of the Twelfth International Ferroalloys Congress: sustainable future*. Ed. by Asmo Vartiainen. Helsinki, finland: Outotec Oyj, pp. 99–107.

Roels, H.A., P. Ghyselen, J.P. Buchet, E. Ceulemans, and R.R. Lauwerys (1992). "Assessment of the permissible exposure level to manganese in workers exposed to manganese dioxide dust." In: *British Journal of Industrial Medicine* 49 (1), pp. 25–34.

Roels, H.A., R. Lauwerys, J.P. Buchet, P. Genet, M.J. Sarhan, I. Hanotiau, M. de Fays, A. Bernard, and D. Stanescu (1987). "Epidemiological survey among workers exposed to manganese: effects on lung, central nervous system, and some biological indices." In: *American Journal of Industrial Medicine* 11 (3), pp. 307–327.

Schacht, C.A., ed. (2004). *Refractories Handbook*. 1st ed. ISBN-13: 9780824756543. New York, USA: CRC Press.

Shen, R., G. Zhang, M. Dell'Amico, P. Brown, and O. Ostrovski (2005). "Characterisation of manganese furnace dust and zinc balance in production of manganese alloys." In: *The Iron and Steel Institute of Japan* 45 (9), pp. 1248–1254.

Skoog, D. A., F. J. Holler, and S. R. Crouch (2007). *Principles of Instrumental Analysis*. Ed. by S. Kiselica. 6th ed. ISBN-13: 9780495012016. Belmont, CA, USA: David Harris.

The National Institute for Occupational Safety and Health (1978). *Occupational Health Guideline for Manganese*. URL: http://www.cdc.gov/niosh/docs/81-123/pdfs/0379.pdf (visited on 04/27/2014).

— (2003). *NIOSH Manual of Analytical Methods*. Ed. by K. Ashley and P. F. O'Connor. Cincinnati, Ohio: NIOSH.

Thomas, R. (2013). *Practical Guide to ICP-MS: A Tutorial for Beginners*. 3rd ed. Practical Spectroscopy. Boca Raton, Florida: CRC Press.

Thomassen, Y. (2015). *Personal communication*.

Thomassen, Y., D. G. Ellingsen, S. Hetland, and G. Sand (2001). "Chemical speciation and sequential extraction of Mn in workroom aerosols: analytical methodology and results from a field study in Mn alloy plants." In: *Journal of Environmental Monitoring* 3 (6), pp. 555–559.

A

Equipment and chemicals

A.1 Equipment

Table A.1. Manufacturer and model of instruments and equipment used in the thesis work

Equipment/model	Manufacturer and model
Analytical weight	Sartorius MC210P
Analytical weight	Sartorius MC 5
Teflon sample containers for microwave-assisted digestion	Milestone
X'Pert^3 Powder Diffractometer	PANalytical
Aerosol filter cassette, 25 mm Type A (Art. no.: M000025A0)	Millipore
PVC membrane filter, 25 mm ø, 5.0 µm pore size	Millipore
W-380 Sonicator, Ultrasonic processor	Heat Systems Ultrasonics, Inc.
Ω350 pH meter	Beckman
mls 1200 Digestion Module	Milestone
EM-45/A Exhaust Module	Milestone
Teflon autoclave	Milestone
50 mL tube	Sarstedt
15 mL tube	Sarstedt
ICS-2100 Ion Chromatography System	Dionex
DS6 Heated Conductivity Cell	Dionex
IonPac™AS18, RFIC™2x250 mm, Column for ICS Lot. no.: 010-21-131	Dionex
IonPac™AG18, RFIC™2x50 mm, Pre-column for ICS Lot. no.: 006-23-128	Dionex

Continued on next page

TableA.1 continued from previous page

Equipment/model	Manufacturer
Eluent Generator Cartridge, EGC III KOH, RFIC™, Serial no.: 130791248012, Product no.: 074532	Dionex
AS-AP Autosampler for ICS	ThermoFisher Scientific
1.5 mL vial	ThermoFisher Scientific
20 – 200 µL pipette, Proline Plus series	Biohit
100 – 1000 µL pipette, Proline Plus series	Biohit
1 – 5 mL pipette, Proline series	Biohit
Plastic transfer 3.5 mL pipettes	Sarstedt
Milli-Q Integral 3, water purification system	Millipore
Optima 7300 V ICP-OES system	PerkinElmer
S10 Autosampler for ICP-OES system	PerkinElmer
Vectaspin 20, 0.45 µm pore size w/ 50 mL sentrifuge tube	Whatman
High-capacity pump for workplace aerosol collection	Model LR 13758, Doerr, Cedarburg, WI, USA

A.2 Chemicals

Table A.2. Manufacturer and concentration of chemicals used in the thesis work

Chemical	Chemical Formula	Manufacturer	Quality
Ethanol	CH_3CH_2OH	Kemetyl	*pro analysi*
Hydrofluoric acid ≥ 40 %	HF	Sigma Aldrich	*pro analysi*
Hydrochloric acid ≥ 37 %	HCl	Sigma Aldrich	*pro analysi*
Nitric acid ≥ 65 %	HNO_3	Sigma Aldrich	*pro analysi*

Continued on next page

Table A.2 continued from previous page

Chemical	Chemical Formula	Manufacturer	Quality
Acetone	C_3H_6O	VWR International	Technical
Triton®X-100	$C_{14}H_{22}O(C_2H_4O)_n$	Merck	*pro analysi*
pH buffer sol.: pH 10.01	—	HACH	—
pH buffer sol.: pH 7.00	—	HACH	—
pH buffer sol.: pH 4.1	—	HACH	—

Table A.3. Stock solutions used to prepare calibration standards and quality controls. All stock solutions were manufactured by Spectrapure Standards.

Analyte	Chemical formula	Concentration $[\frac{\mu g}{mL}]$
Fluoride	F^-	1000 ± 3
Chloride	Cl^-	1000 ± 3
Sulfate	SO_4^{2-}	1000 ± 3
Phosphate	PO_4^{3-}	1000 ± 3
Beryllium	Be	1000 ± 3
Calcium	Ca	1000 ± 3
Magnesium	Mg	1000 ± 3
Potassium	K	10000 ± 3
Sodium	Na	10000 ± 3
Sulfur	S	1000 ± 3

B

Additional information about experiments and analyses

B.1 IC

All weighed-in amounts of chemicals concerning the ion chromatographic analysis are presented in Tables B.1–B.4.

Table B.1. Weighed-in amounts of FeMn and SiMn FFP and water for extraction of water-soluble fraction

Sample	Powder [mg]	Water[1] [mg]
FeMn-1	98.01	10040.29
FeMn-2	97.33	10010.87
FeMn-3	97.70	9996.29
FeMn-1 Spiked	100.91	10042.95
FeMn-2 Spiked	101.72	10011.29
FeMn-3 Spiked	100.77	9995.26
SiMn-1	101.22	10006.52
SiMn-2	107.34	9988.31
SiMn-3	104.08	9992.48
SiMn-1 Spiked	103.93	9981.28
SiMn-2 Spiked	101.74	9979.00
SiMn-3 Spiked	100.66	9983.10

[1] The temperature was 20 °C

B.2 ICP-OES

Table B.5 show the weighed-in amounts of FFP samples that were digested and analyzed. The DL's and QL's of the elemental analyses performed in this study are presented in Table B.6.

B.3 XRD

Masses workplace aerosol fitlers and personal exposure filters anlayzed in the present thesis are given in Table B.7. Diffractograms from the PHD optimization experiment are presented in Figure B.1.

Table B.2. Weighed-in amounts for addition of internal standard and dilution of the unspiked water-extract samples

Sample	Extract [mg]	Internal standard[1] [mg]	Water[1] [mg]	IS ratio ppm/15ppm
FeMn-1	953.61	593.48	37832.77	1.00471
FeMn-2	946.52	596.08	38795.00	0.98515
FeMn-3	955.18	597.84	38195.80	1.00270
SiMn-1	948.63	148.64	8328.90	1.05126
SiMn-2	947.01	149.26	8836.27	1.00182
SiMn-3	945.21	149.26	8836.27	1.00201

[1] The temperature was 20 °C

Table B.3. Weighed-in amounts for addition of internal standard and spike, and dilution of the spiked samples. The internal standard (IS) ratio used for quantification are also presented.

Sample	Extract [mg]	PO_4^{3-} [mg]	F^- [mg]	Cl^- [mg]	SO_4^{2-} [mg]	H_2O[1] [mg]	IS ratio ppm/15ppm
FeMn-1 Spiked	922.64	593.40	198.90	800.50	1133.50	36762.00	0.97894
FeMn-2 Spiked	970.84	593.67	198.98	794.69	1152.68	36303.52	0.98909
FeMn-3 Spiked	943.48	594.35	199.51	800.65	1154.73	36421.85	0.98775
SiMn-1 Spiked	916.36	146.00	47.56	201.36	296.90	8223.58	0.9899
SiMn-2 Spiked	910.45	145.60	47.50	200.44	296.97	8535.77	0.95757
SiMn-3 Spiked	918.13	145.80	47.88	198.78	297.14	8281.16	0.9829

[1] The temperature was 20 °C

Table B.4. Weighed-in amounts for diluting spiked samples two times. The IS ratios used for quantifications are also presented.

Sample	Extract [mg]	H_2O[1] [mg]	IS ratio ppm/15ppm
FeMn-1 Spiked	2053.54	2011.33	0.49455
FeMn-2 Spiked	2050.81	2016.88	0.49867
FeMn-3 Spiked	2055.92	1998.59	0.50086
SiMn-1 Spiked	2048.99	1996.42	0.50143
SiMn-2 Spiked	2049.24	1997.37	0.48492
SiMn-3 Spiked	2048.50	2001.69	0.49714

[1] The temperature was 20 °C

Table B.5. Weighed-in amounts of FeMn and SiMn furnace fume powder for elemental analysis

Parallel	Weighed-in amounts [mg]	
	FeMn	SiMn
1	10.17	10.14
2	10.18	9.93
3	10.77	10.30
4	10.27	10.43
5	10.24	10.05
6	1.011	10.43

Table B.6. Detection limits (DL) and quantification limits (QL) of the emission lines measured in analysis of tapping fume, water extract, and aerosol filters. DL's are 3SD of blank, while QL are 10SD of blank. All limits given in mg L^{-1}.

Element	Tapping fume		Water extract		Aerosol filters	
	DL	QL	DL	QL	DL	QL
Al	0.11	0.36	0.026	0.087	0.019	0.062
Ca	0.29	0.95	0.007	0.023	0.025	0.083
Fe	0.068	0.23	0.005	0.017	0.018	0.061
K	0.23	0.77	0.044	0.15	0.17	0.57
Mg	0.015	0.051	0.018	0.094	0.015	0.015
Mn	0.040	0.13	0.002	0.008	0.003	0.010
Na	0.057	0.17	0.047	0.16	0.023	0.078
Pb	0.007	0.024	—	—	0.009	0.029
S	—	—	0.15	0.51	0.29	0.97
Si	1.6	5.3	0.24	0.81	0.34	1.1
Zn	0.095	0.32	0.003	0.009	0.022	0.074

Table B.7. Mass [mg] on TF and PEF samples used for XRD analysis. "Top", "Middle", and "Bottom" refer where in the stack each filter was placed.

Sample	Mass on filter [mg]
FeMn TF samples	
Top	0.718
Middle	0.946
Bottom	1.022
SiMn TF samples	
Top	0.364
Middle	0.481
Bottom	0.556
Porsgrunn	
#018	0.762
#021	1.908
#026	2.449
#041	1.105
Sauda	
#002	1.889
#007	1.549
#008	1.741
Kvinesdal	
#026	0.486
#046	0.456

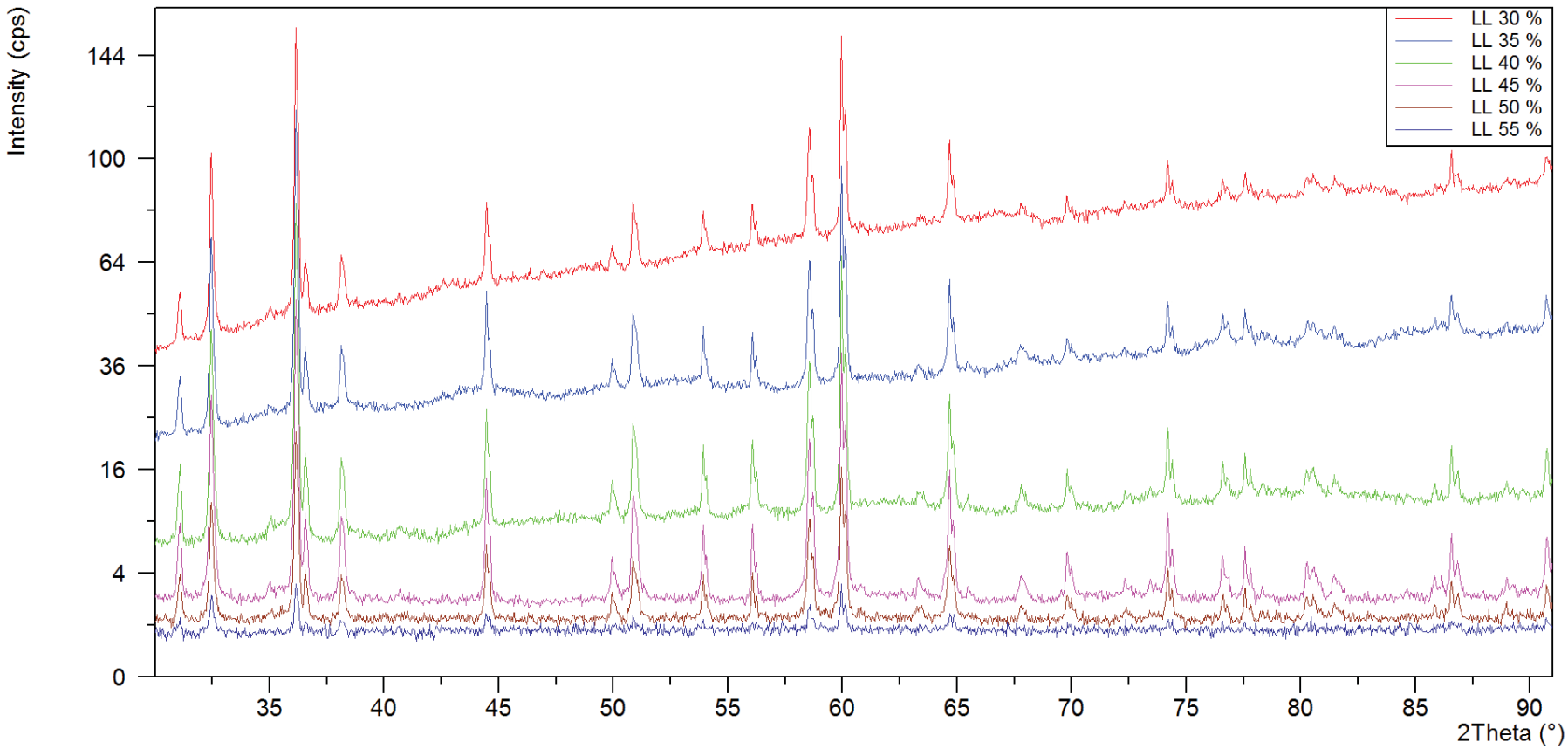

Figure B.1. The diffractograms from the PHD optimization, showing the effect of increasing the lower PDH level from 35 % to 55 %. The intensity (counts per second) is plotted against the 2θ angle (°). The background is dramatically reduced, but the peak intensity only starts to be dramatically reduced at above 45 %. At 55 % most of the peak intensity is lost, and the diffractogram is useless. Signal-to-noise ratio was maximized at 45 %.

C

Examples of calculations

All calculations of concentrations were done in Microsoft Excel speadsheets. The following is of how the sulfate concentrations (in wt%) were carried out, demonstrated for one replicate measurement of FeMn water extract. Approximate values will be used in this example, but the accurate ones were used to calculate the presented concentrations.

The starting point is the concentration reported by the IC software, which we assume to be $44.100\,\mu g\,mL^{-1}$ To calculate the wt% of sulfate in the weighed-in FeMn powder, a series of corrections need to be made to the raw concentration. Normally the blank contribution would be subtracted, but because the blank signals were below the detection limit, this was not possible. Recalling from the methodology, the FeMn water extract was diluted approximately 40 times. The concentration of sulfate in the water extract is therefore

$$[SO_4^{2-}] = 44.100\,\frac{\mu g}{mL} \cdot 40 = 1940.1\,\frac{\mu g}{mL}$$

The concentration of $1940.1\,\frac{\mu g}{mL}$ refers to the concentration of sulfate in the water extract. From the concentration the amount of sulfate, in mg, is found by multiplying the solution volume, which here was approximately 10 mL, and dividing by 1000.

$$m_{SO_4^{2-}} = \frac{1940.1\,\frac{\mu g}{\cancel{mL}}}{1000} \cdot 10\,\cancel{mL} = 19.401\,mg$$

The amount of sulfate in the water extract is therefore 19.401 mg. It is assumed that the extraction was 100 % efficient, meaning that the amount of sulfate in the water extract was assumed to equal the amount of sulfate in the powder. Therefore it is assumed that of the approximately 100 mg powder weighed in, 19.401 mg were sulfate. Taking the ratio and multiplying with 100 % yields the wt% of sulfate in the powder:

$$C_{SO_4^{2-}} = \frac{19.401\,\cancel{mg}}{100\,\cancel{mg}} \cdot 100\,\% = 19.401\,wt\%$$

Based on the standard deviation of replicate samples and measurements, the number of significant digits were not five, as shown here.

Norwegian University
of Life Sciences

Postboks 5003
NO-1432 Ås, Norway
+47 67 23 00 00
www.nmbu.no